Progressive overfilling of readily releasable pool underlies short-term facilitation at recurrent excitatory synapses in layer 2/3 of the rat prefrontal cortex

Jiwoo Shin[1,2,3], Seung Yeon Lee[2], Yujin Kim[1,2,3*], Suk-Ho Lee[1,2,3*]

1. Department of Brain and Cognitive Sciences, College of Natural Sciences, Seoul National University. 2. Department of Physiology, Seoul National University College of Medicine. 03080, Seoul, South Korea. 3. Neuroscience Research Institute, Seoul National University College of Medicine, Seoul 03080, Republic of Korea.

* *corresponding authors*

Yujin Kim Ph.D. (kim.y@snu.ac.kr)
Cell Physiology Lab
Department of Physiology
Seoul National Univ. College of Medicine

Suk-Ho Lee M.D., Ph.D. (leesukho@snu.ac.kr)
Cell Physiology Lab
Department of Physiology
Seoul National Univ. College of Medicine
103 Daehakro, 03080, Seoul, South Korea
Phone) +82-2-740-8222

Abstract

Short-term facilitation of recurrent excitatory synapses within the cortical network has been proposed to support persistent activity during working memory tasks, yet the underlying mechanisms remain poorly understood. We characterized short-term plasticity at the local excitatory synapses in layer 2/3 of the rat medial prefrontal cortex and studied its presynaptic mechanisms. Low-frequency stimulation induced slowly developing facilitation, whereas high-frequency stimulation initially induced strong depression followed by rapid facilitation. This non-monotonic delayed facilitation after a brief depression resulted from a high vesicular fusion probability and slow activation of Ca^{2+}-dependent vesicle replenishment, which led to the overfilling of release sites beyond their basal occupancy. Pharmacological and gene knockdown (KD) experiments revealed that the facilitation was mediated by phospholipase C/diacylglycerol signaling and synaptotagmin 7 (Syt7). Notably, Syt7 KD abolished facilitation and slowed the refilling rate of vesicles with high fusion probability. Furthermore, Syt7 deficiency in layer 2/3 pyramidal neurons impaired the acquisition of trace fear memory and reduced c-Fos activity. In conclusion, Ca^{2+}- and Syt7-dependent overfilling of release sites mediates synaptic facilitation at layer 2/3 recurrent excitatory synapses and contributes to temporal associative learning.

Introduction

Synapses in the mammalian central nervous system undergo activity-dependent modulation of synaptic weight during repetitive stimulation, known as short-term synaptic plasticity (STP). STP is mediated by presynaptic mechanisms that regulate the release probability (p_r), size of the readily releasable pool (RRP), and kinetics of vesicle replenishment of RRP (Zucker and Regehr, 2002; Jackman and Regehr, 2017; Neher and Brose, 2018). Short-term depression has been observed at synapses with a high baseline p_r, primarily because of the rapid depletion of releasable vesicles during high-frequency stimulation (HFS) (Lin et al., 2022). Conversely, vesicle depletion is less pronounced at synapses with a low baseline p_r, and cumulative increases in p_r during HFS are considered to mediate short-term facilitation (Rozov et al., 2001; Pan and Zucker, 2009; Aldahabi et al., 2024). Central synapses exhibit a wide spectrum of STP depending on different combinations of presynaptic factors mediating short-term depression and facilitation.

Previously, facilitation was modeled as an increase in p_r after an action potential (AP) and its slow decay during the inter-spike interval (ISI), resulting in a cumulative increase in p_r during HFS (Markram et al., 1998; Dittman et al., 2000). Recent studies have suggested that the number of docking (or release) sites in an active zone is limited and only partially occupied by releasable vesicles in the resting states (Miki et al., 2016; Pulido and Marty, 2018; Malagon et al., 2020; Lin et al., 2022). Therefore, p_r is determined by the vesicular fusion probability (p_v) and release site occupancy (p_{occ}). However, distinguishing the individual contributions of p_v and p_{occ} to p_r is challenging (Silva et al., 2021; Neher, 2024). It is also

64 unclear whether facilitation is mediated by activity-dependent increases in the p_v, p_{occ}, or
65 both.
66 Two recent models for vesicle priming and release view the 'priming' as a two-step
67 reversible process that leads to a release-ready state. The release-ready vesicles could be
68 vesicles in a tightly docked state (TS) or those occupying specialized docking sites (DS), and
69 are supplied from vesicles in a loosely docked state (LS) or those occupying a distinct
70 replacement sites (RS), which are called LS/TS model (Aldahabi et al., 2024; Neher, 2024)
71 and RS/DS model (Miki et al., 2016; Silva et al., 2021), respectively. Common to both models
72 is the assumption that release-ready vesicles constitute only a fraction of all docked vesicles
73 under resting conditions and that this fraction is up- and down-regulated by synaptic
74 activity.
75 Synaptotagmin-7 (Syt7) was recently found to play a crucial role in facilitation at different
76 types of central synapses (Jackman et al., 2016; Chen et al., 2017; Martinetti et al., 2022). In
77 addition to its role in facilitation, Syt7 accelerates refilling of the RRP after depletion and
78 mediates asynchronous release (Bacaj et al., 2013; Liu et al., 2014; Jackman et al., 2016;
79 Tawfik et al., 2021). Syt7-dependent synaptic facilitation is interpreted as an activity-
80 dependent increase in p_v (Turecek et al., 2016; Jackman and Regehr, 2017; Turecek et al.,
81 2017; Norman et al., 2023). However, it is unclear whether Syt7 contributes to facilitation
82 through a Ca^{2+}-dependent increase in p_{occ} (i.e., overfilling). Overfilling has been proposed as
83 a mechanism supporting facilitation at the Drosophila neuromuscular junction (Kobbersmed
84 et al., 2020), yet whether this process also occurs at the mammalian central synapses
85 mediated by Syt7 has not been studied.

86 Each of layer 2/3 (L2/3) and layer 5 (L5) of neocortex displays intralaminar excitatory
87 synapses between pyramidal cells comprising a recurrent network (Holmgren et al., 2003;
88 Thomson and Lamy, 2007). Short-term facilitation at recurrent excitatory synapses in a
89 cortical network may play a crucial role in maintaining working memory (Mongillo et al.,
90 2008; Mongillo et al., 2012; Hansel and Mato, 2013). Although L2/3 pyramidal cells (PCs)
91 represent task-relevant information during a delay period in working memory tasks
92 (Fujisawa et al., 2008; Ozdemir et al., 2020), most studies on local excitatory recurrent
93 synapses in the neocortex have focused on L5 exhibiting short-term depression (Reyes and
94 Sakmann, 1999; Hempel et al., 2000; Yoon et al., 2020). Further, the synaptic properties of
95 excitatory synapses in L2/3 remain poorly understood.
96 In the present study, we found that HFS of local excitatory synapses in L2/3 of the medial
97 prefrontal cortex (mPFC) induced initial strong depression followed by delayed facilitation,
98 whereas low-frequency stimulation induced slow monotonous facilitation. This unique form
99 of STP could be explained by 1) high p_v of RRP vesicles at rest and throughout a train
100 stimulation; 2) the low resting vesicular occupancy of RRP and its activity-dependent
101 increase. These conditions led to delayed facilitation through progressive overfilling of
102 release sites during HFS with high p_v vesicles beyond the resting occupancy. Syt7 knockdown
103 (KD) in L2/3 PCs completely abolished these synaptic enhancements by inhibiting the Ca^{2+}-
104 dependent increase in release site occupancy. Finally, behavioral tests for trace fear
105 conditioning showed that Syt7 KD impaired the acquisition of trace fear memory and
106 reduced c-Fos expression in the mPFC. Collectively, these results support that Ca^{2+}- and

Syt7-dependent overfilling of release sites mediates synaptic facilitation at L2/3 recurrent excitatory synapses and contributes to temporal associative learning.

Results

Frequency dependence of STP at local excitatory synapses in L2/3 of the prelimbic cortex

We examined STP profiles at recurrent excitatory synapses between L2/3 PCs and at synapses from L2/3-PCs to fast-spiking interneurons (FSINs) in the prelimbic area of the rat mPFC. The PCs and FSINs were identified based on their distinct intrinsic properties and morphologies (***Figure 1—figure supplement 1***). To stimulate presynaptic PCs, L2/3 PCs were transfected with a plasmid encoding oChIEF using *in utero* electroporation (IUE; ***Figure 1A***; Lee et al., 2024). Photo-stimulation of the oChIEF-expressing cell soma at 40 Hz consistently evoked single APs with high fidelity throughout the 600-pulse trains (***Figure 1—figure supplement 2A-B***), which was consistent with little use-dependent inactivation of oChIEF (Lin et al., 2009; Hass and Glickfeld, 2016).

Given that IUE transfected approximately 10-20% of L2/3 PCs (***Figure 1A***), we made a whole-cell patch on a non-transfected L2/3 PC or an FSIN (***Figure 1C***). To stimulate a minimal number of excitatory axon fibers, EPSCs were evoked using minimal optical stimulation (***Figure 1—figure supplement 3A***; 470 nm, 3-4 µm in radius and 3-5 ms in duration). EPSCs evoked by minimal stimulation were examined to determine the uniformity of the kinetic properties (***Figure 1—figure supplement 3B-C***). Moreover, we reassessed the kinetics of EPSCs during trains *post hoc* to ensure uniformity. EPSCs were evoked by 20-pulse trains at 4

128 different frequencies (5, 10, 20, and 40 Hz) to cover the range of firing rates of PCs observed
129 *in vivo* during working memory tasks (Baeg et al., 2003). Excitatory synapses from PCs onto
130 both other PCs and FSINs (PC–PC and PC–FSIN) showed strong (~2-fold enhancement) and
131 lasting (several seconds) short-term facilitation at 20 Hz and lower frequencies (***Figure 1D-***
132 ***E***). The PC-PC synapses exhibited stronger facilitation than did the PC-FSIN synapses.
133 Steady-state EPSCs at the PC-PC synapses were not significantly different from 5 to 20 Hz
134 (***Figure 1F***). Frequency invariance at the PC-PC synapses suggests that Ca^{2+}-dependent
135 synaptic facilitation may counteract vesicle depletion in a frequency-dependent manner
136 (Turecek et al., 2017; Lin et al., 2022). Despite facilitation at all frequencies, the paired pulse
137 ratio (PPR) rapidly decreased as the ISI decreased (***Figure 1G, I***). At 40 Hz stimulation, both
138 PC-PC and PC-FSIN synapses initially underwent strong depression then followed by
139 facilitation in a few stimuli (***Figure 1Dd, Ed***). Such delayed facilitation after paired pulse
140 depression (PPD) has not been previously observed in central synapses except for a slight
141 increase in EPSC at the cerebellar synapses under artificially depolarized conditions (Pulido
142 and Marty, 2018).
143 We confirmed that optically evoked EPSCs were strictly dependent on AP generation (***Figure***
144 ***1—figure supplement 4A***), suggesting that EPSCs are evoked by optical stimulation of
145 presynaptic axon fibers rather than by direct depolarization of presynaptic boutons.
146 Additionally, dual patch-clamp techniques showed that the STP of optically evoked EPSCs
147 did not differ from the electrically evoked STP of EPSCs at the PC-FSIN synapses (***Figure 1—***
148 ***figure supplement 4B***). Finally, we confirmed that AMPA receptor (AMPAR) desensitization
149 was not responsible for PPD at 40 Hz, ruling out the possible effects of postsynaptic factors

150 on STP (***Figure 1—figure supplement 5A***), and that AMPAR saturation was not significant
151 during facilitation (***Figure 1—figure supplement 5B***).
152

153 *Delayed facilitation results from slow activation of Ca^{2+}-dependent vesicle replenishment at a*
154 *constantly high vesicular fusion probability*

155 The strong PPD at 40 Hz suggests a high vesicular fusion probability (p_v) and likely tight
156 coupling of the releasable vesicles to a Ca^{2+} source. To test this hypothesis, we examined the
157 effects of EGTA, a slow calcium chelator, on synaptic transmission at the PC-PC synapses.
158 The baseline EPSC amplitude ($EPSC_1$) was not affected by incubation of the slice in the bath
159 solution containing 50 µM EGTA-AM for longer than 20 min, supporting tight coupling.
160 Moreover, the PPR was decreased to 0.19, and subsequent facilitation slowed but was still
161 distinct (***Figure 2A-B***). These findings indicate that the initial p_v should be higher than 0.81
162 considering vesicle recruitment during ISI. The effects of EGTA-AM were confirmed in the
163 same cell by measuring the baseline EPSC and PPR before and after applying EGTA-AM to
164 the bath. $EPSC_1$ remained unchanged, while PPR was reduced by half (***Figure 2—figure***
165 ***supplement 1***).
166 Notably, the application of EGTA-AM markedly slowed facilitation at 40 Hz (***Figure 2A, C***).
167 The frequency invariance of steady-state EPSCs (***Figure 1F***) and the slower facilitation at 40
168 Hz in the presence of EGTA (***Figure 2A***) imply a Ca^{2+}-dependent increase in the refilling rate
169 of the RRP and/or an increase in the p_v of reluctant vesicles in light of previous studies
170 (Hosoi et al., 2007; Liu et al., 2014; Ritzau-Jost et al., 2014; Turecek et al., 2016; Ritzau-Jost

171 et al., 2018; Kusick et al., 2020). Moreover, facilitation was accelerated at higher stimulation
172 frequencies. The plot of the rate constant for the increase in EPSCs (denoted as $\mathbf{k}_{STF}$, the rate
173 constant for the development of short-term facilitation) as a function of the stimulation
174 frequency (f_{stim}) revealed a linear relationship (***Figure 2C***). $\mathbf{k}_{STF}$ in the presence of EGTA-AM
175 was distinctly below this relationship, supporting the Ca^{2+}-dependent acceleration of
176 facilitation.
177 $\mathbf{k}_{STF}$ was also accelerated when the stimulation frequency was increased from 5 Hz to 40 Hz
178 (***Figure 2D***; 1.27 ± 0.18/s to 24.27 ± 3.44/s). Notably, the second 40-Hz train stimulation led
179 to strong PPD, followed by accelerated facilitation (***Figure 2D-E***). The strong PPD suggests
180 that the vesicular fusion probability kept high during the 5-Hz stimulation, arguing against
181 the possibility for an increase in p_v. Both two-step sequential priming models, LS/TS and
182 RS/DS models, are suitable to interpret our data and we will refer to the different
183 populations of vesicles as TS and LS vesicles, respectively (Taschenberger et al., 2016; Neher
184 and Brose, 2018; Lin et al., 2022; Neher, 2024). Within this framework, vesicles are released
185 from TS with high p_v both in the resting state and during facilitation, and the delayed
186 facilitation is seen as a result of Ca^{2+}-dependent progressive increase in the occupancy of TS
187 vesicles on docking sites.
188

189 *Presynaptic calcium measurements at axonal boutons of L2/3 pyramidal cells*

190 To test contribution of Ca^{2+} channel regulation to STP (Dobrunz et al., 1997; Jackman and
191 Regehr, 2017), we estimated total amount of Ca^{2+} increments during 40 Hz AP trains at

192 axonal boutons of L2/3 PCs in the mPFC. To this end, we measured AP-evoked Ca^{2+}
193 transients (AP-CaTs) using two-dye ratiometry techniques, and estimated calcium binding
194 ratio from AP-CaTs (***Figure 2—figure supplement 2A-C***). Measuring the amplitudes and
195 decay time constants of AP-CaTs at different concentrations of Fluo-5F (150, 250 or 500
196 μM), and plotting them as a function of calcium binding ratio of Fluo-5F (κ_B), we estimated
197 the amplitude of AP-CaTs (A_{Ca} = 1.16 μM), Ca^{2+} decay time constant (τ_c = 43 ms) in the
198 absence exogenous Ca^{2+} buffer, and endogenous static Ca^{2+} binding ratio (κ_S = 96.4 or 77.3
199 estimated from ***Figure 2—figure supplement 2D-E***, respectively; *See Materials and*
200 *Methods*). The resting [Ca^{2+}] ([Ca^{2+}]$_{rest}$) was measured as 50 nM (***Figure 2—figure***
201 ***supplement 2F***). Estimating the total Ca^{2+} increments for the first four AP-CaTs in a 40 Hz
202 train according to Equation 2 (*Materials and Methods*), we found no evidence for
203 inactivation or facilitation of calcium influx during a 40 Hz train (***Figure 2—figure***
204 ***supplement 2G-I***), arguing against the possibility that Ca^{2+} channel inactivation and
205 facilitation contribute to strong PPD and delayed facilitation during a 40 Hz train.
206

207 *Release sites have low baseline occupancy and these are increased during facilitation and*
208 *post-tetanic augmentation*

209 Given that p_v was greater than 0.8, the two-fold increase in EPSC during 20 pulse train
210 stimulations could not be explained by an increase in p_v. Recent studies have shown that
211 vesicle release sites (N) are limited in number and are partially occupied at rest (Miki et al.,
212 2016; Pulido and Marty, 2018; Malagon et al., 2020; Lin et al., 2022). Under such a high p_v,

213 two-fold synaptic facilitation should be attributed to an increase in p_{occ}. The vesicle
214 replenishment rate is accelerated during HFS in a Ca^{2+}-dependent manner (***Figure 2A-C***;
215 Hosoi et al., 2007). This may lead to the overfilling of release sites beyond their basal
216 vesicular occupancy, which in turn may increase EPSC under high p_v. To test this hypothesis,
217 we determined the quantal parameters at the L2/3 local excitatory synapses. We first
218 measured the quantal size from asynchronous release events after replacing extracellular
219 Ca^{2+} with Sr^{2+}, as previously described (Yoon et al., 2020) (***Figure 3—figure supplement 1A-***
220 ***B***). The mean and coefficient of variance of the quantal sizes were 24 pA and 0.25 at PC-PC
221 synapses, respectively, and were 30 pA and 0.31 at PC-FSIN synapses (***Figure 3—figure***
222 ***supplement 1C***).
223 Next, we performed a variance-mean (V-M) analysis of phasic EPSCs at excitatory synapses
224 during train stimulation at 5 Hz and 40 Hz (Scheuss et al., 2002). Applying multiple-
225 probability fluctuation analysis (MPFA) using intra-site quantal variability of 0.2 (Valera et
226 al., 2012), the V-M plot was best fitted by the number of release sites (N) of 5.3 and the
227 quantal size (q) of 25 pA at the PC-PC synapses (***Figure 3A***). The p_r for $EPSC_1$ was calculated
228 as 0.32. We performed the same analysis for the PC-FSIN synapses and found N = 5.3, q = 35
229 pA, and p_r for $EPSC_1$ = 0.31 (***Figure 3B***). Our estimate for N was smaller but comparable to
230 the estimate (6.9) at excitatory synapses in L2/3 of the mouse barrel cortex (Holler et al.,
231 2021).
232 The p_r estimate was clearly smaller than the possible minimum value for p_v (0.81) estimated
233 from the PPR data (***Figure 2B***). Given that p_r is a product of p_{occ} and p_v (Neher, 2024), a p_r
234 smaller than p_v indicates the partial occupancy of release sites in the resting state. If

235 synaptic facilitation were mediated by the recruitment of new release sites, it would be
236 accompanied by an increase in the variance of augmented EPSCs (Valera et al., 2012;
237 Kobbersmed et al., 2020). However, the augmented EPSCs during facilitation followed the
238 same parabola in the V-M plot (***Figure 3A-B***). Therefore, facilitation appears to be mediated
239 by the progressive overfilling of a finite number of release sites beyond the basal occupancy.
240 In the next section, we show that p_v is close to unity based on high double failure rate upon
241 paired pulse stimulation (***Figure 3—figure supplement 2***) and little effect of extracellular
242 $[Ca^{2+}]$ ($[Ca^{2+}]_o$) elevation on baseline EPSC amplitudes (***Figure 3—figure supplement 3***).
243 Assuming this, the baseline p_r at the first pulse estimated from the fitted parabolic curve can
244 be largely regarded as a baseline p_{occ} (c.a. 30%), and the two-fold increase in EPSCs during
245 facilitation can be attributed to an increase of up to 60% in p_{occ}.
246 We investigated the time course of recovery from facilitation and post-tetanic
247 augmentation (PTA) by applying dual-train stimulations (30 pulses at 40 Hz) separated by
248 different inter-burst intervals (IBIs; ***Figure 3C-D***). The initial EPSCs in the second train were
249 enhanced by more than twofold, and followed by a strong PPD, suggesting that fusion
250 probability stays high in the IBIs and thus synaptic transmission is carried by TS vesicles. The
251 decay time course of PTA was characterized by two phases (initially fast and later slow;
252 ***Figure 3E***), which may reflect a two-phase Ca^{2+} decay or two distinct recovery processes that
253 occur sequentially. The variance of potentiated EPSCs measured at IBIs of 0.1, 0.2, and 0.5 s
254 was not different from that of EPSCs at the peak of facilitation (filled circles, ***Figure 3A-B***).
255 Given that the same RRP mediates both facilitation and augmentation and that post-tetanic

256 EPSCs is carried by TS vesicles similar to the baseline EPSCs, this plot suggests that PTA,
257 similar to short-term facilitation, is mediated by an increase in the TS vesicle occupancy.
258

259 *High double failure rate and little effect of $[Ca^{2+}]_o$ elevation on baseline EPSC amplitudes*
260 *suggest that vesicular fusion probability is close to one*

261 The vesicle dynamics of STP has been explained using a simple refilling model (Hosoi et al.,
262 2007; Neher and Sakaba, 2008). This model assumes that the vesicles are reversibly docked
263 to a limited number of release sites (N) with forward and reverse rate constants (denoted as
264 k_1 and b_1, respectively). Under the framework of the simple refilling model (see *Materials*
265 *and Methods*), the rate constant for the refilling of the RRP after depletion by the first pulse
266 is the sum of the baseline k_1 and b_1. This is estimated as 23/s from the plot of PPR as a
267 function of ISIs (***Figure 3—figure supplement 2A***). From the baseline occupancy of 0.3 and
268 $p_{occ} = k_1 / (k_1 + b_1)$, we estimated k_1 to be 6.9/s.
269 When paired APs were applied with an ISI of 20 ms, the failure rate at 1st pulse, $P(F_1)$, was
270 10.6%, and the probability of two consecutive failures, $P(F_1, F_2)$, was 6.2% (***Figure 3—figure***
271 ***supplement 2A***). From the equation $P(F_1) = (1 – p_r)^N$, p_r was calculated as 0.312 when N = 6,
272 comparable to p_r (= 0.32) estimated from the V-M analysis (***Figure 3A***). We calculated $P(F_1,$
273 $F_2)$ under the framework of a simple refilling model, with p_v and k_1 set as free parameters
274 and other parameters set according to the following relationships: $P(F_1) = (1 – p_r)^N$, $p_r = p_v$
275 $\cdot p_{occ}$, and $p_{occ} = k_1 / (k_1 + b_1)$. The calculated values for $P(F_1, F_2)$ and their difference from the
276 observed value (6.2%) are shown in the plane of k_1 *vs*. p_v in ***Figure 3—figure supplement 2B-***

277 ***C***. Given that k_1 was greater than 5/s, the difference between the calculated and observed
278 values of $P(F_1,F_2)$ was minimal when $p_v = 1$ (***Figure 3—figure supplement 2C***).
279 To find optimal values for k_1 and p_v that best explain observed probabilities shown in ***Figure***
280 ***3—figure supplement 2Ac***, a cost function was implemented as the sum of squared errors
281 between observed and predicted probability values for the four combinations of success
282 and failure of 1st and 2nd EPSCs as described in *Materials and Methods*. The minimum of
283 the cost function (5.63×10^{-5}) was found at $k_1 = 5.21$/s and $p_v = 0.999$, which predicted P_{11} =
284 41.5%, P_{10} = 47.9%, P_{01} = 4.93%, and P_{00} = 5.67% (subscript 1 and 0 denote success and
285 failure, respectively).
286 To further validate that baseline p_v is near to unity, we examined EPSC changes following
287 elevation of $[Ca^{2+}]_o$ from 1.3 to 2.5 mM. According to the fourth-power relationship
288 between synaptic responses and $[Ca^{2+}]_o$ (Equation 3 in (Dodge Jr and Rahamimoff, 1967)), a
289 3.24-fold increase in the EPSC amplitude was expected. However, the EPSC amplitude
290 increased only 1.23-fold in average, a change that was not statistically significant (***Figure 3—***
291 ***figure supplement 3A-B***). This small response suggests that p_v is already saturated at rest,
292 limiting the dynamic range for further enhancement through increased calcium influx.
293 Recent morphological and functional studies revealed that elevation of $[Ca^{2+}]_o$ induces an
294 increase in the number of TS or docked vesicles to a similar extent as our observation
295 (Kusick et al., 2020; Lin et al., 2025), raising a possibility that an increase in p_{occ} is
296 responsible for the 1.23-fold increase in EPSC at high $[Ca^{2+}]_o$. A slight but significant
297 reduction in PPR was observed under high $[Ca^{2+}]_o$ too. An increase in p_{occ} is thought to be
298 associated with that in the baseline vesicle refilling rate. While PPR is always reduced by an

299 increase in p_v, the effects of refilling rate to PPR is complicated. For example, PPR can be
300 reduced by both a decrease (***Figure 2—figure supplement 1***) and an increase (Lin et al.,
301 2025) in the refilling rate induced by EGTA-AM and PDBu, respectively. Thus, the slight
302 reduction in PPR is not contradictory to the possible contribution of p_{occ} to the high $[Ca^{2+}]_o$
303 effects. Notably, when slices were pre-incubated with 50 μM EGTA-AM, elevating
304 extracellular $[Ca^{2+}]$ from 1.3 to 2.5 mM produced no significant change in either baseline
305 EPSC amplitude or PPR (***Figure 3—figure supplement 3C-D***), supporting that the modest
306 Ca^{2+}-dependence of baseline EPSCs and PPR in the absence of EGTA is primarily mediated by
307 a change in p_{occ} rather than p_v.
308

309 *Pharmacological manipulations reveal specific molecular identities underlying vesicle loading*
310 *processes*

311 Our results suggest that the baseline occupancy of TS vesicles is low and that the activity-
312 dependent progressive overfilling of docking sites with TS vesicles is responsible for short-
313 term facilitation and augmentation. To elucidate the specific molecular link between
314 synaptic enhancement and Ca^{2+}-dependent overfilling, we examined the effects of several
315 drugs known to affect vesicle dynamics. We first examined the roles of phospholipase C
316 (PLC) and diacylglycerol (DAG) by applying 5 μM U73122, a PLC inhibitor, or 20 μM 1-oleoyl-
317 2-acetyl-sn-glycerol (OAG), a DAG analog. The STP at 40 Hz and PTA at 0.5-s interval were
318 examined before and after applying each drug to the bath. For both drugs, the facilitation
319 and augmentation were reduced (***Figure 4A-B***). U73122 did not affect the basal EPSC

320 amplitude ($EPSC_1$) but resulted in a stronger PPD, slower facilitation, and lower
321 augmentation (***Figure 4A***). These effects of U73122 suggest the involvement of Ca^{2+}-induced
322 PLC activation in progressive overfilling. In contrast, OAG increased $EPSC_1$ while maintaining
323 a pronounced PPD (***Figure 4B***), indicating an increase in the TS vesicle pool size. Meanwhile,
324 OAG slowed $\mathbf{k}_{STF}$ and reduced augmentation, indicating occlusion of activity-dependent
325 synaptic facilitation. Phorbol esters and DAG are thought to accelerate priming through
326 Munc13 activation (Rhee et al., 2002; Taschenberger et al., 2016; Aldahabi et al., 2022); they
327 also shorten the bridges that interlink docked vesicles with the active zone (AZ) membrane
328 (Papantoniou et al., 2023). Collectively, these suggest that PLC- and DAG-mediated signaling
329 play a role in the overfilling of docking sites underlying short-term facilitation and
330 augmentation.
331 Although the acceleration of Ca^{2+}-dependent vesicle refilling supports rapid facilitation at 40
332 Hz, the later part of the delayed facilitation underwent a slight depression, which was more
333 pronounced during the second burst (***Figure 3D and Figure 4***). Sustained synaptic
334 transmission is limited by the spatial availability of docking sites because it is undermined by
335 accumulation of exocytic remainings in the presynaptic AZ during HFS (Neher, 2010; Haucke
336 et al., 2011). To verify this, we examined the effects of dynasore (100 μM), a specific
337 inhibitor of endocytosis (Macia et al., 2006). The treatment with dynasore did not influence
338 $EPSC_1$ or the early phase of facilitation, but it exacerbated depression during the later phase
339 and attenuated PTA (***Figure 4C***). This suggests that late synaptic transmission during the 40-
340 Hz train is limited by site clearance.

341 Given the involvement of actin polymerization in the multiple steps of vesicle docking and
342 recycling, we examined the effects of 20 μM latrunculin B (LatB), an inhibitor of actin
343 polymerization. The effects of LatB were complicated: (1) $EPSC_1$ was decreased, whereas
344 PPR was increased (***Figure 4Da***) and (2) facilitation and augmentation were reduced (***Figure***
345 ***4Db***). The latter effect may result from defects in vesicle replenishment rates, either
346 through the impaired physical movement of vesicles or disrupted site clearance (Sakaba and
347 Neher, 2003; Lee et al., 2012; Hallermann and Silver, 2013; Miki et al., 2016), as Ca^{2+}-
348 dependent vesicle refilling mediates facilitation and augmentation (***Figure 2 and Figure 3***).
349 Meanwhile, the former effect might be attributed to a shift in equilibrium in the priming
350 states towards a loosely docked state (LS) at rest. It is unknown whether actin affects
351 vesicular fusogenicity in neurons, although it facilitates multiple steps of vesicle fusion by
352 enhancing membrane tension in neuroendocrine cells (Wu and Chan, 2022).
353
354 *Short-term facilitation at both types of local excitatory synapses in L2/3 is abolished by Syt7*
355 *knockdown*

356 We examined whether Syt7 mediates facilitation at the PC-PC and PC-FSIN synapses in L2/3
357 of the mPFC. To this end, oChIEF and shRNA against Syt7 (shSyt7) were co-expressed in L2/3
358 PCs using IUE. Syt7 KD resulted in a complete loss of facilitation at all tested stimulation
359 frequencies (***Figure 5A-B***). Short-term depression and paired-pulse depression were more
360 pronounced as the stimulation frequency increased, and the frequency invariance of steady-
361 state EPSC was abolished, implying little contribution of Ca^{2+}-dependent vesicle recruitment
362 (***Figure 5C-F***). The lack of facilitation could not be attributed to the failure of APs in

363 presynaptic axons, as optical stimulation elicited reliable APs in Syt7 KD PCs during the 40-
364 Hz train (***Figure 1—figure supplement 2C***). Syt7 KD had little effect on the basal properties,
365 including the peak amplitude, rise/decay time, and time-to-peak, of single AP-induced EPSCs
366 (***Figure 1—figure supplement 3D-E***). Moreover, Syt7 KD did not significantly affect the
367 intrinsic properties of neurons (***Figure 5—figure supplement 1***).
368 To examine whether Syt7 KD had any nonautonomous effects on postsynaptic cells, we
369 measured the quantal size (q) from asynchronous events in the presence of Sr^{2+} and found
370 that the mean quantal size remained unaltered at Syt7 KD synapses (***Figure 3—figure***
371 ***supplement 1C***). This indicated that Syt7 did not influence postsynaptic parameters,
372 including the density and kinetic properties of AMPARs. To test the specificity of shSyt7, we
373 examined whether co-expression of the shRNA-resistant form of Syt7 restored synaptic
374 facilitation in both excitatory synapse types. Presynaptic overexpression of shRNA-resistant
375 Syt7 under the CAG promoter rescued the effect of shRNA at both PC-PC and PC-FSIN
376 synapses (***Figure 5—figure supplement 2***). These results underscore the crucial role of
377 presynaptic Syt7 in mediating short-term facilitation at local excitatory synapses in L2/3 of
378 the mPFC.
379
380 *Syt7 KD synapses exhibit complementary changes in the number of release sites and their*
381 *vesicle occupancy*

382 To estimate the quantal parameters in Syt7 KD synapses, we performed V-M analysis of
383 EPSCs evoked by train stimulation (***Figure 6A-B***). Fitting a parabola to the V-M plot revealed
384 higher baseline p_{occ} in Syt7 KD synapses than in wild-type (WT) synapses for both synapse

385 types (KD, 0.68 and 0.42; WT, 0.32 and 0.31 for PC-PC and PC-FSIN synapses, respectively).
386 The p_{occ} monotonously decreased during a train stimulation, as expected from short-term
387 depression. Moreover, the number of release sites (N) was markedly lower in Syt7 KD
388 synapses (N = 3.5) than in WT synapses (N = 5.3; ***Figure 3A***). Next, we examined the PTA
389 induced by the same protocol as in ***Figure 3*** (two 40-Hz train stimulations separated by
390 variable IBIs) at Syt7 KD synapses (***Figure 6C***). The 40 Hz train-induced synaptic depression
391 quickly recovered during IBIs, but no PTA was observed at Syt7 KD synapses, indicating its
392 crucial role in augmentation (***Figure 6D-E***).
393
394 *TS vesicle recovery following depletion is accelerated by Syt7*

395 Syt7 is recognized not only for its crucial role in facilitation, but also for mediating Ca^{2+}-
396 dependent replenishment of releasable vesicles (Liu et al., 2014; Tawfik et al., 2021). Given
397 that facilitation at L2/3 excitatory synapses is driven by progressive overfilling (***Figure 2 and***
398 ***Figure 3***), the loss of facilitation at Syt7 KD synapses in the present study implies that Syt7
399 plays a key role in the Ca^{2+}-dependent acceleration of refilling and overfilling of the docking
400 sites with TS vesicles. To test this hypothesis, we examined the recovery kinetics of EPSCs
401 after TS vesicles were depleted by 3 pulses at 40 Hz in wild-type (WT) and Syt7 KD synapses
402 (***Figure 7***). Strong PPD was observed not only in the first burst, but also in the second burst.
403 This suggested that EPSCs in the second burst were mediated by TS vesicles, similar to those
404 in the first burst (***Figure 7A, D***). Therefore, $EPSC_1$ in the second burst can be interpreted as a
405 release from TS vesicles recovering during a given IBI. The recovery time course of $EPSC_1$ in
406 the second burst indicated full recovery of TS vesicles within 100 ms in both excitatory

407 synapse types in WT rats (***Figure 7C, F***). However, this recovery was remarkably slower in
408 Syt7 KD synapses, requiring 5 s for full recovery, indicating that TS vesicle recovery was
409 greatly accelerated by Syt7. Overall, synaptic facilitation and augmentation at local
410 excitatory synapses in L2/3 can be ascribed to progressive activity-dependent increases in
411 the occupancy of TS vesicles (***Figure 2 and Figure 3***), in which Syt7 plays a key role.
412

413 *Behavioral consequences of Syt7 KD in L2/3 PCs of the mPFC*

414 We previously proposed that the disparity in STP between the PC-PC and PC-IN synapses
415 results in activity-dependent changes in the ratio of synaptic weights at the PC-PC and PC-IN
416 synapses (J_{ee}/J_{ie}). This may in turn have a profound influence on persistent activity in a
417 recurrent network by biasing the E-I balance (Yoon et al., 2020). Syt7 KD not only eliminated
418 facilitation, but also the activity-dependent increase in the J_{ee}/J_{ie} ratio in the L2/3 network
419 (***Figure 8—figure supplement 1***). This suggests the possibility that Syt7 contributes to the
420 persistent activity during working memory tasks in the L2/3 recurrent network. Trace fear
421 conditioning (tFC) requires associative learning between an auditory cue (conditioned
422 stimulus, CS) and temporally separate aversive events (unconditioned stimulus, US). The
423 formation of trace fear memory requires the prelimbic area of the mPFC and hippocampus.
424 mPFC activity during the trace interval is thought to temporarily hold CS information,
425 enabling the network to associate temporally discontinuous events (i.e., temporal
426 associative learning) (Gilmartin et al., 2013). Synaptic facilitation and augmentation are

427 implicated in temporary memory retention in recurrent networks (Mongillo et al., 2008;
428 Mongillo et al., 2012).
429 Given that Syt7 is crucial for synaptic facilitation (***Figure 5***) and augmentation (***Figure 6***) in
430 prelimbic L2/3 recurrent excitatory synapses, we tested whether trace fear memory
431 formation was impaired in rats with depleted Syt7 transcripts, specifically in the L2/3 PCs of
432 the mPFC. Syt7-targeted shRNA (shSyt7) or scrambled shRNA (Scr) constructs were
433 transfected bilaterally into the L2/3 PCs of the mPFC using IUE (***Figure 8A***). Both the Scr-
434 transfected control and shSyt7-transfected rats underwent tFC training (***Figure 8B***).
435 Consistent with Gilmartin et al. (2013), in which prefrontal persistent firing was
436 optogenetically inhibited, WT and KD animals exhibited similar freezing behavior during this
437 acquisition phase. The following day, the rats were subjected to a tone test in which trace
438 fear memory formation was assessed from the freezing response to a tone alone in a
439 distinct context. Compared to the control group, the shSyt7-transfected group exhibited
440 significantly lower levels of freezing behavior in response to auditory cues during the first
441 four trials, suggesting an impairment in trace memory formation (***Figure 8C***).
442 The tone test was repeated the following day to test for extinction memory formation. Syt7
443 KD animals exhibited much less freezing to the CS (+1d) than did WT animals. Considering
444 the Rescorla-Wagner model (Yau and McNally, 2023), our results suggest that the strength
445 of CS-US associative memory was weaker in KD animals than in WT animals; thus, the
446 acquisition of trace fear memory was impaired by Syt7 KD in the L2/3 PCs of the mPFC.
447 Next, we assessed the locomotor activity and anxiety levels of rats using the open field test
448 (OFT) and elevated plus maze test (EPM). Scr controls and Syt7 KD rats showed similar

449 exploratory patterns, displaying comparable total distance moved and time spent in the
450 periphery of the OFT or the open/closed arms of the EPM (***Figure 8—figure supplement 2***).
451 Previous studies have suggested that the acquisition of trace fear memory requires elevated
452 trace activity in prelimbic PCs (Gilmartin et al., 2013). Given that c-Fos, an immediate early
453 gene, is upregulated following patterned activities in neurons, its expression is considered a
454 reliable indicator of recent neuronal activation (Fields et al., 1997; Guzowski et al., 2005). To
455 investigate the effect of Syt7 on neuronal activity *in vivo* during tFC, animals were sacrificed
456 at the time of peak c-Fos protein expression, approximately 90 min after completion of the
457 behavioral task (Arime and Akiyama, 2017).
458 To elucidate the activation patterns of specific neuronal populations, we performed
459 immunohistochemical co-labeling of c-Fos and GAD67 (a GABAergic interneuron marker)
460 upon tFC acquisition. The density of c-Fos(+) cells and the percentage of c-Fos(+) cells
461 among GAD67(+) cells in all prelimbic layers were significantly lower in Syt7 KD rats than in
462 control rats (***Figure 8F-G***). Additionally, analysis of the proportion of active cells among
463 transfected L2/3 PCs (c-Fos+/GFP+) revealed that Syt7 KD L2/3 PCs were significantly more
464 active than Scr-transfected PCs (***Figure 8H***). This unexpected hyperactivity of Syt7 KD PCs
465 may be attributed to the high reciprocal connectivity between PCs and FSINs in the
466 neocortex (Holmgren et al., 2003; Otsuka and Kawaguchi, 2009), as PCs with short-term
467 depression would transmit less input to FSINs, which in turn would exert less feedback
468 inhibition on reciprocally connected PCs. Collectively, these findings show that the slow
469 activation of vesicle refilling supports various forms of facilitation at excitatory synapses in
470 PFC L2/3, which is essential for neuronal activity during temporal associative learning.

471

472 ## Discussion

473 The present study characterized STP at local excitatory synapses in the L2/3 network of the
474 rat mPFC at physiological extracellular [Ca^{2+}]. These synapses displayed initial strong
475 depression and then delayed facilitation at 40 Hz, while monotonous slowly developing
476 facilitation was observed at lower frequencies. Our study suggests that such delayed
477 facilitation after a brief depression results from a high p_v (***Figure 2 and Figure 3 and Figure***
478 ***3—figure supplement 2***), along with Ca^{2+}-dependent delayed acceleration of vesicle refilling
479 and overfilling (***Figure 2 and Figure 3***). The two-fold increase in EPSC during 20 pulse train
480 stimulations under the condition of such a high p_v suggests a Ca^{2+}-dependent increase in the
481 vesicle replenishment rate during a train; this then leads to overfilling of release sites
482 beyond their incomplete basal occupancy (***Figure 3A-B***). The high p_v and strong PPD did not
483 result from artificial bouton stimulation, AMPAR desensitization, or any potential distortion
484 caused by optogenetic methods (***Figure 1—figure supplements 4 and 5***). Additionally,
485 similar to short-term facilitation, PTA could be explained by an increase in the TS vesicle
486 occupancy (***Figure 3C-E***), consistent with previous studies showing post-tetanic increases in
487 the p_{occ} and/or vesicle pool size at various types of synapses (Lee et al., 2010; Vandael et al.,
488 2020; Tran et al., 2023; Silva et al., 2024). These findings suggest that release sites are
489 partially occupied at rest and that a progressive overfilling of release sites with TS vesicles
490 underlies facilitation and augmentation at intracortical L2/3 excitatory synapses.

491

492 *Definition of vesicular release probability in the present and previous studies*

493 Previous studies for post-tetanic augmentation (Stevens and Wesseling, 1999; Garcia-Perez
494 and Wesseling, 2008) observed invariance of the RRP size after tetanic stimulation. In these
495 studies, the RRP size was estimated by hypertonic sucrose solution or as the sum of EPSCs
496 evoked 20 Hz/60 pulses train (denoted as 'RRP_{hyper}'). Because reluctant vesicles can be
497 quickly converted to TS vesicles (16/s) and are released during a train (Lee et al., 2012), it is
498 likely that the RRP size measured by these methods encompasses both LS and TS vesicles. In
499 contrast, we assert high p_v based on the observation of strong PPD, failure rates upon paired
500 stimulations at ISI of 20 ms (***Figure 2 and Figure 3—figure supplement 2***). Given that single
501 AP-induced vesicular release occurs from TS vesicles but not from LS vesicles, p_v in the
502 present study indicates the fusion probability of TS vesicles. From the same reasons, p_{occ}
503 denotes the occupancy of release sites by TS vesicles. Note that our study does not provide
504 direct clue whether release sites are occupied by LS vesicles that are not tapped by a single
505 AP, although an increase in the LS vesicle number may accelerate the recovery of TS
506 vesicles. As suggested in Neher (2024), even if the number of LS plus TS vesicles are kept
507 constant, an increase in p_{occ} (occupancy by TS vesicles) would be interpreted as an increase
508 in 'vesicular release probability' if it was measured based on RRP_{hyper}.

509 By the way, it should be noted that increases in both p_v and p_{occ} may contribute to PTA.
510 Post-tetanic potentiation (PTP) and phorbol esters had similar effects on baseline EPSCs
511 (Taschenberger et al., 2016), and PDBu increased both the TS vesicle pool size (1.9-fold) and
512 fusion probability of TS vesicles (1.3-fold) at the calyx synapses (Lin et al., 2025). Therefore,
513 it is possible that PTP may increase both p_{occ} and p_v of TS vesicles, although it has not been

514 yet directly tested. Moreover, acceleration of the latency in the hypertonicity-induced
515 vesicle release raises a possibility for an increase in fusion probability of TS vesicles (Stevens
516 and Wesseling, 1999; Garcia-Perez and Wesseling, 2008), although it is still controversial
517 that the acceleration of the release latency represents a reduction in the activation energy
518 barrier for vesicle fusion (Schotten et al., 2015).
519

520 *Progressive overfilling of docking sites*

521 Conventional models for facilitation assume an increase in p_v after an AP of RRP vesicles,
522 which had been in a low p_v or reluctant state at rest (Dittman et al., 2000; Turecek et al.,
523 2016). This facilitation model is unlikely to explain our results, because TS vesicles are
524 predominantly released not only at rest but also in the facilitated state during or after train
525 stimulation, as evidenced by the strong PPD (ISI, 25 ms) during a 5-Hz train (***Figure 2D-E***)
526 and at different intervals after a 40-Hz/30 pulse trains (***Figure 3D***). Moreover, the PPD (ISI,
527 25 ms) remained pronounced during the early phase of facilitation (***Figure 7***), arguing
528 against the possibility of slowly increasing the p_v of reluctant vesicles. These results
529 suggested that facilitation was mediated by an activity-dependent progressive increase in
530 occupancy of TS vesicles (TS occupancy). Facilitation through an increase in TS occupancy
531 has been termed frequency facilitation, differentiating it from paired pulse facilitation that
532 relies on a residual calcium-dependent transient increase in the p_v of releasable vesicles
533 (Neher, 2024).

534 Assuming an increase in TS occupancy, to attain a two-fold increase in EPSC (***Figure 1***), the
535 baseline occupancy of the docking sites by TS vesicles should be low, as estimated from the
536 V-M plot (c.a. 30% in ***Figure 3***). However, it is unclear whether the remaining docking sites
537 that are not occupied by TS vesicles are truly vacant or are occupied by reluctant LS vesicles
538 that are not released by the AP or AP trains. TS vesicles can be supplied by the
539 transformation of LS to TS vesicles, both of which reside at the same docking site (LS/TS
540 model; reviewed in Neher, 2024). Alternatively, TS vesicles can be supplied from a distinct
541 replacement pool (RS/DS model; reviewed in Silva et al., 2021). Further studies, including
542 ultrastructural analyses of active zones, are required to address this issue.
543 Given the crucial role of Syt7 in facilitation (***Figure 5***), the facilitation mechanisms are closely
544 related to how Syt7 mediates synaptic facilitation. Based on the slow kinetics of Syt7,
545 previous computational modeling studies have proposed that Syt7 may mediate short-term
546 facilitation through an activity-dependent increase in p_v (Turecek et al., 2016; Jackman and
547 Regehr, 2017; Turecek et al., 2017; Norman et al., 2023). The present study, however, found
548 that both facilitation and augmentation were mediated by overfilling of the release sites
549 (***Figure 2 and Figure 3***). Moreover, Syt7-KD synapses displayed slower recovery of TS
550 vesicles (***Figure 7***). These results suggest that Syt7 is essential for activity-dependent
551 overfilling of docking sites with TS vesicles. Whereas the baseline EPSC was not altered
552 (***Figure 1—figure supplement 3***), and complementary changes in the number of docking
553 sites and their baseline occupancy were observed in Syt7 KD synapses (***Figure 6***). These
554 results raise a possibility that Syt7 may play a role in providing additional vacant docking
555 sites that can be overfilled during facilitation. It remains to be elucidated whether the

556 decrease in the number of docking sites at Syt7 KD synapses is related to the subcellular
557 localization of Syt7 to the plasma membrane of the active zone (Sugita et al., 2001; Vevea et
558 al., 2021).
559

560 *STP model in light of known Ca^{2+} binding kinetics of Syt7*

561 Syt7 acts as an upstream Ca^{2+} sensor that facilitates activity-dependent replenishment (Liu
562 et al., 2014; Bacaj et al., 2015; Chen et al., 2017; Tawfik et al., 2021). The present study
563 shows that EPSCs are mediated by TS vesicles both at rest and during activity-dependent
564 facilitation. Releasable vesicles are homogeneous, and Syt7-dependent overfilling is
565 responsible for the activity-dependent enhancement of EPSCs. Thus, we tested whether
566 slowly developing facilitation could be replicated within the framework of a simple refilling
567 model based on the known Ca^{2+} binding kinetics of Syt7 (Brandt et al., 2012). To this end, we
568 made following assumptions: (1) a Ca^{2+}-dependent increase in the forward refilling rate (k_1)
569 requires a full Ca^{2+}-bound form of Syt7, to which multiple Ca^{2+} ions can bind (two or three
570 Ca^{2+} ions on each C2A and/or C2B domain) (Brandt et al., 2012; Chon et al., 2015; Voleti et
571 al., 2017); (2) sequential Ca^{2+} binding steps are synergistic through a cooperativity factor, *b*;
572 (3) Syt7 senses AP-induced local [Ca^{2+}] similar to that estimated at the calyx of Held (a
573 Gaussian function with a full width at half maximum value of 0.2 ms and a peak of 40 µM)
574 (Wang et al., 2008); and (4) residual [Ca^{2+}] follows a mono-exponential function with an
575 amplitude of 1 µM and decay time constant of 50 ms (Jackson and Redman, 2003).

576 Under these assumptions and the framework of the simple refilling model, slow and delayed
577 facilitation could be replicated by modeling k_1 as $k_1 = k_{1,b} + K_{1,max} \times$ [Syt7: n Ca^{2+}], where
578 [Syt7: n Ca^{2+}] represents the fraction of fully Ca^{2+}-bound Syt7 (***Figure 9A-C***). Syt7 was slowly
579 activated over the course of the stimulus train, suggesting that the cooperative binding of
580 multiple Ca^{2+} ions progressively increased the putative active form of Syt7 because of its
581 slow membrane binding/unbinding kinetics. Nevertheless, the late phase of facilitation at
582 high frequencies was predicted to be higher in the simulation than in the experiment. As
583 expected, based on the notion that sustained release during HFS is limited by site clearance
584 in the active zone (***Figure 4C***), the model/data discrepancy became more pronounced at
585 higher frequencies. Incorporating endocytic terms into the model may mitigate late-phase
586 discrepancies. Moreover, removal of the catalytic function of Syt7 in the model effectively
587 accounted for the complete loss of facilitation observed in Syt7 KD (***Figure 9D***).
588

589 *Conventional STF models involving cumulative increase in p_v of reluctant vesicles*

590 Conventional models for facilitation assume a post-AP residual Ca^{2+}-dependent step
591 increase in p_v of RRP (Dittman et al., 2000) or reluctant vesicles (Turecek et al., 2016). Given
592 that p_v of TS vesicles is close to one in the present study, an increase in p_v of TS vesicles
593 cannot account for facilitation. The possibility for activity-dependent increase in fusion
594 probability of LS vesicles (denoted as $p_{v,LS}$) should be considered in two ways depending on
595 whether LS and TS vesicles reside in distinct pools or in the same pool. Notably, strong PPD
596 at short ISI implies that $p_{v,LS}$ is near zero at the resting state. Whereas LS vesicles do not

597 contribute to baseline transmission, short-term facilitation (STF) may be mediated by
598 cumulative increase in p_v of LS vesicles that reside in a distinct pool. Because the increase in
599 $p_{v,LS}$ during facilitation recruits new release sites (increase in N), the variance of EPSCs
600 should become larger as stimulation frequency increases, resulting in upward deviation
601 from a parabola in the V-M plane, as shown in recent studies (Valera et al., 2012;
602 Kobbersmed et al., 2020). This prediction is not compatible with our results of V-M analysis
603 (***Figure 3***), showing that EPSCs during STF fell on the same parabola regardless of
604 stimulation frequencies. Therefore, it is unlikely that an increase in fusion probability of
605 reluctant vesicles residing in a distinct release pool mediates STF in the present study. For
606 the latter case, in which LS and TS vesicles occupy in the same release sites, it is hard to
607 distinguish a step increase in fusion probability of LS vesicles from a conversion of LS vesicles
608 to TS. Nevertheless, our results do not support the possibility for a gradual increase in $p_{v,LS}$
609 that occurs in parallel with STF. Strong PPD, indicative of high p_v, was consistently found not
610 only in the baseline (***Figure 2 and Figure 2—figure supplement 1***) but also during post-
611 tetanic augmentation phase (***Figure 3D***) and even during the early development of
612 facilitation (***Figure 2D-E and Figure 7***), arguing against the gradual increase in $p_{v,LS}$. One may
613 argue that STF may be mediated by a drastic step increase of $p_{v,LS}$ from zero to one, but it is
614 not distinguishable from conversion of LS to TS vesicles.
615

616 *Possible mechanisms underlying the depression-facilitation sequence*

617 Cooperative binding of multiple Ca^{2+} ions to Syt7 predicts delayed activation and a
618 progressive increase in vesicle refilling during train stimulations, resulting in delayed
619 facilitation. Combining this with a high p_v could replicate not only the slow facilitation at 5
620 Hz, but also the unique depression-facilitation sequence observed at 40 Hz (***Figure 9***). As
621 simulated by Pulido and Marty (2018), delayed facilitation can be reproduced by a high p_v in
622 combination with a low baseline occupancy of replacement sites and subsequent Ca^{2+}-
623 dependent refilling. However, whether this model is also able to replicate slow facilitation at
624 low frequencies remains to be tested. An alternative, but not exclusive, possibility for
625 delayed facilitation is that the presynaptic global Ca^{2+} itself may undergo a slow buildup
626 during a train due to the saturation of endogenous Ca^{2+}-binding proteins.

627

628 *Facilitation requires not only Syt7, but also activation of PLC-DAG signaling*

629 To gain insight into the specific molecular mechanisms underlying the vesicle-loading
630 processes, we examined the effects of pharmacological inhibitors targeting PLC and DAG
631 (***Figure 4***). Both a PLC inhibitor and a DAG analog reduced facilitation and augmentation.
632 This suggests that the progressive overfilling of docking sites with TS vesicles is supported by
633 the PLC-DAG signaling pathway and probably downstream Munc13 (Rhee et al., 2002; Lou et
634 al., 2008). Phorbol esters have been recently shown to increase the TS fraction of docked
635 vesicles by enhancing vesicle priming without affecting Ca^{2+} transients or p_v (Taschenberger
636 et al., 2016; Aldahabi et al., 2022; Papantoniou et al., 2023; Aldahabi et al., 2024). In line

637 with these findings, signaling involving PLC and DAG may support Ca^{2+}-dependent overfilling
638 of TS vesicles by enhancing molecular priming processes.
639

640 *Roles of facilitation and augmentation in working memory and related tasks*

641 Previous theoretical studies have proposed that working memory in a recurrent network
642 can be maintained in the form of augmentation at synapses (Mongillo et al., 2008) and/or
643 persistent activity of neurons in a memory ensemble (Mongillo et al., 2012). The latter can
644 be supported by short-term facilitation of recurrent excitatory synapses or disparity in STP
645 between excitatory and inhibitory synapses (Mongillo et al., 2012; Yoon et al., 2020).
646 However, whether these short-term enhancements in synaptic efficacy contribute to
647 working memory-related behaviors has not been examined. tFC is a temporal associative
648 learning task requiring temporary retention of CS information during a trace period. The
649 mPFC and hippocampus are crucial for tFC, and tFC is interfered with by a load of working
650 memory and attention distraction, implying that the tFC shares the same neural substrate
651 with other working memory tasks (Raybuck and Lattal, 2014). In the present study, tFC in
652 WT and Syt7 KD animals revealed that Syt7 deficiency in the L2/3 PCs of the mPFC impaired
653 the acquisition of trace fear memory and reduced c-Fos expression associated with tFC
654 training (***Figure 8***).
655 The acquisition of trace fear memory was impaired by inhibition of persistent activity in
656 mPFC during trace period (Gilmartin et al., 2013). The similar deficit observed in Syt7 KD
657 animals is consistent with the hypothesis that STF provides bi-stable ensemble activity in a

658 recurrent network (Mongillo et al., 2012). Nevertheless, alternative mechanisms may be
659 responsible for the behavioral deficit. Not only recurrent network but also long-range loop
660 between the mPFC and the mediodorsal (MD) thalamus play a critical role in maintaining
661 persistent activity within the mPFC especially for a delay period longer than 10 s (Bolkan et
662 al., 2017). Prefrontal L2/3 is heavily innervated by MD thalamus, and L2/3-PCs subsequently
663 relay signals to L5 cortico-thalamic (CT) neurons (Collins et al., 2018). Given that L2/3 is an
664 essential component of the PFC-thalamic loop, loss of STF at recurrent synapses between
665 L2/3 PCs may lead to insufficient L2/3 inputs to L5 CT neurons and failure in the reverberant
666 PFC-MD thalamic feedback loop. Therefore, not only L2/3 recurrent network but also its
667 output to downstream network should be considered as a possible network mechanism
668 underlying behavioral deficit caused by Syt7 KD L2/3.
669 In summary, activity-dependent synaptic facilitation and augmentation at prelimbic L2/3
670 recurrent excitatory synapses can be attributed to overfilling of release sites with TS
671 vesicles. Given that the lack of short-term facilitation in L2/3 PCs impairs trace fear memory
672 acquisition, temporary maintenance of CS information during trace period may be
673 supported by an increase in the TS occupancy in presynaptic terminals of CS-representing
674 neuronal ensembles.
675

Materials and Methods

Animals/Subjects

All experiments were carried out on Sprague-Dawley rats of either sex at p28-43. Rats were maintained in temperature-controlled rooms on a constant 12 h light/12 h dark cycle and were given access to water and food ad libitum. All animal procedures were approved and performed in accordance with the Institutional Animal Care and Use Committee at Seoul National University (SNU200522-1).

In utero electroporation (IUE)

Pregnant Sprague Dawley rats on embryonic day (E) 17.5 were deeply anesthetized with 5% (v/v) isoflurane for the duration of surgery. The uterine horns were exposed by laparotomy and wet with warm sterile phosphate-buffered saline (PBS). The plasmids (0.5-2 μg/μl) together with the 0.01% fast green dye were injected into either the left or the right lateral ventricle or bilateral ventricles of embryos through a thin glass capillary (Narishige PC-10). The embryo's head was carefully held between the forceps-shaped electrodes of 10 mm diameter (CUY65010; NEPAGENE, Japan). Electroporation pulses (50 V for 50 ms) were delivered five times at intervals of 150 ms using a square-wave generator (ECM830; BEX, United States). The uterine horns were placed back into the abdominal cavity and abdominal muscles and skin were sutured. After the surgery, the animals were recovered under the infrared lamp. For knockdown experiments in slice electrophysiology, the shRNA constructs were co-electroporated with the pCAG-oChIEF-tdTomato, because of the

697 consistent co-expression of the two constructs in a significant proportion of the transfected
698 cells in vivo (Bony et al., 2013). Pups with robust fluorescence signals in the prefrontal
699 cortex of both hemispheres were used for behavior experiments.
700

701 *Preparation of vector constructs*

702 For an optic stimulation, pCAG-oChIEF-tdTomato was transfected by IUE. Short hairpin RNA
703 (shRNA) against Syt7 sequence (GATCTACCTGTCCTGGAAGAG) was expressed under the
704 control of an U6 promoter of pAAV-U6-GFP vector (Cell Biolabs, #VPK-413). This shRNA was
705 shown to effectively knockdown Syt7 in cell cultures and in vivo by previous reports from
706 more than one research group (Bacaj et al., 2013; Li et al., 2017). Scrambled control
707 sequence (TCGCATAGCGTATGCCGTT) was designed by shuffling the recognition region
708 sequences and a BLAST analysis confirmed that the control shRNA sequence had no target
709 gene. For rescue experiments, the cDNA for rat Syt7 (NM_021659) rendered resistant to the
710 shRNA were inserted in the KD vector and their expression was driven by the CAG promoter;
711 the vector also contained a self-cleaving P2A peptide sequence followed by EGFP, which
712 ensures visualization of transfected cells. All the constructs above were verified by DNA
713 sequencing. Plasmid DNA was purified and concentrated under endotoxin free conditions
714 (Qiagen EndoFree Maxi Kit).
715

716 *Slice preparation*

717 Acute brain slices were prepared by using a VT1200S Vibratome (Leica Microsystems) after
718 isoflurane anesthesia and decapitation. Coronal sections of the mPFC (300 µm in thickness)
719 were cut in ice-cold artificial cerebrospinal fluid (aCSF) composed of (in mM) 125 NaCl, 3.2
720 KCl, 25 $NaHCO_3$, 1.25 NaH_2PO_4, 20 D-glucose, 2 NaPyr, 1 $MgCl_2$, and 1.3 $CaCl_2$ (Yoon et al.,
721 2020), bubbled with 95% O_2 and CO_2 (pH = 7.3; 310 mOsm). Slices were allowed to recover
722 for a minimum of 30 minutes at 36 °C, and subsequently maintained at room temperature
723 until recording. Composition of aCSF was identical throughout the preparation, incubation,
724 and recording periods unless otherwise stated. For the recordings, the mPFC slices were
725 continuously perfused with oxygenated aCSF at a flow rate of 1.5 ml/min, and the
726 temperature was maintained at 31–32 °C using an in-line temperature controller (Warner
727 Instruments).

728

729 *Electrophysiology*

730 Whole-cell patch-clamp recordings were performed from pyramidal cells and fast-spiking
731 interneurons in layer 2/3 of the prelimbic mPFC. Neuronal subtypes were initially selected
732 based on morphology under visual guidance by using an upright microscope equipped with
733 infrared differential interference contrast (IR-DIC) optics (BX51WI, Olympus), and were
734 further identified by their electrophysiological properties (see ***Figure 1—figure supplement***
735 ***1***; van Aerde and Feldmeyer, 2015; Tremblay et al., 2016). To analyze these intrinsic
736 properties in current-clamp experiments, we measured the following parameters: (1)

737 resting membrane potential (RMP), (2) input resistance (R_{in}), (3) sag ratio, and (4) the F-I
738 curve, which plots firing frequencies (F) against the amplitude of injected currents (I). Both
739 cell types exhibited a low sag ratio below 0.1, consistent with findings from other studies
740 (van Aerde and Feldmeyer, 2015; Yoon et al., 2020). PCs and FSINs were easily distinguished
741 by their unique firing frequency, Rin, spike adaptation, RMP and morphological
742 characteristics including the shape of soma and the thickness of apical dendrites. For
743 experiments involving oChIEF-expressing neurons in WT or Syt7 KD rats, whole-cell
744 recordings were performed from the fluorescently labeled pyramidal neurons in layer 2/3 of
745 the prelimbic cortex using suitable filter sets. Patch pipettes (tip resistance of 2–3 MΩ) were
746 pulled from borosilicate glass and filled with (in mM) 130 K-gluconate, 8 KCl, 10 HEPES, 0.2
747 EGTA, 20 Na_2Pcr, 0.3 Na_2GTP, 4 MgATP. Intracellular solutions were adjusted to pH 7.25 and
748 300–310 mOsm. Neurons were voltage clamped at −78 mV and series resistance (Rs) were
749 continuously monitored during the EPSCs recordings. Experiments were discarded before
750 analysis if the Rs changed by 20% or larger deviation of baseline value. Measurements were
751 not corrected for Rs compensation, bridge balance, or liquid junction potential.
752 Electrophysiological data were low-pass-filtered at 1 kHz (Bessel) and acquired at 20 kHz
753 using a Multiclamp 700B amplifier paired with Digidata 1440A digitizer and Clampex 10.2
754 software (Molecular Devices).
755

756 *Synaptic stimulation*

757 IUE resulted in sparse expression of channelrhodopsin (10-20%) (***Figure 1A***). Exploiting the
758 sparse expression, we employed a minimal optical stimulation method to activate a single or

759 very few excitatory synapses in layer 2/3. The optic minimal stimulation was performed by
760 our published protocol with minor modifications (Yoon et al., 2020). This approach aimed to
761 minimize the risk of synaptic contamination, which could arise from engaging extra
762 terminals that were initially inactive (depolarized below threshold) but became active by
763 temporal summation during high-frequency trains. It also helped prevent the buildup of
764 depolarization at the synaptic terminals, which might influence the probability of release, as
765 noted by (Jackman et al., 2014). To achieve this, we employed a collimated digital
766 micromirror device (DMD)-coupled LED (Polygon400; Mightex Systems) to confine 470 nm
767 blue light to a small area with a radius of approximately 3–8 µm (typically 3–4 µm), as
768 measured at the focal plane of a 60× water immersion objective [numerical aperture (NA) =
769 1.0; LUMPlanFL, Olympus] (***Figure 1—figure supplement 3A***). To find the minimal
770 stimulation area, the radius of illumination area was increased from 2 µm by 50% at each
771 step (***Figure 1—figure supplement 3A***), and selected the smallest illumination area that
772 elicited EPSCs. Setting the duration of illumination between 3 and 5 ms (typically 5 ms),
773 photostimulation onto oChIEF-expressing cells reliably induced action potentials (APs)
774 during 600-pulse trains (see ***Figure 1—figure supplement 2***).
775 STP at various stimulus frequencies (5, 10, 20, and 40 Hz) was examined using 20-pulse
776 trains. Trials of train stimulation were repeated with a prolonged interval of 30 s to avoid
777 change in baseline properties. We observed no systematic changes in the amplitudes of the
778 first EPSC of each train, nor did we find significant differences in the paired-pulse ratio (PPR)
779 across stimulation trials in the same cell. For each stimulus frequency, approximately ten to
780 twenty consecutive traces were collected and then averaged across trials to yield a mean

781 EPSC trace. For recovery experiments, two consecutive trains of 3 or 30 stimuli at 40 Hz,
782 with varying time intervals (0.1-10 s), were applied every 10 s or 60 s, respectively, at both
783 excitatory synapses. For 600-stimulus trains at 10Hz, the trial was delivered only once for
784 each cell to avoid possible after-effects caused by prolonged synaptic stimulation (Hirsch
785 and Crepel, 1990). Prior to the stimulus trains, the EPSCs were normalized to the mean
786 amplitude of the baseline. For the baseline measurements, paired pulses with various ISIs
787 (20-200 ms) were delivered every 3 s (1/3 Hz) at least 20 times.
788 For all recordings, picrotoxin (PTX, 10 µM) was included in the recording solution to isolate
789 glutamatergic responses. mPFC PC terminals were entirely glutamatergic as the application
790 of 6-cyano-7-nitroquinoxaline-2,3-dione (CNQX, 20 µM), an AMPA receptor antagonist,
791 completely abolished the monosynaptic events evoked by photostimulation. A low
792 concentration of PTX was employed to minimize the relieving effects on spike suppression
793 caused by blockade of GABAa receptors. We confirmed that no synaptic response was
794 elicited by electrical stimulation in the presence of both 10 µM PTX and 20 µM CNQX.
795 In ***Figure 1—figure supplement 4A***, 1 µM TTX (1 mM stock solution) and 0.1 mM 4-AP (500
796 mM stock solution) were added to the bath solution to block action potentials and restore
797 presynaptic glutamate release, respectively (***Figure 1—figure supplement 4***). In ***Figure 1—***
798 ***figure supplement 5A***, 50 µM of cyclothiazide, a positive allosteric modulator of the AMPA
799 receptors, was included to minimize rapid desensitization of the postsynaptic receptors. In
800 ***Figure 1—figure supplement 5B***, 0.5 mM kynurenate was added to bath solution to prevent
801 possible saturation of AMPA receptors, especially during maximal synaptic facilitation. For
802 pharmacological manipulations of synaptic vesicle dynamics (***Figure 4***), drugs related to

803 vesicle supply including U73122, OAG, LatB, EGTA-AM, and dynasore at indicated
804 concentrations were added to the recording solution during baseline measurements or
805 PTA/recovery experiments (IBI = 0.5 s). Chemicals were from Sigma-Aldrich, Merck, or
806 Tocris.
807

808 *Measurements of quantal size*

809 Experiments for measuring asynchronous release were performed as previously described
810 (Yoon et al., 2020). In brief, we replaced extracellular Ca^{2+} entirely with 2 mM Sr^{2+} to induce
811 asynchronous release. A single stimulus was delivered at 3-second intervals over 100
812 repetitions, and asynchronous release events were detected during a 100-ms window
813 starting 25 ms after stimulus onset for each trial. The same procedure was also executed
814 under sham conditions (0% light intensity) to serve as a control, thus mitigating
815 contamination from nonspecific spontaneous events and potential errors associated with in
816 the detection algorithm. q was determined as the mean value from the first Gaussian
817 function after fitting the EPSC distribution with either a single or double Gaussian function
818 (***Figure 3—figure supplement 1***).
819

820 *Estimation of Ca^{2+} kinetics at axonal boutons*

821 Cytosolic [Ca^{2+}] at single axonal boutons was estimated by employing the two-dye, dual-
822 excitation wavelength technique as described by (Oheim et al., 1998). This method involves
823 measuring the fluorescence ratio of a Ca^{2+}-sensitive dye to that of a Ca^{2+}-insensitive dye to

824 correct for dye concentrations. We used Fluo-5F at concentrations of 150, 250, or 500 μM
825 (dissociation constant, K_d = 2.3 μM) as the calcium indicator dye and Alexa Flour 555 (50
826 μM) as the reference dye. The fluorophores were from Invitrogen. Both dyes were co-
827 loaded into presynaptic terminals of layer 2/3 pyramidal cells in mPFC through whole-cell
828 patch clamp. Before data acquisition, the dyes were allowed to diffuse to terminal boutons
829 for at least 30 minutes after the patch break-in, a duration sufficient for the equilibrium of
830 dye concentrations between the soma and its axonal terminals.
831 Calcium imaging was performed by sequentially exciting Fluo-5F and AF555 at wavelengths
832 of 473 and 559 nm, respectively, using a confocal laser-scanning microscope (FV1200;
833 Olympus, Japan) equipped with a 60× water immersion objective (NA, 0.9; LUMPlanFl;
834 Olympus, Tokyo, Japan). Once a single axonal bouton was identified, lines for scanning were
835 drawn across boutons, oriented perpendicular to the axon (***Figure 2—figure supplement***
836 ***2A-B***). After baseline fluorescence was measured, line scanning was proceeded while a
837 single or train APs were induced by applying current pulses. Upon stimulation, green
838 fluorescence but not red one increased along the vertical array of lines across the bouton
839 (***Figure 2—figure supplement 2B-C***). Measurements were obtained under current-clamp
840 conditions, with the resting potential regularly monitored. The scanning speed was adjusted
841 to 600-700 Hz by controlling the line length. Line scan for measuring fluorescent transients
842 in a bouton was repeated at least 3 times, and then averaged to enhance the signal-to-noise
843 ratio. To mitigate photobleaching, minimal intensity of the laser power and maximal pinhole
844 size were used. Emitted light was filtered through 490/590 or 575/675 bandpass filters
845 before detection by photomultiplier tubes for green or red fluorescence, respectively.

846 Fluorescence measurements were converted to $[Ca^{2+}]_i$ using the ratio of background-
847 subtracted fluorescence ($F = F_0 - F_b$) from two dyes. The fluorescence ratio ($R = F_{green}/F_{red}$) in
848 data traces were converted to $[Ca^{2+}]_i$ using the following equation:

849 $$[Ca^{2+}]_i = K_d \times (R - R_{min}) / (R_{max} - R). \quad (1)$$

850 Calibration parameters were obtained using an in-cell calibration protocol (Helmchen,
851 2011), wherein the minimum (R_{min}) and maximum ratio (R_{max}) values were established
852 through the use of intracellular solutions containing 10 mM EGTA or 10 mM $[Ca^{2+}]$,
853 respectively.

854 When Ca^{2+} is extruded with a rate constant, γ, after an AP-induced short pulse of Ca^{2+} influx
855 to a single compartment, $[Ca^{2+}]_i$ initially rises to A_{Ca} and then undergoes a mono-exponential
856 decay with a time constant (τ_{Ca}). Under this framework, A_{Ca} and τ_{Ca} depend on Ca^{2+} binding
857 ratios of endo- and exogenous Ca^{2+} buffers (denoted as κ_S and κ_B, respectively) as following
858 equations (Neher, 1995; Kim et al., 2003):

859 $$1/A_{Ca} = (1 + \kappa_S + \kappa_B) / \Delta[Ca^{2+}]_T. \quad (2)$$

860 $$\tau_{Ca} = (1 + \kappa_S + \kappa_B) / \gamma. \quad (3)$$

861 , where $\Delta[Ca^{2+}]_T$ is an increment in total $[Ca^{2+}]$ (free plus bound) elicited by an AP. Ca^{2+}
862 binding ratio indicates the ratio of concentration changes in the Ca^{2+}-buffer complex relative
863 to free $[Ca^{2+}]$ change, and linearized κ_B is calculated from the dye concentration and the
864 change from $[Ca^{2+}]_1$ to $[Ca^{2+}]_2$ as follows:

865 $$\kappa_B = \Delta[CaB] / \Delta[Ca^{2+}] = [B]_t K_d / [([Ca^{2+}]_1 + K_d)([Ca^{2+}]_2 + K_d)]. \quad (4)$$

866 The total dye concentration, $[B]_t$, was taken as [Fluo-5F] in the patch pipette. With κ_B
867 determined from Equation 4 and τ_{Ca} from the decay of a Ca^{2+} transient, κ_S can be estimated

868 by plotting τ versus κ_B and applying a linear fit to the plot, which gives the x-intercept as -(1

869 + κ_S). Once determined, κ_S can be used to calculate $\Delta[Ca^{2+}]_T$.

870

871 *Optimization of k_1 and p_v from failure rates*

872 Let n_0 = the number of docked SVs before arrival of a first AP; n_1 = the number of docked

873 SVs remaining after a first AP (i.e. n_0 - n_1 vesicles are released); n_2 = the number of docked

874 SVs just before arrival of a 2nd AP (ISI = 20 ms; ***Figure 3—figure supplement 2***). If the

875 number of release sites (N), forward and reverse rates for vesicle docking (k_1 and b_1,

876 respectively), mean release site occupancy (p_{occ}) and vesicular fusion probability upon an AP

877 (p_v) are given, we can predict $P(n_0, n_1, n_2)$, the probability for $[n_0, n_1, n_2]$, as following steps.

878 1) Probability for a synapse harbouring n_0 docked SVs just before arrival of a first AP is

879 calculated as:

880 $$P(n_0) = C(N, n_1)\, p_{occ}^{n0} \times (1 - p_{occ})^{(N-n0)}.$$

881 2) Probability that n_1 vesicles remain after a first AP when the initial number of docked SVs

882 is n_0 $[P(n_1|n_0)]$ is calculated as:

883 $$P(n_1|n_0) = C(n_0, n_1) \times (1-p_v)^{n1} \times p_v^{(n0-n1)}, \text{ if } n_0 \geq n_1 ,$$

884 $$P(n_1|n_0) = 0, \text{ if } n_0 < n_1.$$

885 3) When forward and backward rate constants are k_1 and b_1, respectively, probability that n_2

886 vesicles are docked just before arrival of a 2nd AP when n_1 SVs remain after a 1st AP (Δt = 20

887 ms) $[P(n_2 \mid n_1)]$ is predicted as follows: Assuming that docking and undocking follow a

888 Poisson process,

$$P(n_2|n_1) = \Sigma_{j=0..n1} C(n_1, j)\, C(o_1, i+j)\, B^j (1-B)^{n1-j} F^{i+j} (1-F)^{o1-i-j} \cdot \mathbf{1}_{0 \le (i+j) \le o1}.$$

, where $B = 1 - \exp(-b_1 \Delta t)$; $F = 1 - \exp(-k_1 \Delta t)$; $i = n_2 - n_1$; $o_1 = N - n_1$.

4) Combining probabilities calculated from above three steps, we can calculate $P(n_0, n_1, n_2)$:

$$P(n_0, n_1, n_2) = P(n_0) \times P(n_1|n_0) \times P(n_2|n_1)$$

5) Once $P(n_0, n_1, n_2)$ is given, we can predict probability for double failure (P_{00}) and probability for the 1st success and the 2nd failure (P_{10}) as:

$$P_{00} = \Sigma_{n0=0..N}\, \Sigma_{n1 = n0}\, \Sigma_{n2 = 0..N} \quad p(n_0, n_1, n_2)\, (1 - p_v)^{n2} .$$

$$P_{10} = \Sigma_{n0=0..N}\, \Sigma_{n1 \neq n0}\, \Sigma_{n2 = 0..N} \quad p(n_0, n_1, n_2)\, (1 - p_v)^{n2} .$$

6) Probability for the 1st failure and the 2nd success (P_{01}) and probability for double success (P_{11}) were calculated as:

$$P_{01} = P(F_1) - P(F_1, F_2)$$

$$P_{11} = P(S_1) - P(S_1, F_2)$$

, in which $P(F_1)$ and $P(S_1)$ are probability for the 1st failure and the 1st success, respectively, and these are calculated as:

$$P(F_1) = P(n_0)\, P(F_1 \mid n_0) = \Sigma_{n0=0..N} P(n_0)\, (1 - p_v)^{n0} ,$$

$$P(S_1) = 1 - P(F_1).$$

To optimize k_1 and p_v, we used the Matlab routine, *fmincon*, in which the sum of squared errors (= observed value minus predicted value) was set as a cost function to be minimized. Lower and upper bounds for k_1 and p_v were set as [4, 8] and [0.8, 1], respectively. Release probability (p_r) was calculated from the observed 1st failure rate, $P(F_1)$, as

$$p_r = 1 - [P(F_1)]^{(1/N)}$$

910 N was assumed to be six as shown in ***Figure 3***. Other parameters (b_1, and p_{occ}) were set
911 according to following relationships:

912 $$p_{occ} = p_r / p_v .$$

913 $$b_1 = k_1 (1 - p_{occ})/p_{occ} .$$

914

915 *Calculation of probability for double failure*

916 Double failure probability, P_{00}, can be more easily predicted. By the Bayes rule,

917 $$P(F_1, F_2) = \Sigma_{n2=0..N} \Sigma_{n1=0..N} P(F_2|n_2) P(n_2|n_0) P(F_1|n_0) P(n_0)$$

918 , where F_1 and F_2 means 1st and 2nd failure, because $n_0 = n_1$ after the 1st failure. $P(F_1)$ and N
919 are observed values. For calculation in ***Figure 3—figure supplement 2***, k_1 and p_v were set
920 free variables. Other parameters were set under the following constrains: $P(F_1) = (1 – p_r)^N$, p_r
921 $= p_v p_{occ}$, and $p_{occ} = k_1 / (k_1 + b_1)$.

922

923 *Behavioral tests*

924 **Trace fear conditioning**: For trace fear conditioning (tFC) (Gilmartin et al., 2013), individual
925 rats were placed in the training chamber (30.5 x 25.4 x 30.5 cm; Coulbourn Instruments)
926 consisting of metal grid floor connected to an electrical stimulator (H10-11R-TC-SF,
927 Coulbourn Instruments) for delivery of a footshock. After a 5 min habituation period, rats
928 received five pairings of a 20 s tone conditioned stimulus (CS, 2.5 kHz, 75 dB), followed by
929 empty 20s trace period and a unconditioned stimulus (US; 1 s, 0.7 mA footshock) with a
930 pseudorandom inter-trial interval (ITI) of 240 ± 20 s. During this training session, rats learned

931 to associate the auditory CS with the shock US. The next day, the rats were tested for
932 memory of CS-US trace association (called tone test). The acquisition of fear learning, often
933 indicated by the extent of freezing to the CS, was assessed in a novel chamber (a white
934 hexagonal enclosure) in a dimly lit room. During this tone (or retrieval) test, rats were first
935 allowed to explore the new context for 5 min (habituation), followed by twelve 20 s CS
936 presentations with a variable ITI of 120 ± 20 s. This entire session was repeated on the next
937 day for assessment of extinction learning. Identities of the chambers were also determined
938 with the presence of distinct odors; the training and testing chambers were cleaned with
939 70% ethanol and 1% acetic acid respectively before and after each session. For all
940 experimental sessions, the activity of animals in the chambers was recorded at 30 frames
941 per second using the EthoVision XT (Noldus Information Technology, Wageningen,
942 Netherlands), and stored as a video file. The freezing behavior, defined as behavioral
943 immobility other than respiratory movement, was assessed using an open-source video
944 analysis pipeline ezTrack (Pennington et al., 2019). The percentage of freezing was
945 calculated as a total duration of freezing divided by the total duration of observation.
946 **Elevated Plus Maze**: Elevated plus maze (EPM) test was performed using a plus-shaped
947 apparatus elevated 60 cm above the ground. The maze consisted of two open arms (50 x 10
948 x 0.5 cm (H)), two closed arms (50 x 10 x 40 cm (H)) and a center area (10 x 10 cm). Rats
949 were individually placed on the center area, facing an open arm, and the path of the animal
950 was recorded with a video camera for 5 min. We analyzed the total distance traveled for 5
951 min and time spent in each arm. Animals were tracked offline using the open-source
952 tracking system ezTrack (Pennington et al., 2019).

953 **Open field test**: Open field exploration test (OFT) was performed in an open field apparatus
954 in a dimly lit room. The open field consisted of a white plastic board (1.20 m in diameter)
955 surrounded by white plastic walls (50 cm in height). Individual rats were placed in a center
956 zone (0.6 m in diameter), and allowed to freely explore the apparatus for 10 min. Time
957 spent in the center zone and total distance traveled were analyzed for initial 5 min. Animals
958 were tracked offline using the open-source tracking system ezTrack (Pennington et al.,
959 2019).
960

961 *Histology and immunohistochemistry*

962 At the end of the behavioral experiments, rats were anesthetized using isoflurane inhalation
963 and transcardially perfused with PBS followed by 4% paraformaldehyde (PFA, T&I, Korea).
964 Brains were extracted and post-fixed in 4% PFA solution for 24 h. Perfused brains were
965 sliced at 100 μm for estimation of GFP expression or 50 μm for immunohistochemistry. For
966 analysis of c-Fos expression, rats were returned to their home cages immediately after the
967 training session and perfused approximately 90 minutes later (Arime and Akiyama, 2017).
968 Brains were then cryopreserved, frozen, and sectioned coronally. Immunofluorescence
969 staining was conducted on free-floating slices using a rabbit monoclonal anti c-fos (1:1000,
970 Cell Signaling Technology, cat# 2250s) and mouse monoclonal anti-GAD67 (1:500, Millipore,
971 cat# mab5406). Fluorescent secondary antibodies included Cy5-conjugated goat anti-rabbit
972 IgG (1:1000, Abcam, cat# ab97077) and Cy3-conjugated goat anti-mouse IgG (1:1000,
973 Abcam, cat# ab97035). Brain slices were permeabilized and blocked with PBS containing
974 0.5% Triton X-100 and 5% normal goat serum (NGS) for 1h at room temperature. Slices were

incubated overnight at 4 °C with primary antibodies, followed by 4 h incubation with secondary antibodies at room temperature. Slices were then mounted with Antifading Mounting medium (Abcam, cat# ab104139). Confocal images were acquired using a Leica TCS SP8 microscope set to the same laser intensity and acquisition parameters to compare the immunosignals in sections from Scr and Syt7 KD groups. For cell counting and colocalization, fluorescent protein-positive cells were automatically quantified with spot-detection algorithms in Imaris 9.5 (Oxford instruments).

Data analysis

Data were analyzed and presented using ClampFit (Molecular Devices), Igor Pro (Wavemetrics), MATLAB (Mathworks), and Prism (GraphPad). Data points and error bars represent the mean ± standard error of the mean. All statistical analyses were conducted using two-tailed comparisons. Sample sizes and statistical tests for each group are detailed in the figure legends.

Numerical integration of the simple refilling model

This model posits reversible docking of vesicles at finite release sites (N_{max}) with forward (k_1) and reverse rate constants (b_1) (Hosoi et al., 2007; Neher and Sakaba, 2008).

$$\underset{b_1}{\overset{k_1}{\rightleftharpoons}} n \xrightarrow{p_v}$$

994 According to this scheme, $dn/dt = k_1\ u - b_1\ n - p_v\ n\ \delta(t - t_{AP})$, where u is the number of
995 unoccupied sites (= $N_{max} - n$); t_{AP} is the timing of AP firing; and δ is the Dirac delta function.
996 The p_v was assumed to be unity (***Figure 3—figure supplement 2***). The sum of basal k_1 (= $k_{1,b}$)
997 and b_1 was be estimated as 23/s from the dependence PPR on ISIs (***Figure 3—figure***
998 ***supplement 2Ab***). From the baseline occupancy of 0.3 and $p_{occ} = k_{1,b} / (k_{1,b} + b_1)$, we could
999 estimate baseline k_1 and b_1 as 6.9/s, and 16.1/s, respectively. Ca^{2+}- and Syt7-dependent
1000 increase of k_1 was modeled as $k_1 = k_{1,b} + K_{1,max}$ [Syt7: n Ca^{2+}], where [Syt7: n Ca^{2+}] represents
1001 the fraction of full Ca^{2+}-bound Syt7. For deterministic simulations, we time-integrated a set
1002 of differential equations for each model using Euler methods with a time step of 1 ms. All
1003 calculations were performed on the platform of Matlab (R2022b, Mathworks, USA).
1004
1005 *Material availability statement*

1006 All data generated or analyzed during this study are included in the manuscript and
1007 supporting files. Source data files are provided in this paper. Matlab codes for the analyses
1008 and simulation are presented in this paper.
1009
1010

Acknowledgements

We thank Dr. E. Neher and Dr. A. Marty for critical reading of this manuscript and invaluable comments.

Author contributions

All experiments were carried out at cell physiology lab under Y.K and S.H.L's supervision. Conception or design of the work: J.S. and S.H.L. Acquisition, analysis or interpretation of data for the work: J.S, Y.K. and L.S.H. Drafting the work or revising it critically for important intellectual content: J.S., S.Y.L, Y.K. and L.S.H.

Funding

This study was supported by grants from the National Research Foundation of Korea (RS-2024-333669 to S-H. Lee; 2021R1I1A1A01059646 to Y. Kim), and Seoul National University Hospital (2024).

1027 Figure legends

1028 **Figure 1. Frequency-dependence of short-term synaptic plasticity at prelimbic L2/3**
1029 **excitatory synapses.**

1030 (**A**) In utero electroporation following injection of the plasmid (CAG-oChIEF-tdTomato) into
1031 the ventricle of an embryo (E17.5). (**B**) Representative images showing specific expression of
1032 oChIEF-tdTomato in L2/3 pyramidal cells after IUE. The red fluorescence of tdTomato clearly
1033 visualizes oChIEF-expressing cell bodies in L2/3 and axons in L5. Scale bar: 1 mm, 100 μm, 50
1034 μm from left to right. (**C**) Recording schematic showing photostimulation of oChIEF-
1035 expressing axon fibers of transfected PCs (*filled triangles*) and a whole-cell recording from
1036 non-transfected PCs (*empty triangles*) or FSINs (*empty circles*). A collimated DMD-coupled
1037 LED was used to confine the area of excitation (typically 3–4 μm in diameter) to a small
1038 region (*blue circle*) near the soma. (**D, E**) Representative traces for EPSCs averaged over 10
1039 trials at each frequency (*left*) and average amplitudes of baseline-normalized EPSCs (*right*)
1040 during 20-pulse trains at frequencies from 5 to 40 Hz at PC-PC (*D*; n = 12, 9, 21, 10 cells for 5,
1041 10, 20, 40 Hz, respectively) and PC-FSIN (*E*; n = 8, 9, 10, 10) synapses. Each data point was
1042 normalized to the average of the first EPSC. (**F**) Baseline-normalized amplitudes of steady-
1043 state EPSCs ($EPSC_{ss}$; *black symbols*) and synaptic efficacy ($EPSC_{ss} \times f$; *red symbols*) as a
1044 function of stimulation frequency (*f*) at PC–PC synapses. $EPSC_{ss}$ was measured from the
1045 average of last 5 EPSCs from the 20-pulse trains (n = 12, 9, 21, 10). (**G**) Paired pulse ratio
1046 (PPR) as a function of inter-spike intervals (n = 25, 9, 25, 22, 43 for 200, 100, 50, 25, 20 ms
1047 ISI, respectively) at PC-PC synapses. (**H**) $EPSC_{ss}$ and synaptic efficacy at PC-FSIN (n = 8, 9, 10,
1048 10). (**I**) PPR at PC-FSIN (n = 8, 9, 10, 15, 34). *Gray symbols*, individual data.
1049

1050 **Figure 2. Delayed facilitation results from slow activation of Ca^{2+}-dependent vesicle**
1051 **replenishment at a constantly high vesicular fusion probability**

1052 (**A**) Representative traces (*left*) and mean baseline-normalized amplitudes (*right*) of EPSCs
1053 evoked by 30-pulse trains at 40 Hz in control (n = 21; *black*) and in the presence of 50 μM

1054 EGTA-AM (n = 14; *green*). (**B**) Mean values for the first EPSC amplitude ($EPSC_1$, *left*) and PPR
1055 (*right*) from the experiments displayed in (A). *Gray symbols*, individual data. (**C**) Plot of rate
1056 constants for short-term facilitation ($\mathbf{k}_{STF}$) as a function of stimulation frequency (f_{stim}),
1057 showing a linear relationship. The linear regression line (*black*) is shown fitted to $\mathbf{k}_{STF}$ values,
1058 estimated from ***Figure 1***. (**D**) Representative EPSC traces (*left*) and average of baseline-
1059 normalized EPSCs (*right*) evoked by 12-pulse stimulation at 5 Hz, followed by 40 Hz 7-pulse
1060 train (n = 12). Note that slowly developing facilitation was converted to rapid facilitation
1061 after strong PPD. (**E**) Mean values for PPR at 40 Hz. The baseline PPR was reproduced from
1062 ***Figure 1G*** and the PPR during 5 Hz train was calculated as (13th EPSC) / (12th EPSC). *Gray*
1063 *symbols*, individual data. All statistical data are represented as mean ± S.E.M.; n.s. = not
1064 significant; **, P **<** 0.01; unpaired t-test.

1065

1066 **Figure 3. Low baseline occupancy of release sites and its increase during facilitation and**
1067 **post-tetanic augmentation**

1068 (**A, B**) *Left*, Representative EPSCs evoked by 5 and 40 Hz train stimulation (*black*, 5 Hz;
1069 *purple*, 40 Hz). *Right*, Variance-mean plots of EPSCs amplitude from averaged EPSCs
1070 recorded at PC-PC (A; n = 12, 17 for 5 and 40 Hz, respectively) and PC-FSIN (B; n = 8, 10)
1071 synapses. The data were fitted using multiple-probability fluctuation analysis (MPFA). Error
1072 bars are omitted for clarity. The 1st EPSC of 5 Hz train (*broken line*) was used to estimate the
1073 resting level of p_{occ}. *Filled circles* were measured from post-tetanic augmented EPSCs (*A*, n =
1074 12, 12, 9; *B*, n = 7, 7, 7 for 0.1, 0.2, 0.5 s IBIs, respectively). (**C-E**) Post-tetanic augmentation
1075 (PTA) experiments at PC-PC (*top*) and PC-FSIN (*bottom*) synapses. (**C**) Representative traces
1076 for EPSCs evoked by double 40 Hz train stimulations separated by 0.5 s. (**D**) Mean baseline-
1077 normalized amplitudes of EPSCs evoked by double 40 Hz trains at different inter-burst
1078 intervals (IBIs, 0.1, 0.2, 0.5, 1, 2, 5, 10 s). *Upper*, PC-PC synapse (n = 12, 12, 21, 11, 11, 16, 11
1079 from short to long IBIs, respectively). *Lower*, PC-FSIN synapse (n = 10, 9, 8, 9, 9, 7, 9). (**E**) PTA
1080 time course. The baseline-normalized amplitudes of 1st EPSC from the 2nd train were plotted
1081 as a function of IBIs.

1082

1083 **Figure 4. Pharmacological experiments reveal specific molecular mechanisms underlying**

1084 **vesicle loading processes**

1085 (**A-C**) (**a**) Representative EPSC traces (*left*) and mean baseline-normalized EPSCs (*right*)
1086 evoked by double 40 Hz train stimulations separated by 0.5 s inter-burst interval (IBI) in
1087 control and in the presence of 5 µM U73122 (*Aa*, n = 7, *orange*), 20 µM OAG (*Ba*, n = 12,
1088 *cyan*) or 100 µM dynasore (*Ca*, n = 10, *blue*). (**b**) Mean values for baseline EPSCs ($EPSC_1$, *left*)
1089 and augmentation (*right*) from the experiments shown in corresponding *a* panel. (**Da**)
1090 Representative EPSC traces evoked by paired pulses (*left*) and mean values for baseline EPSC
1091 amplitude (*middle*) and PPR (*right*) before and after applying 20 µM LatB (n = 6). (**Db**)
1092 Representative EPSC traces (*left, upper*) and average of normalized EPSCs (*left, lower*)
1093 evoked by double 40 Hz train stimulation separated by 0.5 s in control (n = 21) and in 20 µM
1094 LatB conditions (n = 16; *pink*). *Right*, Mean values for augmentation in control and LatB
1095 conditions. *Gray symbols*, individual data. All statistical data are represented as mean ±
1096 S.E.M., *, $P < 0.05$; **, $P < 0.01$; ***, $P < 0.001$; unpaired or paired t-test; n.s. = not
1097 significant.

1098

1099 **Figure 5. STF at both types of local excitatory synapses is abolished by Syt7 KD**

1100 (**A, B**) Representative EPSC traces (*left*) and mean baseline-normalized amplitudes of EPSCs
1101 (*right*) evoked by 20-pulse trains at 5 to 40 Hz. STP was measured at PC-PC (*A*; n = 10, 9, 12,
1102 9) and PC-FSIN (*B*; n = 9, 8, 10, 9) synapses, in which presynaptic Syt7 transcripts were
1103 depleted (Syt7 KD). Syt7 KD pyramidal cells are indicated as *black triangles* on the top. For
1104 comparison, STP in WT synapses is reproduced from ***Figure 1*** (*dotted lines*). Same frequency
1105 color codes were used as in ***Figure 1***. (**C**) Baseline-normalized amplitudes of steady-state
1106 EPSC ($EPSC_{ss}$; *black symbols*) and synaptic efficacy ($EPSC_{ss} \times f$; *red symbols*) as a function of
1107 stimulation frequency (*f*) at PC-PC synapses. $EPSC_{ss}$ was defined as the average of last 5 EPSC
1108 amplitudes from 20-pulse trains. (**D**) PPR as a function of inter-spike intervals (n = 10, 9, 12,

1109 18, 26). (**E**) $EPSC_{ss}$ and synaptic efficacy at PC-FSIN synapses. (**F**) PPR at PC-FSIN synapses (n =
1110 9, 8, 10, 12, 24). *Gray symbols*, individual data.
1111

1112 **Figure 6. Syt7 KD synapses exhibit complementary changes in the number of release sites**
1113 **and their vesicle occupancy**

1114 (**A, B**) *Left*, Representative traces of EPSCs evoked by 5 and 40 Hz train stimulations (*black*, 5
1115 Hz; *purple*, 40 Hz). *Right*, Variance-mean plots of EPSCs amplitude from averaged EPSCs
1116 recorded at PC-PC (*A*; n = 9, 15, 12, 10, 9) and PC-FSIN (*B*; n = 4, 14, 10, 9, 8) synapses in
1117 which presynaptic Syt7 has been knocked down. The data were fitted using MPFA and error
1118 bars are omitted for clarity. The mean 1st EPSC amplitude of 5 Hz train (*vertical broken line*)
1119 was used for estimation of baseline p_{occ}. Dashed parabolas indicate MPFA fits to variance-
1120 mean plot of WT synapses reproduced from ***Figure 3***. (**C-E**) Recovery experiments at PC-PC
1121 (*top*) and PC-FSIN (*bottom*) synapses in which presynaptic Syt7 was knocked-down. (**C**)
1122 Representative EPSCs evoked by double 40 Hz train stimulations separated by 0.5 s. (**D**)
1123 Mean baseline-normalized amplitudes of EPSCs evoked by double 40 Hz trains at PC-PC (n =
1124 12, 10, 9, 9, 10, 9, 8) and PC-FSIN (n = 10, 9, 10, 11, 8, 9, 10) synapses at different interburst
1125 intervals (IBIs). (**E**) Recovery time course. Baseline-normalized amplitudes of 1st EPSC from
1126 the 2nd burst were plotted as a function of various IBIs. *Dotted lines* indicate augmented
1127 EPSCs in the WT reproduced from ***Figure 3***.
1128

1129 **Figure 7. Recovery of TS vesicles following depletion is accelerated by Syt7**

1130 (**A-C**). Recovery experiments at PC-PC synapses in WT (*A*) and Syt7 KD (*B*). Mean baseline-
1131 normalized amplitudes of EPSCs evoked by two consecutive 3-pulse 40 Hz trains in WT (n =
1132 16, 13, 11, 11, 11, 9 from short to long IBIs, respectively) and KD (n = 13, 11, 12, 8, 10, 11)
1133 synapses at different IBIs (0.1, 0.2, 0.5, 1, 2, 5 s). *Inset*, representative traces of EPSCs
1134 evoked by two consecutive 3-pulse 40 Hz train stimulations separated by 0.2 s. (**D-F**).
1135 Recovery experiments at PC-FSIN synapses in WT (*D*) and Syt7 KD (*E*). Mean baseline-
1136 normalized amplitudes of EPSCs evoked by two consecutive 3-pulse 40 Hz trains in WT (n =

1137 9, 11, 11, 9, 10, 13) and KD (n = 9, 12, 9, 7, 10, 9) synapses at different IBIs. *Inset*,
1138 representative traces of EPSCs evoked by two consecutive 3-pulse 40 Hz train stimulations
1139 separated by 0.2 s. (**C, F**) Recovery time course. Baseline-normalized amplitudes of 1st EPSC
1140 from the 2nd burst were plotted as a function of various IBIs.
1141

1142 **Figure 8. Behavioral effects of Syt7 deficiency in L2/3 PCs of the mPFC**

1143 (**A**) *Top*, Representative images showing bilateral expression of U6-GFP in L2/3 of PCs after
1144 IUE at E17.5. Scale bar: 1 mm, 100 µm. *Bottom*, Schematic of trace fear conditioning and
1145 extinction (tone test) protocol. (**B**) Freezing behavior of control (expressing scrambled
1146 shRNA, *Scr*) and Syt7 KD rats during acquisition of tFC. (**C**) Freezing ratio during tone tests on
1147 following days. Data are shown as average freezing during T1–T4, T5–T8, or T9–T12 (T,
1148 trials). The freezing on T1-T4 was significantly lower in KD rats suggesting that formation of
1149 trace memory was impaired in Syt7 KD rats (n = 10, 11 for Ctrl and KD, respectively; P =
1150 0.0007, F(1, 19) = 16.43, two-way repeated measures ANOVA; P = 0.0064, 0.0211, 0.0064,
1151 0.0064; Holm-Sidak test). (**D**) Representative images of c-Fos immunoreactivity in the
1152 prelimbic cortex of control or Syt7 KD rats 90 min after tFC acquisition. c-Fos (*left*, *red*, Cy5)
1153 and GAD67 (*right*, *cyan*, Cy3) were immunostained in the same brain slice expressing U6-
1154 GFP (*middle*; *green*). Scale bar, 50 µm. (**E**) Exemplar images of c-Fos positive neurons
1155 expressing GFP (*top*) or GAD67 (*bottom*) in control (*left*) or Syt7 KD rats (*right*). Scale bar, 50
1156 µm. (**F-H**) Effects of Syt7 KD on c-Fos density (*F*) and percentage of c-Fos positive neurons
1157 co-labeled with GAD67 (*G*) or GFP (*H*) in L2/3 or L5 of prelimbic cortex (n = 9, 9 for Ctrl and
1158 KD, respectively). *Open symbols*, individual data. All statistical data are represented as mean
1159 ± S.E.M.; ****, P **<** 0.0001; unpaired t-test.

1160

1161 **Figure 9. STP model in light of known Ca^{2+} binding kinetics of Syt7**

1162 (**A-D**) *Left*, Schematic of allosteric calcium binding to Syt7. The number of Ca^{2+} bound to Syt7
1163 was denoted as # in 'S#' in the reaction scheme. k_{on} = 7/µM/s, k_{off} = 10/s. *Middle*, Simulated
1164 changes of k_1 (*black*) in response to 5 Hz train of Ca^{2+} transients (*light blue traces*). The

1165 priming step of the simple refilling model was assumed to be catalyzed by full Ca^{2+}-bound
1166 form of Syt7. Accordingly, Ca^{2+}-dependent increase in k_1 was calculated as $K_{1,max}$ multiplied
1167 by a fraction of full Ca^{2+}-bound form of Syt7. We assumed that local $[Ca^{2+}]_i(t)$ follows a
1168 Gaussian function: $(1/\sigma\sqrt{2\pi}) \exp[-(t-t_p)^2/ 2\sigma^2]$, in which t_p = 0.25 ms and σ = 0.085 ms. *Right*,
1169 Fits of the Syt7 model to the STP data. To fit this model to the STP data, $K_{1,max}$ was set to
1170 300/s (*A*), 220/s (*B*), and 180/s (*C*). Cooperativity factor (*b*) was set to 0.35 (*A*), 0.2 (*B*), and
1171 0.05 (*C*). k_1 is set to be constant for Syt7 KD (*D*). Same frequency color codes were used as in
1172 ***Figure 1***.
1173

References

Aldahabi M, Neher E, Nusser Z (2024) Different states of synaptic vesicle priming explain target cell type-dependent differences in neurotransmitter release. Proc Natl Acad Sci U S A 121:e2322550121.

Aldahabi M, Balint F, Holderith N, Lorincz A, Reva M, Nusser Z (2022) Different priming states of synaptic vesicles underlie distinct release probabilities at hippocampal excitatory synapses. Neuron 110:4144-4161 e4147.

Arime Y, Akiyama K (2017) Abnormal neural activation patterns underlying working memory impairment in chronic phencyclidine-treated mice. PLoS One 12:e0189287.

Bacaj T, Wu D, Burre J, Malenka RC, Liu X, Sudhof TC (2015) Synaptotagmin-1 and -7 Are Redundantly Essential for Maintaining the Capacity of the Readily-Releasable Pool of Synaptic Vesicles. PLoS Biol 13:e1002267.

Bacaj T, Wu D, Yang X, Morishita W, Zhou P, Xu W, Malenka RC, Sudhof TC (2013) Synaptotagmin-1 and synaptotagmin-7 trigger synchronous and asynchronous phases of neurotransmitter release. Neuron 80:947-959.

Baeg EH, Kim YB, Huh K, Mook-Jung I, Kim HT, Jung MW (2003) Dynamics of population code for working memory in the prefrontal cortex. Neuron 40:177-188.

Bolkan SS, Stujenske JM, Parnaudeau S, Spellman TJ, Rauffenbart C, Abbas AI, Harris AZ, Gordon JA, Kellendonk C (2017) Thalamic projections sustain prefrontal activity during working memory maintenance. Nat Neurosci 20:987-996.

Bony G, Szczurkowska J, Tamagno I, Shelly M, Contestabile A, Cancedda L (2013) Non-hyperpolarizing GABAB receptor activation regulates neuronal migration and neurite growth and specification by cAMP/LKB1. Nat Commun 4:1800.

Brandt DS, Coffman MD, Falke JJ, Knight JD (2012) Hydrophobic contributions to the membrane docking of synaptotagmin 7 C2A domain: mechanistic contrast between isoforms 1 and 7. Biochemistry 51:7654-7664.

Chen C, Satterfield R, Young SM, Jr., Jonas P (2017) Triple Function of Synaptotagmin 7 Ensures Efficiency of High-Frequency Transmission at Central GABAergic Synapses. Cell Rep 21:2082-2089.

Chon NL, Osterberg JR, Henderson J, Khan HM, Reuter N, Knight JD, Lin H (2015) Membrane Docking of the Synaptotagmin 7 C2A Domain: Computation Reveals Interplay between Electrostatic and Hydrophobic Contributions. Biochemistry 54:5696-5711.

Collins DP, Anastasiades PG, Marlin JJ, Carter AG (2018) Reciprocal Circuits Linking the Prefrontal Cortex with Dorsal and Ventral Thalamic Nuclei. Neuron 98:366-379 e364.

Dittman JS, Kreitzer AC, Regehr WG (2000) Interplay between facilitation, depression, and residual calcium at three presynaptic terminals. J Neurosci 20:1374-1385.

Dobrunz LE, Huang EP, Stevens CF (1997) Very short-term plasticity in hippocampal synapses. Proceedings of the national academy of sciences 94:14843-14847.

Dodge Jr FA, Rahamimoff R (1967) Co-operative action of calcium ions in transmitter release at the neuromuscular junction. The Journal of physiology 193:419-432.

1214 Fields RD, Eshete F, Stevens B, Itoh K (1997) Action potential-dependent regulation of gene
1215 expression: temporal specificity in ca2+, cAMP-responsive element binding proteins,
1216 and mitogen-activated protein kinase signaling. J Neurosci 17:7252-7266.
1217 Fujisawa S, Amarasingham A, Harrison MT, Buzsaki G (2008) Behavior-dependent short-term
1218 assembly dynamics in the medial prefrontal cortex. Nat Neurosci 11:823-833.
1219 Garcia-Perez E, Wesseling JF (2008) Augmentation controls the fast rebound from
1220 depression at excitatory hippocampal synapses. J Neurophysiol 99:1770-1786.
1221 Gilmartin MR, Miyawaki H, Helmstetter FJ, Diba K (2013) Prefrontal activity links
1222 nonoverlapping events in memory. J Neurosci 33:10910-10914.
1223 Guzowski JF, Timlin JA, Roysam B, McNaughton BL, Worley PF, Barnes CA (2005) Mapping
1224 behaviorally relevant neural circuits with immediate-early gene expression. Curr
1225 Opin Neurobiol 15:599-606.
1226 Hallermann S, Silver RA (2013) Sustaining rapid vesicular release at active zones: potential
1227 roles for vesicle tethering. Trends Neurosci 36:185-194.
1228 Hansel D, Mato G (2013) Short-term plasticity explains irregular persistent activity in
1229 working memory tasks. J Neurosci 33:133-149.
1230 Hass CA, Glickfeld LL (2016) High-fidelity optical excitation of cortico-cortical projections at
1231 physiological frequencies. J Neurophysiol 116:2056-2066.
1232 Haucke V, Neher E, Sigrist SJ (2011) Protein scaffolds in the coupling of synaptic exocytosis
1233 and endocytosis. Nat Rev Neurosci 12:127-138.
1234 Helmchen F (2011) Calibration protocols for fluorescent calcium indicators. Cold Spring Harb
1235 Protoc 2011:980-984.
1236 Hempel CM, Hartman KH, Wang XJ, Turrigiano GG, Nelson SB (2000) Multiple forms of short-
1237 term plasticity at excitatory synapses in rat medial prefrontal cortex. J Neurophysiol
1238 83:3031-3041.
1239 Hirsch JC, Crepel F (1990) Use-dependent changes in synaptic efficacy in rat prefrontal
1240 neurons in vitro. J Physiol 427:31-49.
1241 Holler S, Kostinger G, Martin KAC, Schuhknecht GFP, Stratford KJ (2021) Structure and
1242 function of a neocortical synapse. Nature 591:111-116.
1243 Holmgren C, Harkany T, Svennenfors B, Zilberter Y (2003) Pyramidal cell communication
1244 within local networks in layer 2/3 of rat neocortex. J Physiol 551:139-153.
1245 Hosoi N, Sakaba T, Neher E (2007) Quantitative analysis of calcium-dependent vesicle
1246 recruitment and its functional role at the calyx of Held synapse. J Neurosci 27:14286-
1247 14298.
1248 Jackman SL, Regehr WG (2017) The Mechanisms and Functions of Synaptic Facilitation.
1249 Neuron 94:447-464.
1250 Jackman SL, Beneduce BM, Drew IR, Regehr WG (2014) Achieving high-frequency optical
1251 control of synaptic transmission. J Neurosci 34:7704-7714.
1252 Jackman SL, Turecek J, Belinsky JE, Regehr WG (2016) The calcium sensor synaptotagmin 7 is
1253 required for synaptic facilitation. Nature 529:88-91.
1254 Jackson MB, Redman SJ (2003) Calcium dynamics, buffering, and buffer saturation in the
1255 boutons of dentate granule-cell axons in the hilus. J Neurosci 23:1612-1621.

1256 Kim MH, Lee SH, Park KH, Ho WK, Lee SH (2003) Distribution of K+-dependent Na+/Ca2+
1257 exchangers in the rat supraoptic magnocellular neuron is polarized to axon
1258 terminals. J Neurosci 23:11673-11680.
1259 Kobbersmed JRL, Grasskamp AT, Jusyte M, Böhme MA, Ditlevsen S, Sørensen JB, Walter AM
1260 (2020) Rapid regulation of vesicle priming explains synaptic facilitation despite
1261 heterogeneous vesicle:Ca2+ channel distances. eLife 9:e51032.
1262 Kusick GF, Chin M, Raychaudhuri S, Lippmann K, Adula KP, Hujber EJ, Vu T, Davis MW,
1263 Jorgensen EM, Watanabe S (2020) Synaptic vesicles transiently dock to refill release
1264 sites. Nat Neurosci 23:1329-1338.
1265 Lee HR, Choi SH, Lee SH (2024) Differential involvement of mitochondria in post-tetanic
1266 potentiation at intracortical excitatory synapses of the medial prefrontal cortex.
1267 Cereb Cortex 34.
1268 Lee JS, Ho WK, Lee SH (2010) Post-tetanic increase in the fast-releasing synaptic vesicle pool
1269 at the expense of the slowly releasing pool. J Gen Physiol 136:259-272.
1270 Lee JS, Ho WK, Lee SH (2012) Actin-dependent rapid recruitment of reluctant synaptic
1271 vesicles into a fast-releasing vesicle pool. Proc Natl Acad Sci U S A 109:E765-774.
1272 Li YC, Chanaday NL, Xu W, Kavalali ET (2017) Synaptotagmin-1- and Synaptotagmin-7-
1273 Dependent Fusion Mechanisms Target Synaptic Vesicles to Kinetically Distinct
1274 Endocytic Pathways. Neuron 93:616-631 e613.
1275 Lin JY, Lin MZ, Steinbach P, Tsien RY (2009) Characterization of engineered
1276 channelrhodopsin variants with improved properties and kinetics. Biophys J 96:1803-
1277 1814.
1278 Lin KH, Taschenberger H, Neher E (2022) A sequential two-step priming scheme reproduces
1279 diversity in synaptic strength and short-term plasticity. Proc Natl Acad Sci U S A
1280 119:e2207987119.
1281 Lin KH, Ranjan M, Lipstein N, Brose N, Neher E, Taschenberger H (2025) Number and relative
1282 abundance of synaptic vesicles in functionally distinct priming states determine
1283 synaptic strength and short-term plasticity. The Journal of Physiology.
1284 Liu H, Bai H, Hui E, Yang L, Evans CS, Wang Z, Kwon SE, Chapman ER (2014) Synaptotagmin 7
1285 functions as a Ca2+-sensor for synaptic vesicle replenishment. Elife 3:e01524.
1286 Lou X, Korogod N, Brose N, Schneggenburger R (2008) Phorbol esters modulate
1287 spontaneous and Ca2+-evoked transmitter release via acting on both Munc13 and
1288 protein kinase C. J Neurosci 28:8257-8267.
1289 Macia E, Ehrlich M, Massol R, Boucrot E, Brunner C, Kirchhausen T (2006) Dynasore, a cell-
1290 permeable inhibitor of dynamin. Dev Cell 10:839-850.
1291 Malagon G, Miki T, Tran V, Gomez LC, Marty A (2020) Incomplete vesicular docking limits
1292 synaptic strength under high release probability conditions. Elife 9.
1293 Markram H, Wang Y, Tsodyks M (1998) Differential signaling via the same axon of
1294 neocortical pyramidal neurons. Proc Natl Acad Sci U S A 95:5323-5328.
1295 Martinetti LE, Bonekamp KE, Autio DM, Kim HH, Crandall SR (2022) Short-Term Facilitation
1296 of Long-Range Corticocortical Synapses Revealed by Selective Optical Stimulation.
1297 Cereb Cortex 32:1932-1949.
1298 Miki T, Malagon G, Pulido C, Llano I, Neher E, Marty A (2016) Actin- and Myosin-Dependent
1299 Vesicle Loading of Presynaptic Docking Sites Prior to Exocytosis. Neuron 91:808-823.

1300 Mongillo G, Barak O, Tsodyks M (2008) Synaptic theory of working memory. Science
1301 319:1543-1546.
1302 Mongillo G, Hansel D, van Vreeswijk C (2012) Bistability and spatiotemporal irregularity in
1303 neuronal networks with nonlinear synaptic transmission. Phys Rev Lett 108:158101.
1304 Neher E (1995) The use of fura-2 for estimating Ca buffers and Ca fluxes.
1305 Neuropharmacology 34:1423-1442.
1306 Neher E (2010) What is Rate-Limiting during Sustained Synaptic Activity: Vesicle Supply or
1307 the Availability of Release Sites. Front Synaptic Neurosci 2:144.
1308 Neher E (2024) Interpretation of presynaptic phenotypes of synaptic plasticity in terms of a
1309 two-step priming process. J Gen Physiol 156.
1310 Neher E, Sakaba T (2008) Multiple roles of calcium ions in the regulation of
1311 neurotransmitter release. Neuron 59:861-872.
1312 Neher E, Brose N (2018) Dynamically Primed Synaptic Vesicle States: Key to Understand
1313 Synaptic Short-Term Plasticity. Neuron 100:1283-1291.
1314 Norman CA, Krishnakumar SS, Timofeeva Y, Volynski KE (2023) The release of inhibition
1315 model reproduces kinetics and plasticity of neurotransmitter release in central
1316 synapses. Commun Biol 6:1091.
1317 Oheim M, Naraghi M, Muller TH, Neher E (1998) Two dye two wavelength excitation calcium
1318 imaging: results from bovine adrenal chromaffin cells. Cell Calcium 24:71-84.
1319 Otsuka T, Kawaguchi Y (2009) Cortical inhibitory cell types differentially form intralaminar
1320 and interlaminar subnetworks with excitatory neurons. J Neurosci 29:10533-10540.
1321 Ozdemir AT, Lagler M, Lagoun S, Malagon-Vina H, Lasztoczi B, Klausberger T (2020)
1322 Unexpected Rule-Changes in a Working Memory Task Shape the Firing of
1323 Histologically Identified Delay-Tuned Neurons in the Prefrontal Cortex. Cell Rep
1324 30:1613-1626 e1614.
1325 Pan B, Zucker RS (2009) A general model of synaptic transmission and short-term plasticity.
1326 Neuron 62:539-554.
1327 Papantoniou C, Laugks U, Betzin J, Capitanio C, Ferrero JJ, Sanchez-Prieto J, Schoch S, Brose
1328 N, Baumeister W, Cooper BH, Imig C, Lucic V (2023) Munc13- and SNAP25-
1329 dependent molecular bridges play a key role in synaptic vesicle priming. Sci Adv
1330 9:eadf6222.
1331 Pennington ZT, Dong Z, Feng Y, Vetere LM, Page-Harley L, Shuman T, Cai DJ (2019) ezTrack:
1332 An open-source video analysis pipeline for the investigation of animal behavior. Sci
1333 Rep 9:19979.
1334 Pulido C, Marty A (2018) A two-step docking site model predicting different short-term
1335 synaptic plasticity patterns. J Gen Physiol 150:1107-1124.
1336 Raybuck JD, Lattal KM (2014) Bridging the interval: theory and neurobiology of trace
1337 conditioning. Behav Processes 101:103-111.
1338 Reyes A, Sakmann B (1999) Developmental switch in the short-term modification of unitary
1339 EPSPs evoked in layer 2/3 and layer 5 pyramidal neurons of rat neocortex. J Neurosci
1340 19:3827-3835.
1341 Rhee JS, Betz A, Pyott S, Reim K, Varoqueaux F, Augustin I, Hesse D, Sudhof TC, Takahashi M,
1342 Rosenmund C, Brose N (2002) Beta phorbol ester- and diacylglycerol-induced

1343 augmentation of transmitter release is mediated by Munc13s and not by PKCs. Cell
1344 108:121-133.
1345 Ritzau-Jost A, Jablonski L, Viotti J, Lipstein N, Eilers J, Hallermann S (2018) Apparent calcium
1346 dependence of vesicle recruitment. J Physiol 596:4693-4707.
1347 Ritzau-Jost A, Delvendahl I, Rings A, Byczkowicz N, Harada H, Shigemoto R, Hirrlinger J, Eilers
1348 J, Hallermann S (2014) Ultrafast action potentials mediate kilohertz signaling at a
1349 central synapse. Neuron 84:152-163.
1350 Rozov A, Burnashev N, Sakmann B, Neher E (2001) Transmitter release modulation by
1351 intracellular Ca2+ buffers in facilitating and depressing nerve terminals of pyramidal
1352 cells in layer 2/3 of the rat neocortex indicates a target cell-specific difference in
1353 presynaptic calcium dynamics. J Physiol 531:807-826.
1354 Sakaba T, Neher E (2003) Involvement of actin polymerization in vesicle recruitment at the
1355 calyx of Held synapse. J Neurosci 23:837-846.
1356 Scheuss V, Schneggenburger R, Neher E (2002) Separation of presynaptic and postsynaptic
1357 contributions to depression by covariance analysis of successive EPSCs at the calyx of
1358 Held synapse. J Neurosci 22:728-739.
1359 Schotten S, Meijer M, Walter AM, Huson V, Mamer L, Kalogreades L, ter Veer M, Ruiter M,
1360 Brose N, Rosenmund C (2015) Additive effects on the energy barrier for synaptic
1361 vesicle fusion cause supralinear effects on the vesicle fusion rate. Elife 4:e05531.
1362 Silva M, Tran V, Marty A (2021) Calcium-dependent docking of synaptic vesicles. Trends
1363 Neurosci 44:579-592.
1364 Silva M, Tran V, Marty A (2024) A maximum of two readily releasable vesicles per docking
1365 site at a cerebellar single active zone synapse. Elife 12.
1366 Stevens CF, Wesseling JF (1999) Augmentation is a potentiation of the exocytotic process.
1367 Neuron 22:139-146.
1368 Sugita S, Han W, Butz S, Liu X, Fernandez-Chacon R, Lao Y, Sudhof TC (2001) Synaptotagmin
1369 VII as a plasma membrane Ca(2+) sensor in exocytosis. Neuron 30:459-473.
1370 Taschenberger H, Woehler A, Neher E (2016) Superpriming of synaptic vesicles as a common
1371 basis for intersynapse variability and modulation of synaptic strength. Proc Natl Acad
1372 Sci U S A 113:E4548-4557.
1373 Tawfik B, Martins JS, Houy S, Imig C, Pinheiro PS, Wojcik SM, Brose N, Cooper BH, Sorensen
1374 JB (2021) Synaptotagmin-7 places dense-core vesicles at the cell membrane to
1375 promote Munc13-2- and Ca(2+)-dependent priming. Elife 10.
1376 Thomson AM, Lamy C (2007) Functional maps of neocortical local circuitry. Frontiers in
1377 neuroscience 1:48.
1378 Tran V, Silva M, Marty A (2023) Prioritized docking of synaptic vesicles provided by a rapid
1379 recycling pathway. iScience 26:106366.
1380 Tremblay R, Lee S, Rudy B (2016) GABAergic Interneurons in the Neocortex: From Cellular
1381 Properties to Circuits. Neuron 91:260-292.
1382 Turecek J, Jackman SL, Regehr WG (2016) Synaptic Specializations Support Frequency-
1383 Independent Purkinje Cell Output from the Cerebellar Cortex. Cell Rep 17:3256-
1384 3268.
1385 Turecek J, Jackman SL, Regehr WG (2017) Synaptotagmin 7 confers frequency invariance
1386 onto specialized depressing synapses. Nature 551:503-506.

1387 Valera AM, Doussau F, Poulain B, Barbour B, Isope P (2012) Adaptation of granule cell to
1388 Purkinje cell synapses to high-frequency transmission. J Neurosci 32:3267-3280.
1389 van Aerde KI, Feldmeyer D (2015) Morphological and physiological characterization of
1390 pyramidal neuron subtypes in rat medial prefrontal cortex. Cereb Cortex 25:788-805.
1391 Vandael D, Borges-Merjane C, Zhang X, Jonas P (2020) Short-Term Plasticity at Hippocampal
1392 Mossy Fiber Synapses Is Induced by Natural Activity Patterns and Associated with
1393 Vesicle Pool Engram Formation. Neuron 107:509-521 e507.
1394 Vevea JD, Kusick GF, Courtney KC, Chen E, Watanabe S, Chapman ER (2021) Synaptotagmin
1395 7 is targeted to the axonal plasma membrane through gamma-secretase processing
1396 to promote synaptic vesicle docking in mouse hippocampal neurons. Elife 10.
1397 Voleti R, Tomchick DR, Sudhof TC, Rizo J (2017) Exceptionally tight membrane-binding may
1398 explain the key role of the synaptotagmin-7 C(2)A domain in asynchronous
1399 neurotransmitter release. Proc Natl Acad Sci U S A 114:E8518-E8527.
1400 Wang LY, Neher E, Taschenberger H (2008) Synaptic vesicles in mature calyx of Held
1401 synapses sense higher nanodomain calcium concentrations during action potential-
1402 evoked glutamate release. J Neurosci 28:14450-14458.
1403 Wu LG, Chan CY (2022) Multiple Roles of Actin in Exo- and Endocytosis. Front Synaptic
1404 Neurosci 14:841704.
1405 Yau JO, McNally GP (2023) The Rescorla-Wagner model, prediction error, and fear learning.
1406 Neurobiol Learn Mem 203:107799.
1407 Yoon JY, Lee HR, Ho WK, Lee SH (2020) Disparities in Short-Term Depression Among
1408 Prefrontal Cortex Synapses Sustain Persistent Activity in a Balanced Network. Cereb
1409 Cortex 30:113-134.
1410 Zucker RS, Regehr WG (2002) Short-term synaptic plasticity. Annu Rev Physiol 64:355-405.
1411

Figure 1

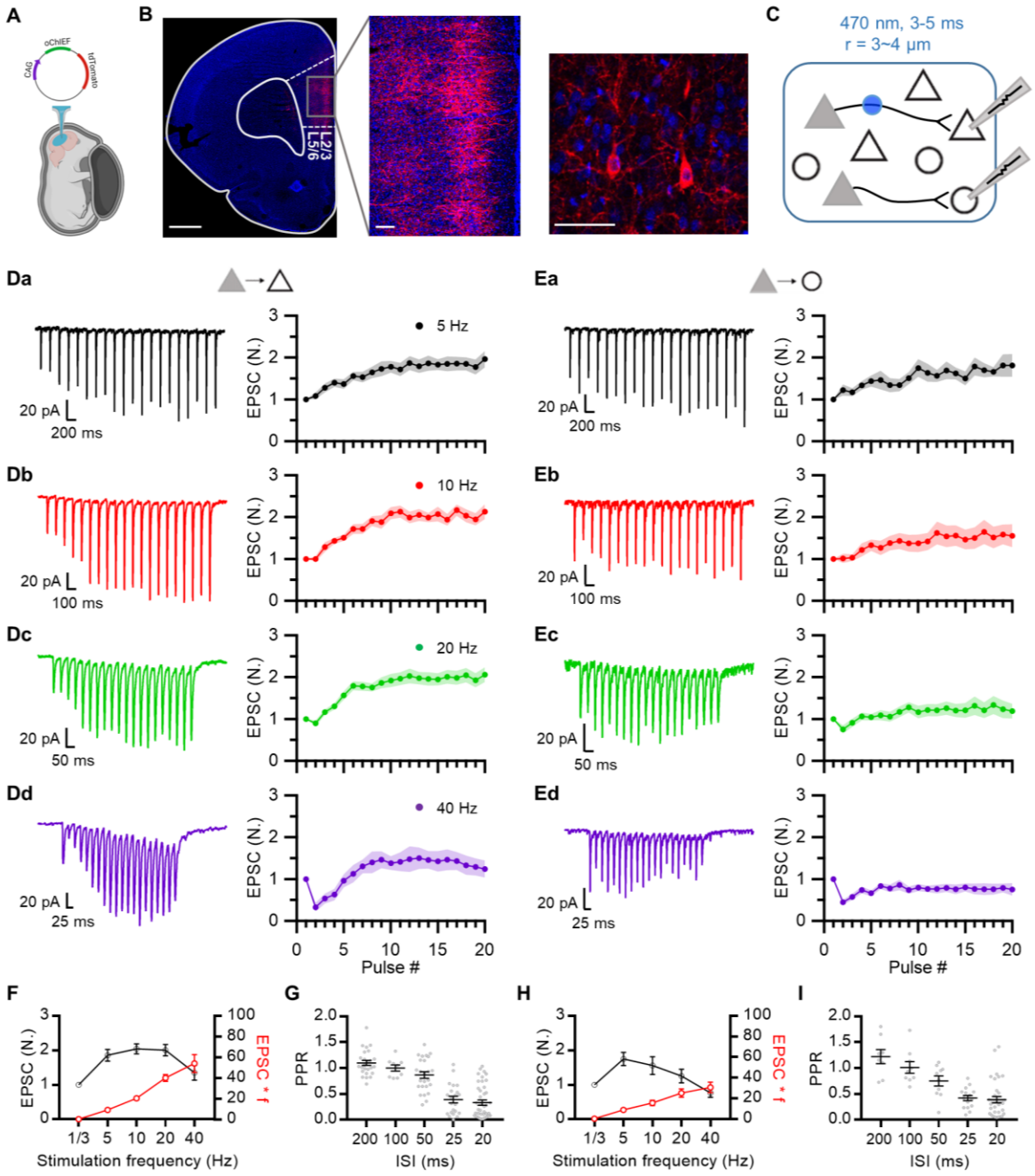

Figure 1. Frequency-dependence of short-term synaptic plasticity at prelimbic L2/3 excitatory synapses.

(**A**) In utero electroporation following injection of the plasmid (CAG-oChIEF-tdTomato) into the ventricle of an embryo (E17.5). (**B**) Representative images showing specific expression of oChIEF-tdTomato in L2/3 pyramidal cells after IUE. The red fluorescence of tdTomato clearly visualizes oChIEF-expressing cell bodies in L2/3 and axons in L5. Scale bar: 1 mm, 100 μm, 50 μm from left to right. (**C**) Recording schematic showing photostimulation of oChIEF-expressing axon fibers of transfected PCs (*filled triangles*) and a whole-cell recording from non-transfected PCs (*empty triangles*) or FSINs (*empty circles*). A collimated DMD-coupled LED was used to confine the area of excitation (typically 3–4 μm in diameter) to a small region (*blue circle*) near the soma. (**D, E**) Representative traces for EPSCs averaged over 10 trials at each frequency (*left*) and average amplitudes of baseline-normalized EPSCs (*right*) during 20-pulse trains at frequencies from 5 to 40 Hz at PC-PC (*D*; n = 12, 9, 21, 10 cells for 5, 10, 20, 40 Hz, respectively) and PC-FSIN (*E*; n = 8, 9, 10, 10) synapses. Each data point was normalized to the average of the first EPSC. (**F**) Baseline-normalized amplitudes of steady-state EPSCs ($EPSC_{ss}$; *black symbols*) and synaptic efficacy ($EPSC_{ss} \times f$; *red symbols*) as a function of stimulation frequency (*f*) at PC–PC synapses. $EPSC_{ss}$ was measured from the average of last 5 EPSCs from the 20-pulse trains (n = 12, 9, 21, 10). (**G**) Paired pulse ratio (PPR) as a function of inter-spike intervals (n = 25, 9, 25, 22, 43 for 200, 100, 50, 25, 20 ms ISI, respectively) at PC-PC synapses. (**H**) $EPSC_{ss}$ and synaptic efficacy at PC-FSIN (n = 8, 9, 10, 10). (**I**) PPR at PC-FSIN (n = 8, 9, 10, 15, 34). *Gray symbols*, individual data.

Figure 2

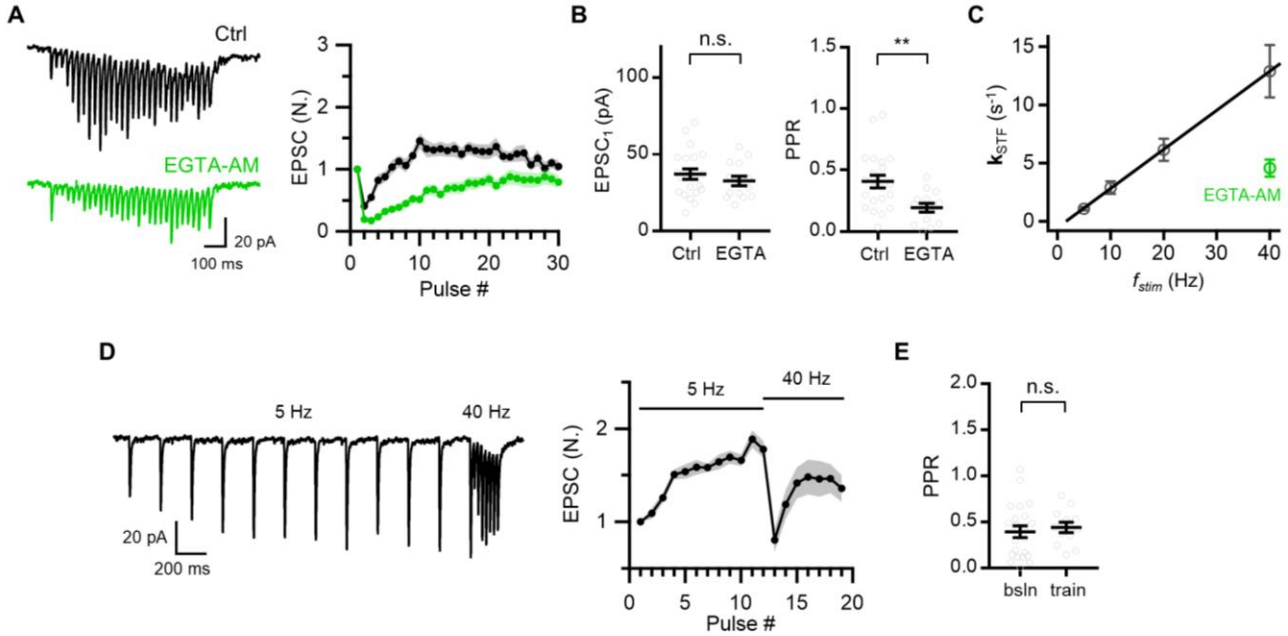

Figure 2. Delayed facilitation results from slow activation of Ca^{2+}-dependent vesicle replenishment at a constantly high vesicular fusion probability

(**A**) Representative traces (*left*) and mean baseline-normalized amplitudes (*right*) of EPSCs evoked by 30-pulse trains at 40 Hz in control (n = 21; *black*) and in the presence of 50 µM EGTA-AM (n = 14; *green*). (**B**) Mean values for the first EPSC amplitude ($EPSC_1$, *left*) and PPR (*right*) from the experiments displayed in (A). *Gray symbols*, individual data. (**C**) Plot of rate constants for short-term facilitation ($\mathbf{k}_{STF}$) as a function of stimulation frequency (f_{stim}), showing a linear relationship. The linear regression line (*black*) is shown fitted to $\mathbf{k}_{STF}$ values, estimated from *Figure 1*. (**D**) Representative EPSC traces (*left*) and average of baseline-normalized EPSCs (*right*) evoked by 12-pulse stimulation at 5 Hz, followed by 40 Hz 7-pulse train (n = 12). Note that slowly developing facilitation was converted to rapid facilitation after strong PPD. (**E**) Mean values for PPR at 40 Hz. The baseline PPR was reproduced from *Figure 1G* and the PPR during 5 Hz train was calculated as (13th EPSC) / (12th EPSC). *Gray symbols*, individual data. All statistical data are represented as mean ± S.E.M.; n.s. = not significant; **, $P < 0.01$; unpaired t-test.

Figure 3

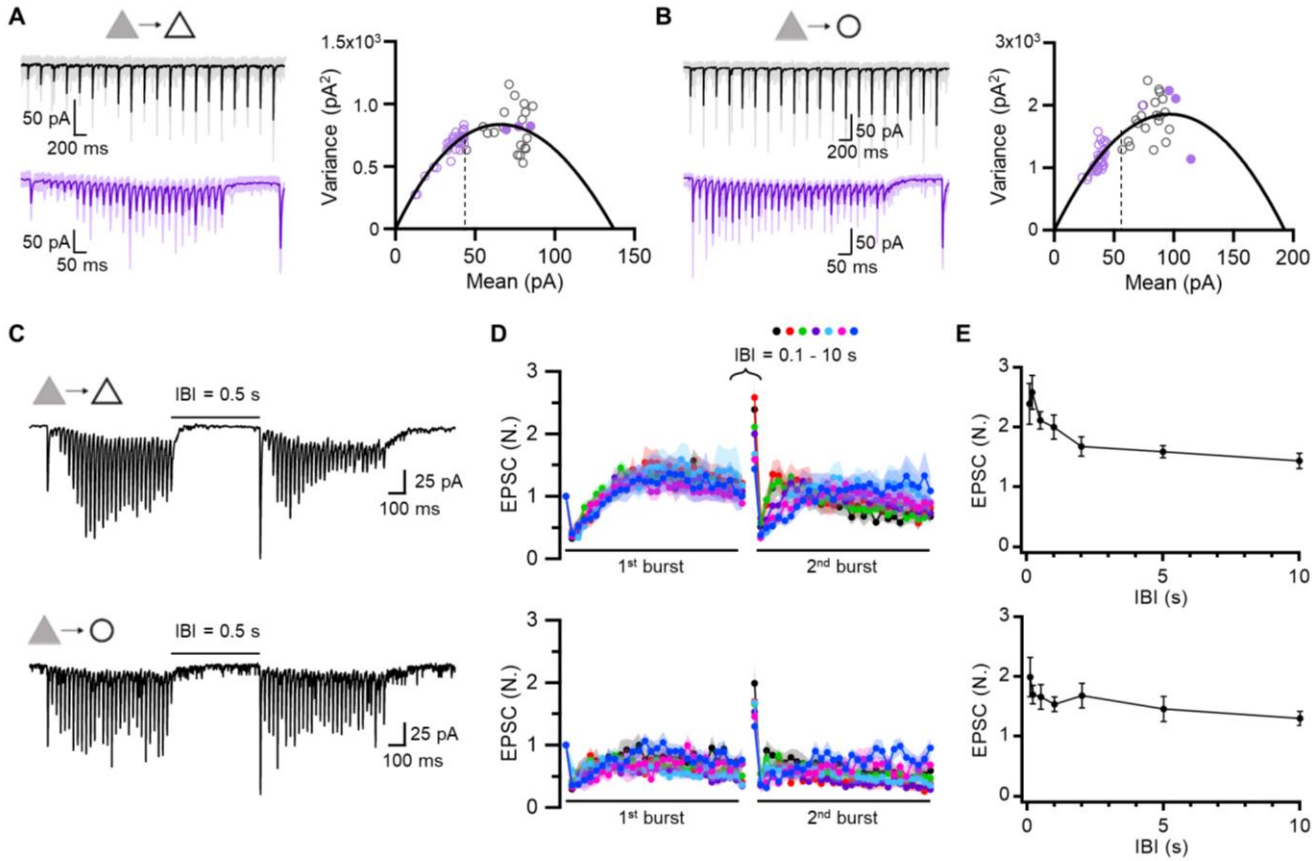

Figure 3. Low baseline occupancy of release sites and its increase during facilitation and post-tetanic augmentation

(**A, B**) *Left*, Representative EPSCs evoked by 5 and 40 Hz train stimulation (*black*, 5 Hz; *purple*, 40 Hz). *Right*, Variance-mean plots of EPSCs amplitude from averaged EPSCs recorded at PC-PC (A; n = 12, 17 for 5 and 40 Hz, respectively) and PC-FSIN (B; n = 8, 10) synapses. The data were fitted using multiple-probability fluctuation analysis (MPFA). Error bars are omitted for clarity. The 1st EPSC of 5 Hz train (*broken line*) was used to estimate the resting level of p_{occ}. *Filled circles* were measured from post-tetanic augmented EPSCs (*A*, n = 12, 12, 9; *B*, n = 7, 7, 7 for 0.1, 0.2, 0.5 s IBIs, respectively). (**C-E**) Post-tetanic augmentation (PTA) experiments at PC-PC (*top*) and PC-FSIN (*bottom*) synapses. (**C**) Representative traces

55 for EPSCs evoked by double 40 Hz train stimulations separated by 0.5 s. (**D**) Mean baseline-
56 normalized amplitudes of EPSCs evoked by double 40 Hz trains at different inter-burst
57 intervals (IBIs, 0.1, 0.2, 0.5, 1, 2, 5, 10 s). *Upper*, PC-PC synapse (n = 12, 12, 21, 11, 11, 16, 11
58 from short to long IBIs, respectively). *Lower*, PC-FSIN synapse (n = 10, 9, 8, 9, 9, 7, 9). (**E**) PTA
59 time course. The baseline-normalized amplitudes of 1st EPSC from the 2nd train were plotted
60 as a function of IBIs.
61

Figure 4

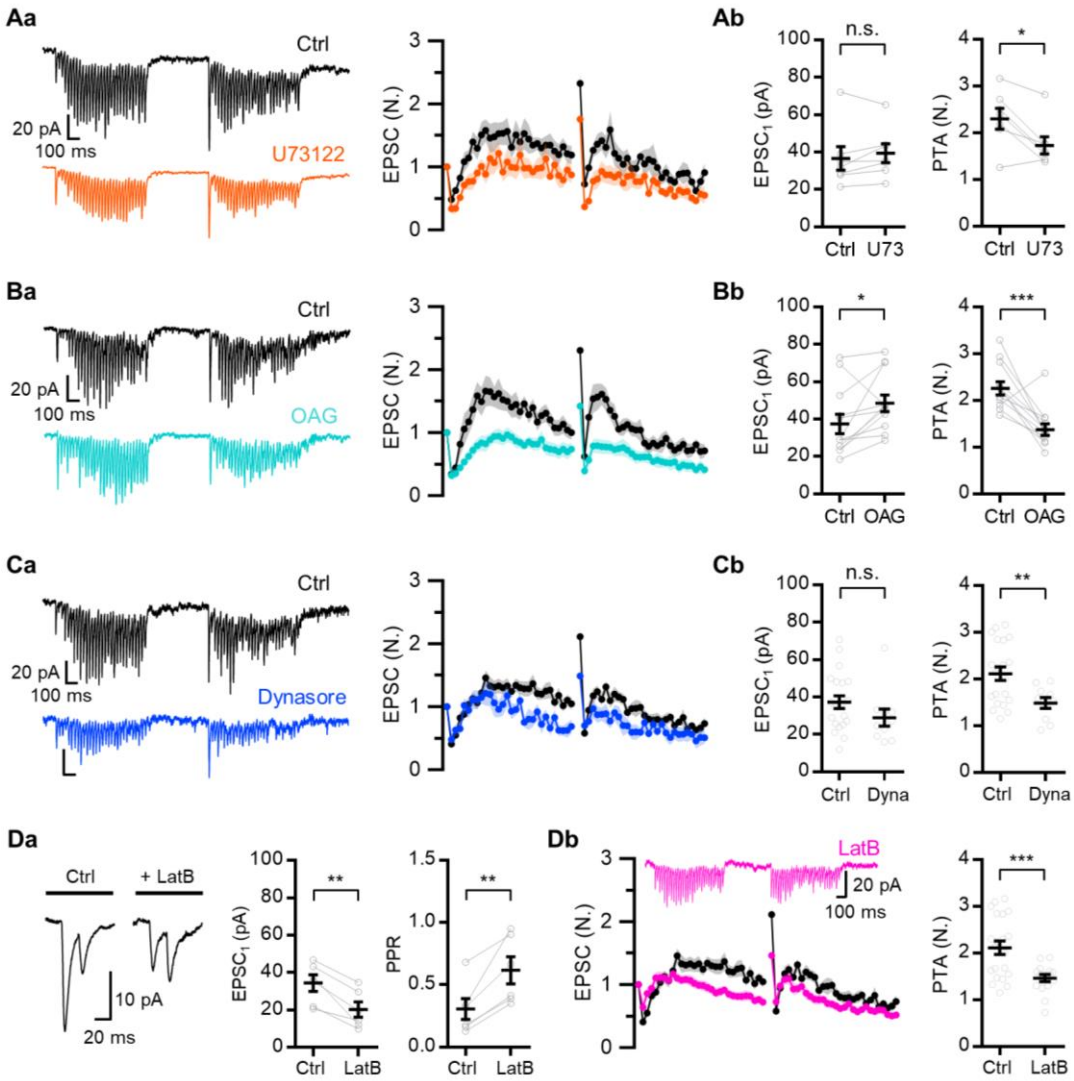

Figure 4. Pharmacological experiments reveal specific molecular mechanisms underlying vesicle loading processes

(**A-C**) (**a**) Representative EPSC traces (*left*) and mean baseline-normalized EPSCs (*right*) evoked by double 40 Hz train stimulations separated by 0.5 s inter-burst interval (IBI) in control and in the presence of 5 µM U73122 (*Aa*, n = 7, *orange*), 20 µM OAG (*Ba*, n = 12, *cyan*) or 100 µM dynasore (*Ca*, n = 10, *blue*). (**b**) Mean values for baseline EPSCs ($EPSC_1$, *left*) and augmentation (*right*) from the experiments shown in corresponding *a* panel. (**Da**)

71 Representative EPSC traces evoked by paired pulses (*left*) and mean values for baseline EPSC
72 amplitude (*middle*) and PPR (*right*) before and after applying 20 μM LatB (n = 6). (**Db**)
73 Representative EPSC traces (*left, upper*) and average of normalized EPSCs (*left, lower*)
74 evoked by double 40 Hz train stimulation separated by 0.5 s in control (n = 21) and in 20 μM
75 LatB conditions (n = 16; *pink*). *Right*, Mean values for augmentation in control and LatB
76 conditions. *Gray symbols*, individual data. All statistical data are represented as mean ±
77 S.E.M., *, $P < 0.05$; **, $P < 0.01$; ***, $P < 0.001$; unpaired or paired t-test; n.s. = not
78 significant.
79

Figure 5

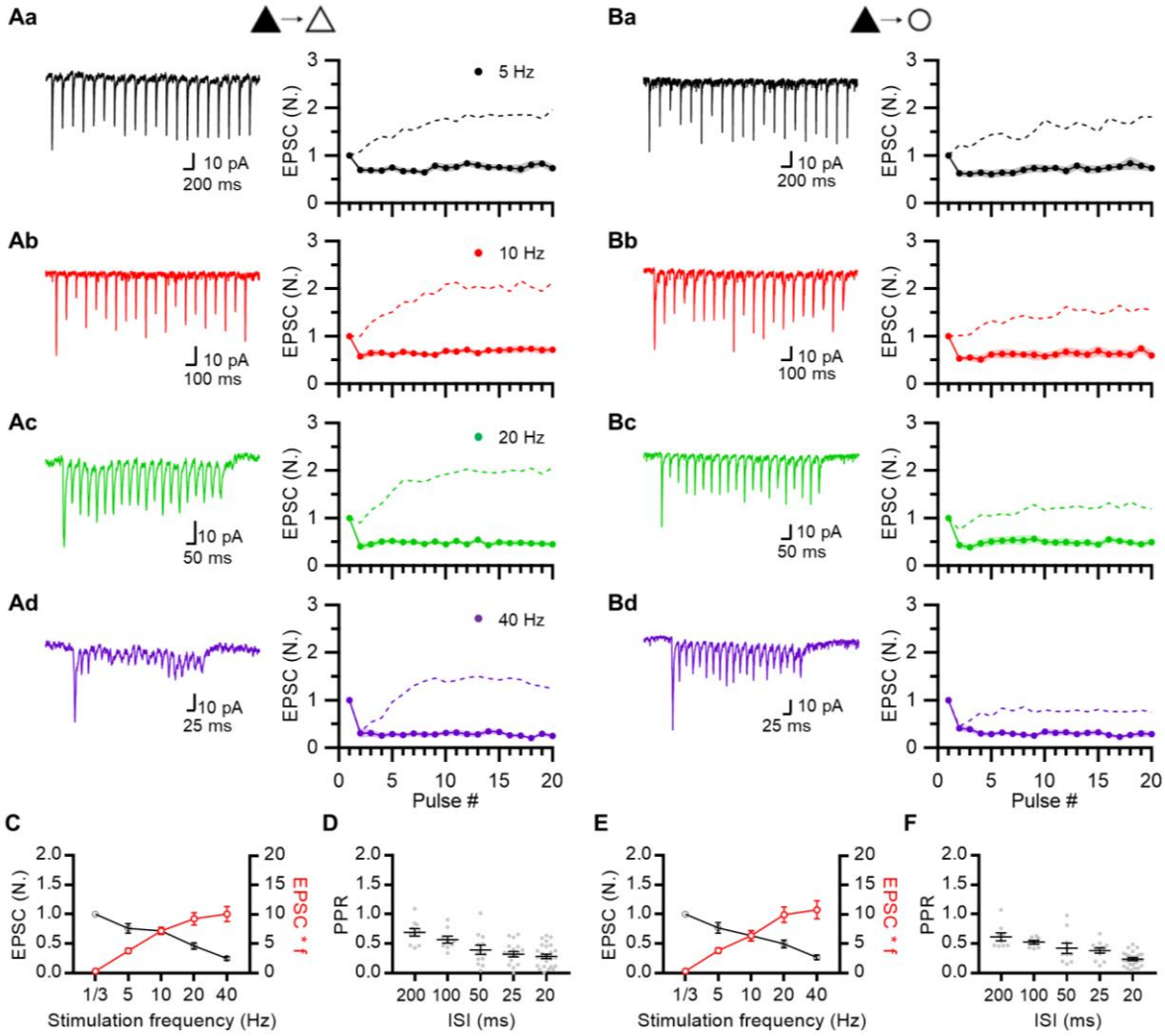

Figure 5. STF at both types of local excitatory synapses is abolished by Syt7 KD

(**A, B**) Representative EPSC traces (*left*) and mean baseline-normalized amplitudes of EPSCs (*right*) evoked by 20-pulse trains at 5 to 40 Hz. STP was measured at PC-PC (*A*; n = 10, 9, 12, 9) and PC-FSIN (*B*; n = 9, 8, 10, 9) synapses, in which presynaptic Syt7 transcripts were depleted (Syt7 KD). Syt7 KD pyramidal cells are indicated as *black triangles* on the top. For comparison, STP in WT synapses is reproduced from ***Figure 1*** (*dotted lines*). Same frequency color codes were used as in ***Figure 1***. (**C**) Baseline-normalized amplitudes of steady-state

89 EPSC ($EPSC_{ss}$; *black symbols*) and synaptic efficacy ($EPSC_{ss}$ × *f*; *red symbols*) as a function of
90 stimulation frequency (*f*) at PC-PC synapses. $EPSC_{ss}$ was defined as the average of last 5 EPSC
91 amplitudes from 20-pulse trains. (**D**) PPR as a function of inter-spike intervals (n = 10, 9, 12,
92 18, 26). (**E**) $EPSC_{ss}$ and synaptic efficacy at PC-FSIN synapses. (**F**) PPR at PC-FSIN synapses (n =
93 9, 8, 10, 12, 24). *Gray symbols*, individual data.
94

95 Figure 6

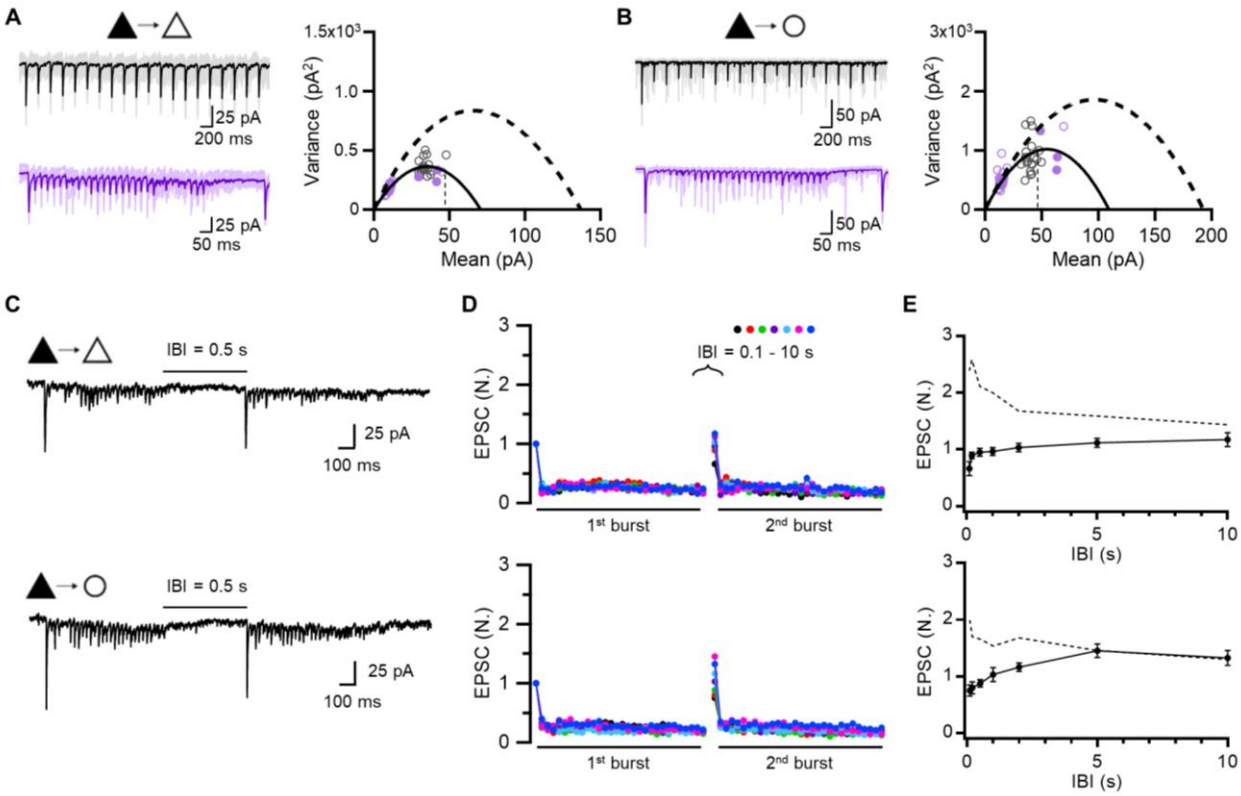

96
97 **Figure 6. Syt7 KD synapses exhibit complementary changes in the number of release sites**
98 **and their vesicle occupancy**

99 (**A, B**) *Left*, Representative traces of EPSCs evoked by 5 and 40 Hz train stimulations (*black*, 5
100 Hz; *purple*, 40 Hz). *Right*, Variance-mean plots of EPSCs amplitude from averaged EPSCs
101 recorded at PC-PC (*A*; n = 9, 15, 12, 10, 9) and PC-FSIN (*B*; n = 4, 14, 10, 9, 8) synapses in
102 which presynaptic Syt7 has been knocked down. The data were fitted using MPFA and error

103 bars are omitted for clarity. The mean 1st EPSC amplitude of 5 Hz train (*vertical broken line*)
104 was used for estimation of baseline p_{occ}. Dashed parabolas indicate MPFA fits to variance-
105 mean plot of WT synapses reproduced from ***Figure 3***. (**C-E**) Recovery experiments at PC-PC
106 (*top*) and PC-FSIN (*bottom*) synapses in which presynaptic Syt7 was knocked-down. (**C**)
107 Representative EPSCs evoked by double 40 Hz train stimulations separated by 0.5 s. (**D**)
108 Mean baseline-normalized amplitudes of EPSCs evoked by double 40 Hz trains at PC-PC (n =
109 12, 10, 9, 9, 10, 9, 8) and PC-FSIN (n = 10, 9, 10, 11, 8, 9, 10) synapses at different interburst
110 intervals (IBIs). (**E**) Recovery time course. Baseline-normalized amplitudes of 1st EPSC from
111 the 2nd burst were plotted as a function of various IBIs. *Dotted lines* indicate augmented
112 EPSCs in the WT reproduced from ***Figure 3***.
113

114 Figure 7

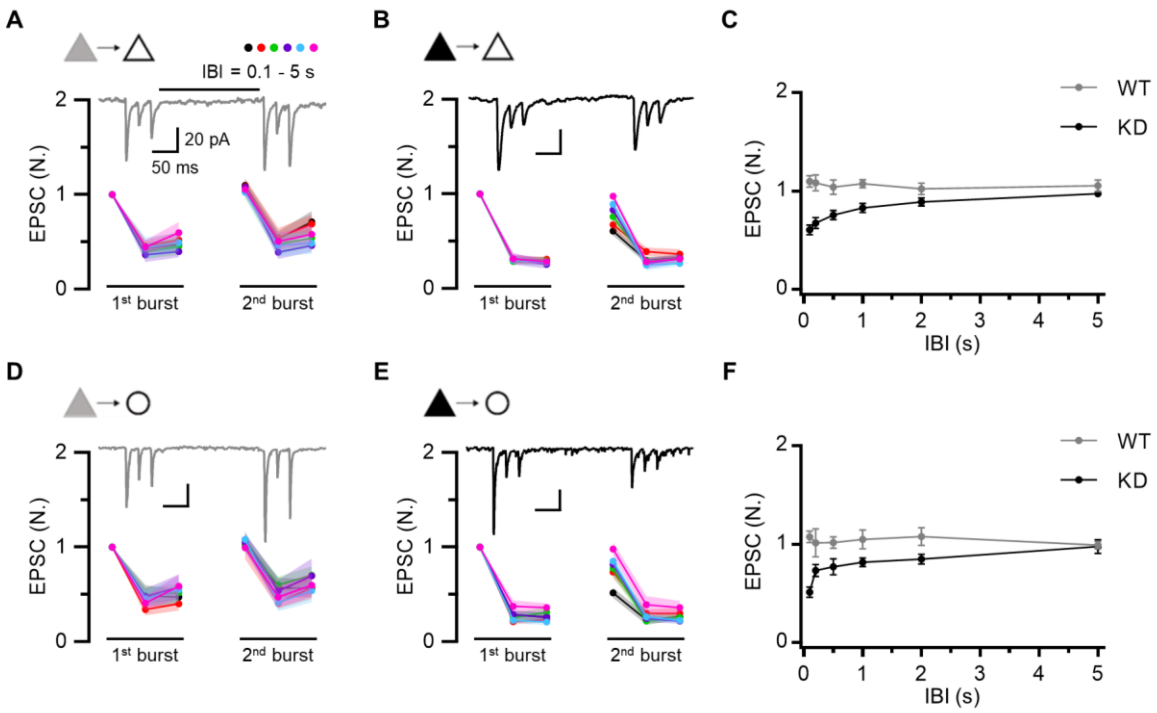

115
116 **Figure 7. Recovery of TS vesicles following depletion is accelerated by Syt7**

117 (**A-C**). Recovery experiments at PC-PC synapses in WT (*A*) and Syt7 KD (*B*). Mean baseline-
118 normalized amplitudes of EPSCs evoked by two consecutive 3-pulse 40 Hz trains in WT (n =

119 16, 13, 11, 11, 11, 9 from short to long IBIs, respectively) and KD (n = 13, 11, 12, 8, 10, 11)
120 synapses at different IBIs (0.1, 0.2, 0.5, 1, 2, 5 s). *Inset*, representative traces of EPSCs
121 evoked by two consecutive 3-pulse 40 Hz train stimulations separated by 0.2 s. (**D-F**).
122 Recovery experiments at PC-FSIN synapses in WT (*D*) and Syt7 KD (*E*). Mean baseline-
123 normalized amplitudes of EPSCs evoked by two consecutive 3-pulse 40 Hz trains in WT (n =
124 9, 11, 11, 9, 10, 13) and KD (n = 9, 12, 9, 7, 10, 9) synapses at different IBIs. *Inset*,
125 representative traces of EPSCs evoked by two consecutive 3-pulse 40 Hz train stimulations
126 separated by 0.2 s. (**C, F**) Recovery time course. Baseline-normalized amplitudes of 1st EPSC
127 from the 2nd burst were plotted as a function of various IBIs.
128

Figure 8

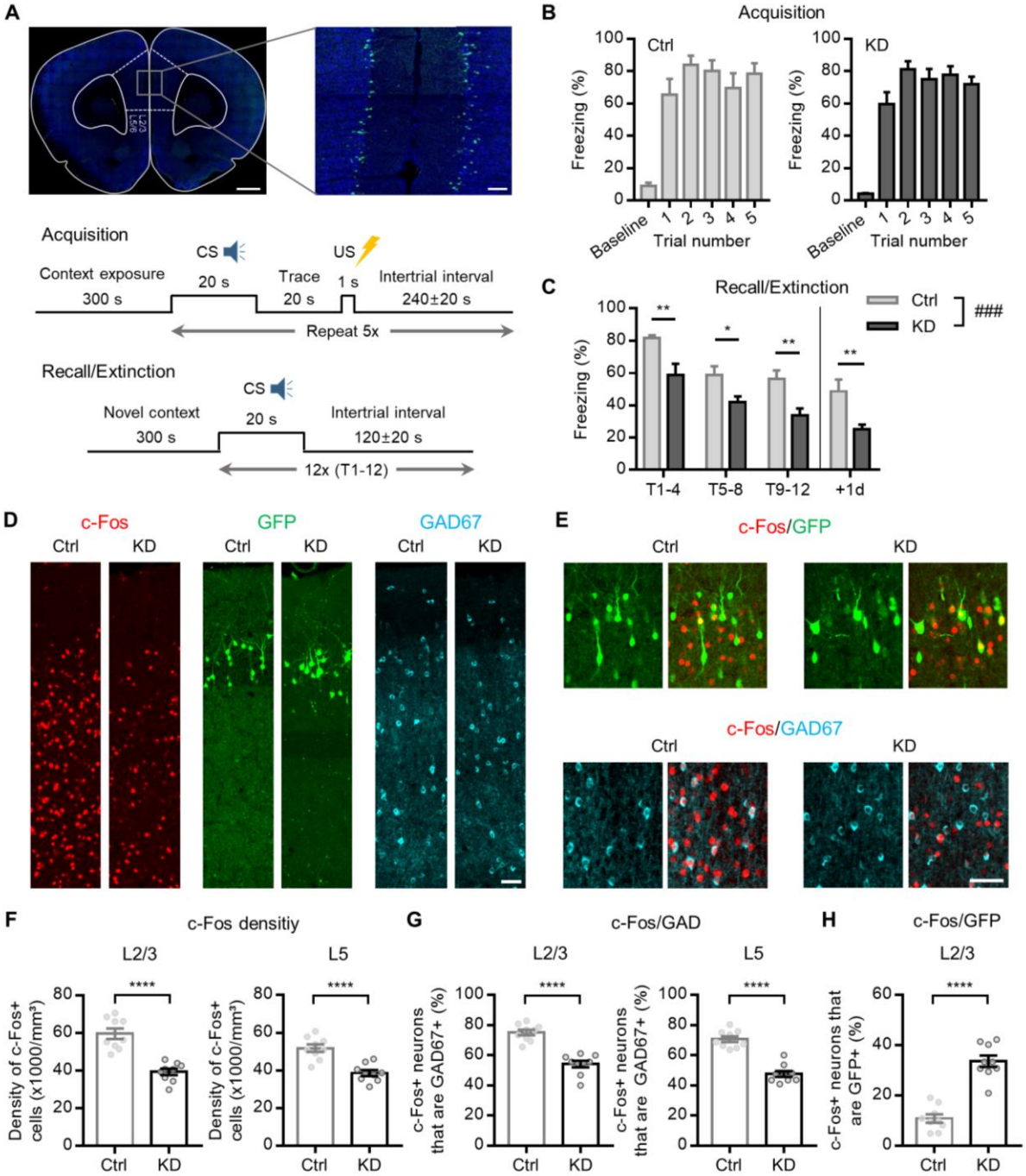

Figure 8. Behavioral effects of Syt7 deficiency in L2/3 PCs of the mPFC

(**A**) *Top*, Representative images showing bilateral expression of U6-GFP in L2/3 of PCs after IUE at E17.5. Scale bar: 1 mm, 100 µm. *Bottom*, Schematic of trace fear conditioning and

134 extinction (tone test) protocol. (**B**) Freezing behavior of control (expressing scrambled
135 shRNA, *Scr*) and Syt7 KD rats during acquisition of tFC. (**C**) Freezing ratio during tone tests on
136 following days. Data are shown as average freezing during T1–T4, T5–T8, or T9–T12 (T,
137 trials). The freezing on T1-T4 was significantly lower in KD rats suggesting that formation of
138 trace memory was impaired in Syt7 KD rats (n = 10, 11 for Ctrl and KD, respectively; P =
139 0.0007, F(1, 19) = 16.43, two-way repeated measures ANOVA; P = 0.0064, 0.0211, 0.0064,
140 0.0064; Holm-Sidak test). (**D**) Representative images of c-Fos immunoreactivity in the
141 prelimbic cortex of control or Syt7 KD rats 90 min after tFC acquisition. c-Fos (*left*, *red*, Cy5)
142 and GAD67 (*right*, *cyan*, Cy3) were immunostained in the same brain slice expressing U6-
143 GFP (*middle*; *green*). Scale bar, 50 µm. (**E**) Exemplar images of c-Fos positive neurons
144 expressing GFP (*top*) or GAD67 (*bottom*) in control (*left*) or Syt7 KD rats (*right*). Scale bar, 50
145 µm. (**F-H**) Effects of Syt7 KD on c-Fos density (*F*) and percentage of c-Fos positive neurons
146 co-labeled with GAD67 (*G*) or GFP (*H*) in L2/3 or L5 of prelimbic cortex (n = 9, 9 for Ctrl and
147 KD, respectively). *Open symbols*, individual data. All statistical data are represented as mean
148 ± S.E.M.; ****, P **<** 0.0001; unpaired t-test.

149

Figure 9

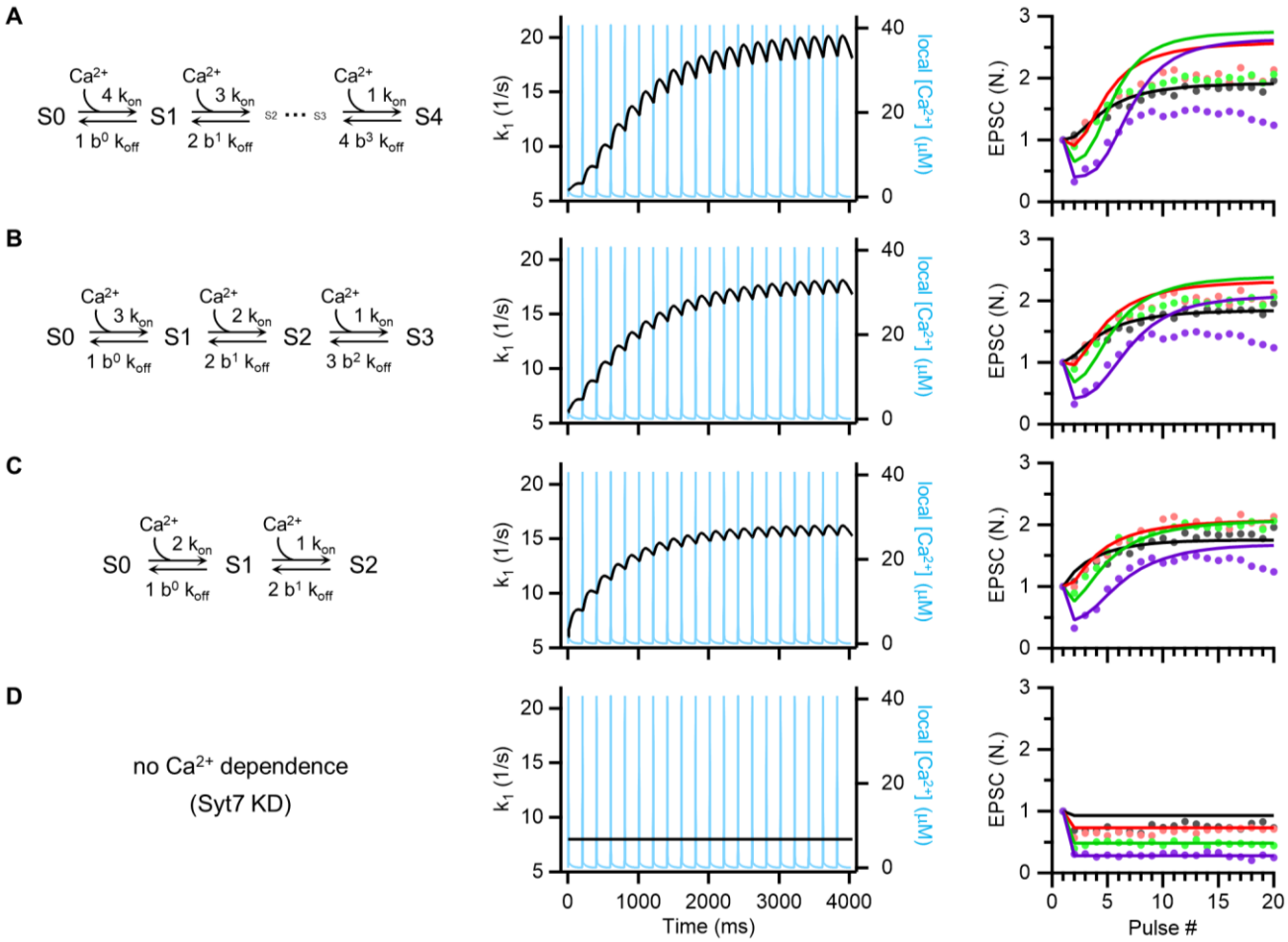

Figure 9. STP model in light of known Ca^{2+} binding kinetics of Syt7

(**A-D**) *Left*, Schematic of allosteric calcium binding to Syt7. The number of Ca^{2+} bound to Syt7 was denoted as # in 'S#' in the reaction scheme. k_{on} = 7/μM/s, k_{off} = 10/s. *Middle*, Simulated changes of k_1 (*black*) in response to 5 Hz train of Ca^{2+} transients (*light blue traces*). The priming step of the simple refilling model was assumed to be catalyzed by full Ca^{2+}-bound form of Syt7. Accordingly, Ca^{2+}-dependent increase in k_1 was calculated as $K_{1,max}$ multiplied by a fraction of full Ca^{2+}-bound form of Syt7. We assumed that local $[Ca^{2+}]_i(t)$ follows a Gaussian function: $(1/\sigma\sqrt{2\pi})\exp[-(t-t_p)^2/2\sigma^2]$, in which t_p = 0.25 ms and σ = 0.085 ms. *Right*, Fits of the Syt7 model to the STP data. To fit this model to the STP data, $K_{1,max}$ was set to

161 300/s (*A*), 220/s (*B*), and 180/s (*C*). Cooperativity factor (*b*) was set to 0.35 (*A*), 0.2 (*B*), and
162 0.05 (*C*). k_1 is set to be constant for Syt7 KD (*D*). Same frequency color codes were used as in
163 ***Figure 1***.

Supplementary Figures

Progressive overfilling of readily releasable pool underlies short-term facilitation at recurrent excitatory synapses in layer 2/3 of the rat prefrontal cortex

Jiwoo Shin[1,2,3], Seung Yeon Lee[2], Yujin Kim[1,2,3*], Suk-Ho Lee[1,2,3*]

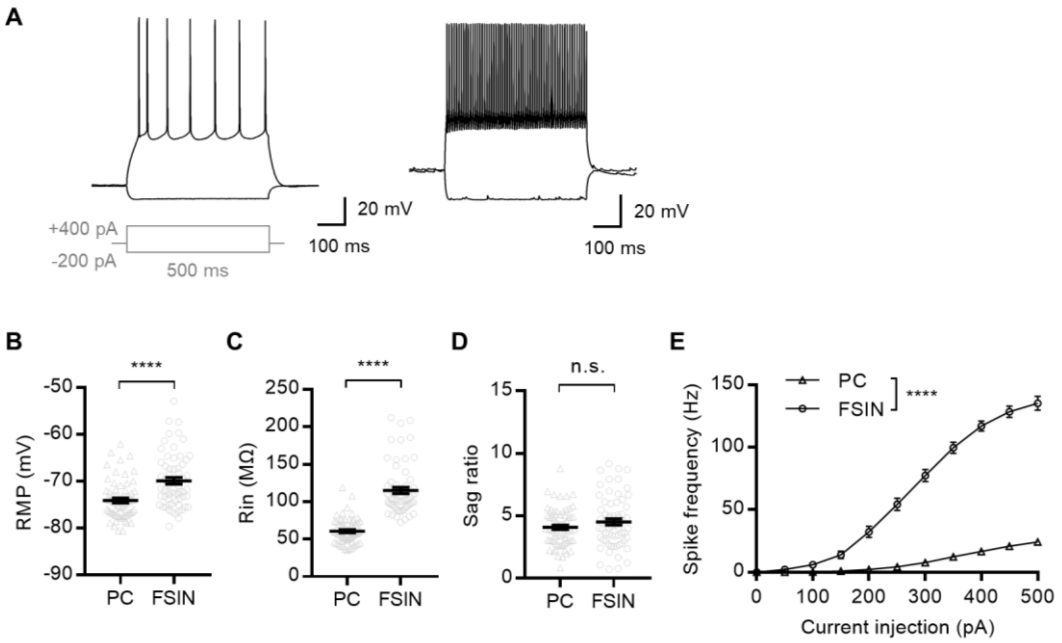

10 **Figure 1—figure supplement 1. Intrinsic membrane properties of mPFC neurons.**

11 (**A**) Neuronal subtypes in mPFC layer 2/3. Cells were characterized based on their
12 electrophysiological properties (n = 66, 64 for PC and FSIN, respectively). Representative
13 voltage responses to current injection (-200 or +400 pA) of pyramidal cells (*left*) and fast-
14 spiking interneurons (*right*). (**B-D**) Mean resting membrane potential (*B*), input resistance
15 (*C*), and Sag ratio (*D*) measured in layer 2/3 PCs and FSINs. *Gray symbols*, individual data. (**E**)
16 Current-spike relationship in each cell type. All statistical data are represented as mean ±
17 S.E.M.; n.s. = not significant; ****, P **<** 0.0001; unpaired t-test or two-way ANOVA.

18

19

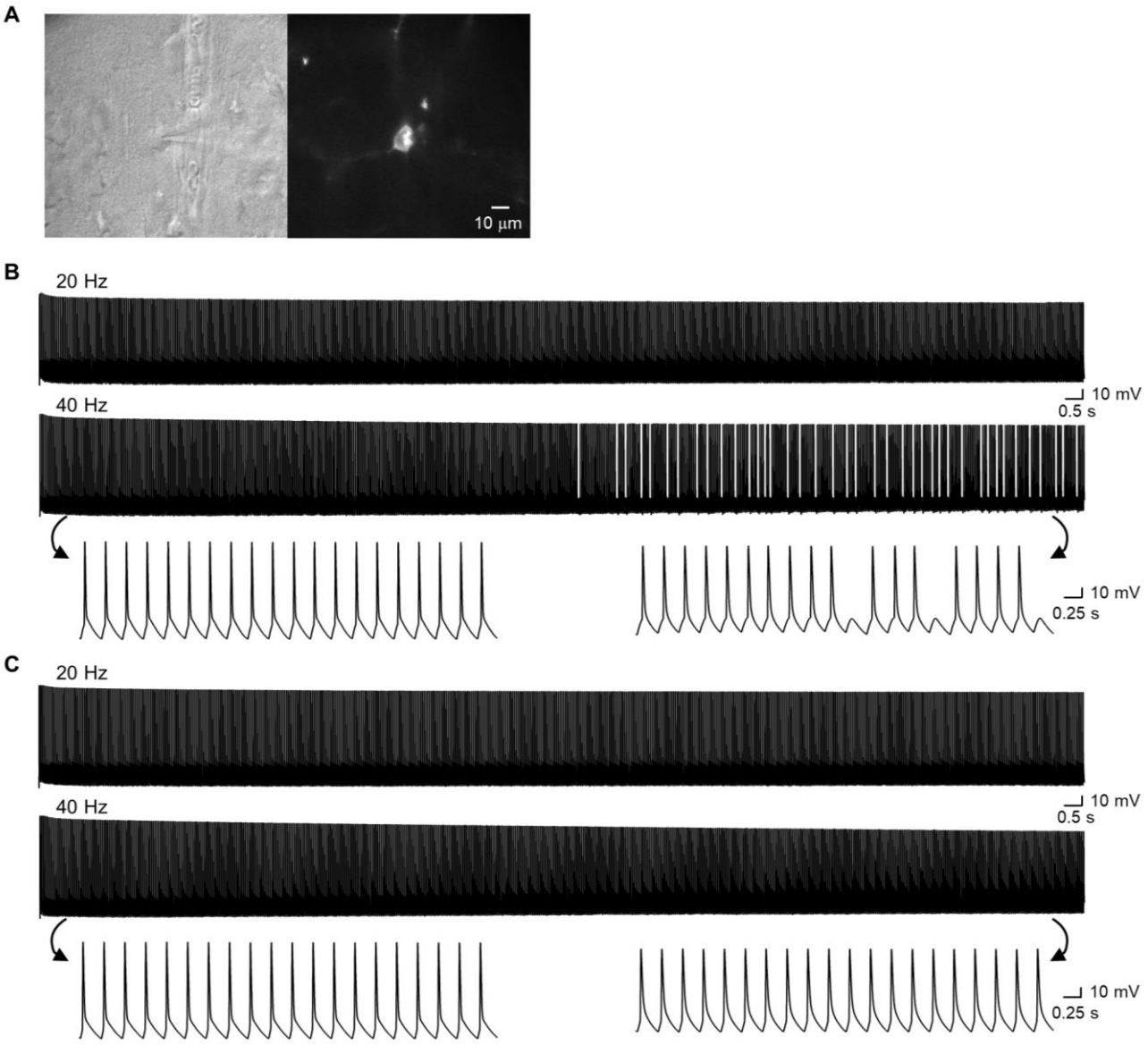

Figure 1—figure supplement 2. Test for consistency of light stimulation in oChIEF-expressing L2/3 pyramidal cells.

(**A**) Representative images of an oChIEF-expressing neuron. Whole-cell recordings were performed from the fluorescently labeled neurons in layer 2/3 of the prelimbic cortex. *Left*, IR-DIC image (60×) of the pyramidal cell under whole-cell patch clamp. *Right*, fluorescence image of td-Tomato in the same cell excited at 530 nm wavelength. (**B**) Current-clamp recordings of action potentials evoked by 600 light pulse trains from an oChIEF-expressing

L2/3 cell. For somatic stimulation, we used the typical light stimulation conditions used in STP experiments (5 ms in duration and 4 µm in radius; see *Methods*). Uniform action potentials were produced with high fidelity, albeit not without compromise towards the end of the train in the case of 40 Hz stimulation. Note that these results are similar to previously reported values from neocortical neurons (Lin et al., 2009; Yoon et al., 2020). (**C**) Same experiments as (*B*) but in Syt7 KD pyramidal cells that express oChIEF in L2/3 of the mPFC.

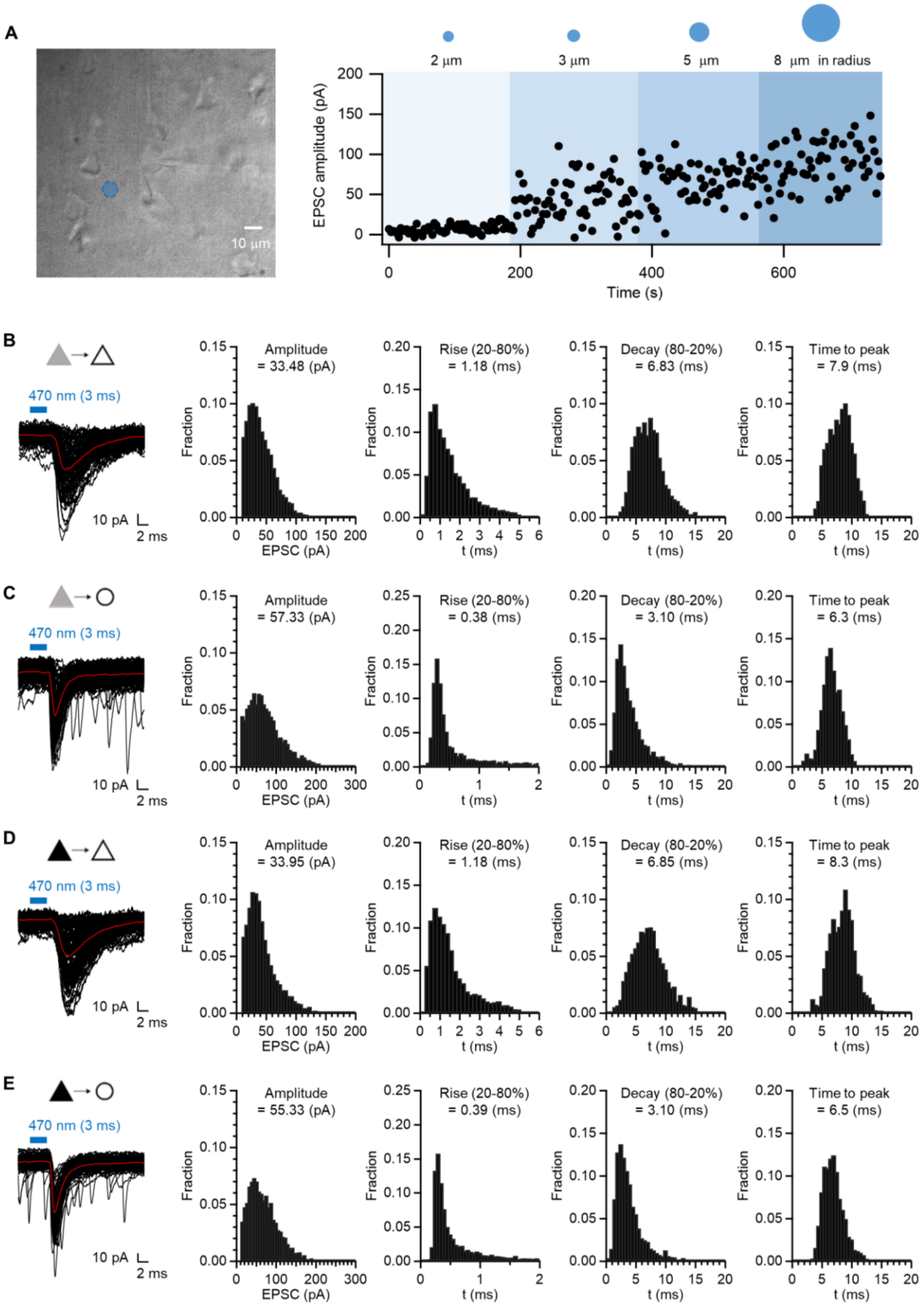
A
10 µm
2 µm
3 µm
5 µm
8 µm in radius
EPSC amplitude (pA)
Time (s)
B
470 nm (3 ms)
10 pA
2 ms
Amplitude = 33.48 (pA)
Rise (20-80%) = 1.18 (ms)
Decay (80-20%) = 6.83 (ms)
Time to peak = 7.9 (ms)
C
470 nm (3 ms)
Amplitude = 57.33 (pA)
Rise (20-80%) = 0.38 (ms)
Decay (80-20%) = 3.10 (ms)
Time to peak = 6.3 (ms)
D
470 nm (3 ms)
Amplitude = 33.95 (pA)
Rise (20-80%) = 1.18 (ms)
Decay (80-20%) = 6.85 (ms)
Time to peak = 8.3 (ms)
E
470 nm (3 ms)
Amplitude = 55.33 (pA)
Rise (20-80%) = 0.39 (ms)
Decay (80-20%) = 3.10 (ms)
Time to peak = 6.5 (ms)
Fraction
EPSC (pA)
t (ms)

36 **Figure 1—figure supplement 3. Properties of EPSCs evoked by minimal stimulation.**

37 (**A**) Optical minimal stimulation. A collimated DMD-coupled LED was used to confine the
38 area of excitation to a small region near the soma. To stimulate a minimal number of
39 excitatory axon fibers, the radius of illumination area was increased from 2 µm by 50% at
40 each step, and selected the smallest illumination area that elicits EPSCs (Yoon et al., 2020)
41 before starting each recording session. The illumination area was in the range of 3 to 8 µm
42 in radius, when measured at the focal plane (typically 3–4 µm) of a 60× water immersion
43 objective (*blue circle* in the photograph). (**B-E**) Properties of minimally stimulated baseline
44 EPSCs (failure-excluded). Medians of frequency distributions are presented. Decay times
45 below 1 ms were excluded from analysis. From left to right, representative traces (100
46 pulses), EPSC amplitude, rise time (20-80%), decay time (80-20%), and time to peak (from
47 stimulus onset) from WT PC-PC (*B*, n = 81), WT PC-FSIN (*C*, n = 77), Syt7 KD PC-PC (*D*, n = 72),
48 and Syt7 KD PC-FSIN (*E*, n = 78) synapses.
49
50

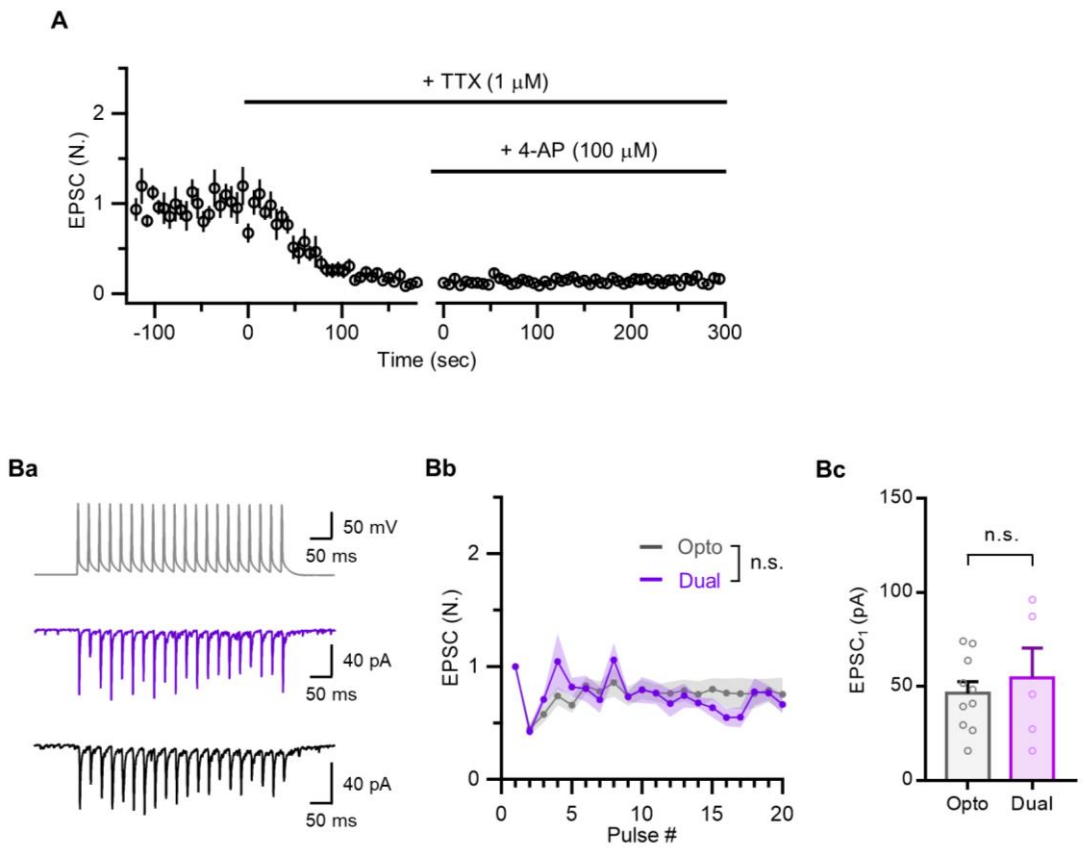

51 **Figure 1—figure supplement 4. Validation of STP of optically evoked EPSCs**

52 (**A**) The high p_v at PC-PC synapses may result from direct photo-stimulation of axon boutons.
53 To test if optically evoked EPSCs depend on APs, the effect of 1 µM tetrodotoxin (TTX) was
54 tested. Applying 1 µM tetrodotoxin (TTX) and additionally 0.1 mM 4-aminopyridine, a D-
55 type K channel blocker abolished optically evoked EPSCs (n = 8). Even when repolarization
56 was hindered by subsequent addition of 100 µM 4-aminopyridine (4-AP), a potassium
57 channel blocker, EPSCs were not rescued. These findings suggest that the light-evoked
58 responses are dependent on APs of presynaptic axon fibers rather than photo-induced
59 depolarization of presynaptic boutons (Little and Carter, 2013). (**B**) Comparison of STP
60 evoked by optical stimulation with that by dual patch techniques. To test validity of STP of
61 photostimulation-evoked EPSCs, we compared STP of unitary EPSCs evoked by dual whole-
62 cell patch at PC-FSIN synapses. Both of EPSC1 and STP at 40 Hz recorded by using paired
63 whole-cell recordings were not significantly different from those evoked by photo-

stimulation, supporting the validity of our optogenetic methods. (**Ba**) Representative EPSC traces evoked by 20-pulse 40 Hz trains stimulation at pyramidal cell to fast spiking interneuron (PC-FSIN) synapses. A train of APs in a presynaptic PC (*top*), evoked EPSCs in a FSIN by dual whole-cell patch clamp (*middle*) or by optical stimulation (*bottom*) under same conditions. (**Bb**) Mean values for baseline-normalized amplitudes of EPSCs evoked by 40 Hz train at PC-FSIN synapses. *Opto*, optical stimulation (n = 10); *Dual*, dual patch techniques (n = 5). STP evoked by the two techniques were not significantly different (two-way repeated measures ANOVA, $F(1, 13) < 0.01$, $P = 0.955$). (**Bc**) Mean values for the first EPSC in different stimulation methods ($P = 0.5724$, unpaired t-test). *Open circles*, individual data. All statistical data are represented as mean ± S.E.M.

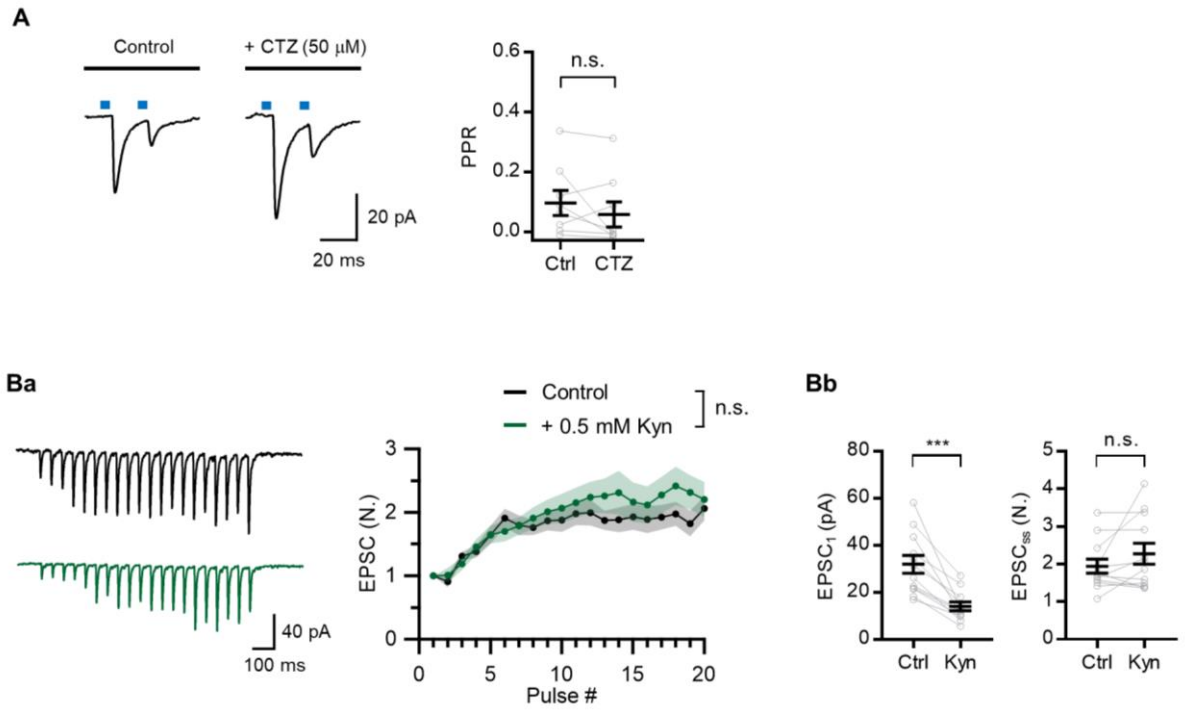

Figure 1—figure supplement 5. Test for AMPAR desensitization and saturation

(**A**) Representative traces of EPSCs evoked by paired-pulse photostmulation at 20 ms ISI (*left*) and mean values for paired pulse ratio (PPR, *right*) before and after applying 50 µM cyclothiazide (CTZ, n = 8), an AMPA receptor (AMPAR) desensitization inhibitor. CTZ induced no significant change in PPR arguing against the possibility that strong PPD is caused by AMPAR desensitization. *Gray symbols*, individual data. (**B**) It has been shown that multi-vesicular release occurs at recurrent excitatory synapses in neocortical L2/3 (Holler et al., 2021). Whereas a single vesicle release is insufficient to saturate postsynaptic AMPARs, an increase in the number of vesicular release during facilitation may saturate AMPAR resulting in underestimation of facilitation. To test this possibility, facilitation at 20 Hz was measured in the presence of 0.5 mM kynurenic acid (Kyn), a fast competitive antagonist (Diamond and Jahr, 1997; Wadiche and Jahr, 2001). Fast blockade of AMPA receptors did not have significant effects on short-term facilitation at excitatory synapses in the mPFC L2/3, suggesting that AMPAR saturation may not be significant during facilitation. (**Ba**) Representative EPSC traces (*left*) and average of baseline-normalized EPSCs (*right*) evoked

91 by 40 Hz 20-pulse trains in control and in the presence of 0.5 mM kynurenic acid (Kyn).
92 Although facilitation was slightly increased by Kyn, it was not statistically significant (n = 12;
93 two-way repeated measures ANOVA, F (1, 22) = 0.575, P = 0.456). The slightly higher
94 facilitation may result from reduced blocking efficiency of Kyn upon increased glutamate
95 concentration in the synaptic cleft (Tong and Jahr, 1994; Meyer et al., 2001). (**Bb**) Mean
96 values for the baseline EPSC (*left*) and the steady-state EPSC (*right*) before and after
97 applying 0.5 mM kynurenate as shown in *Ba*. The baseline EPSC was reduced by Kyn to
98 43.5% of control. *Gray symbols*, individual data. All statistical data are represented as mean
99 ± S.E.M.; n.s. = not significant; ***, P **<** 0.001; paired t-test.

100

101

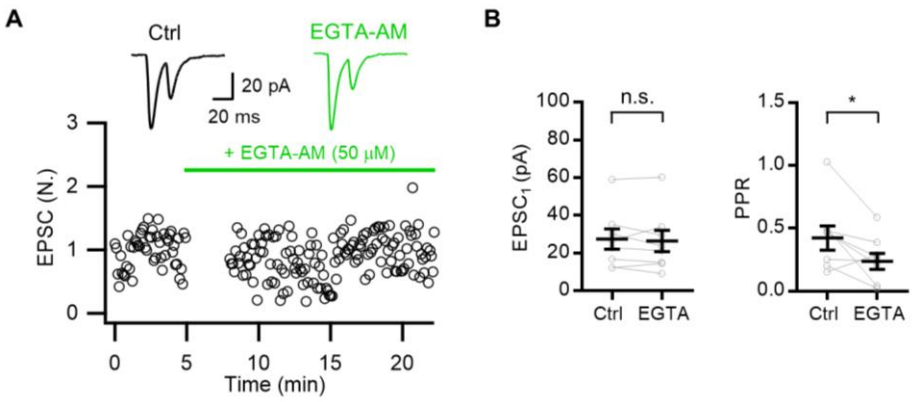

102 **Figure 2—figure supplement 1. Effects of EGTA-AM on synaptic transmission**

103 (**A**) Representative traces (*top*) and time courses of normalized amplitudes of the first EPSCs
104 (*bottom*) during paired-pulse photostimulation at 20 ms ISI in control and in the presence of
105 50 μM EGTA-AM (n = 8). The green horizontal bar indicates application of 50 μM EGTA-AM.
106 (**B**) Mean values for the first EPSC (*left*) and PPR (*right*) before and after EGTA-AM
107 application. *Gray symbols*, individual data. All statistical data are represented as mean ±
108 S.E.M.; n.s. = not significant; *, P **<** 0.05; paired t-test.

109

110

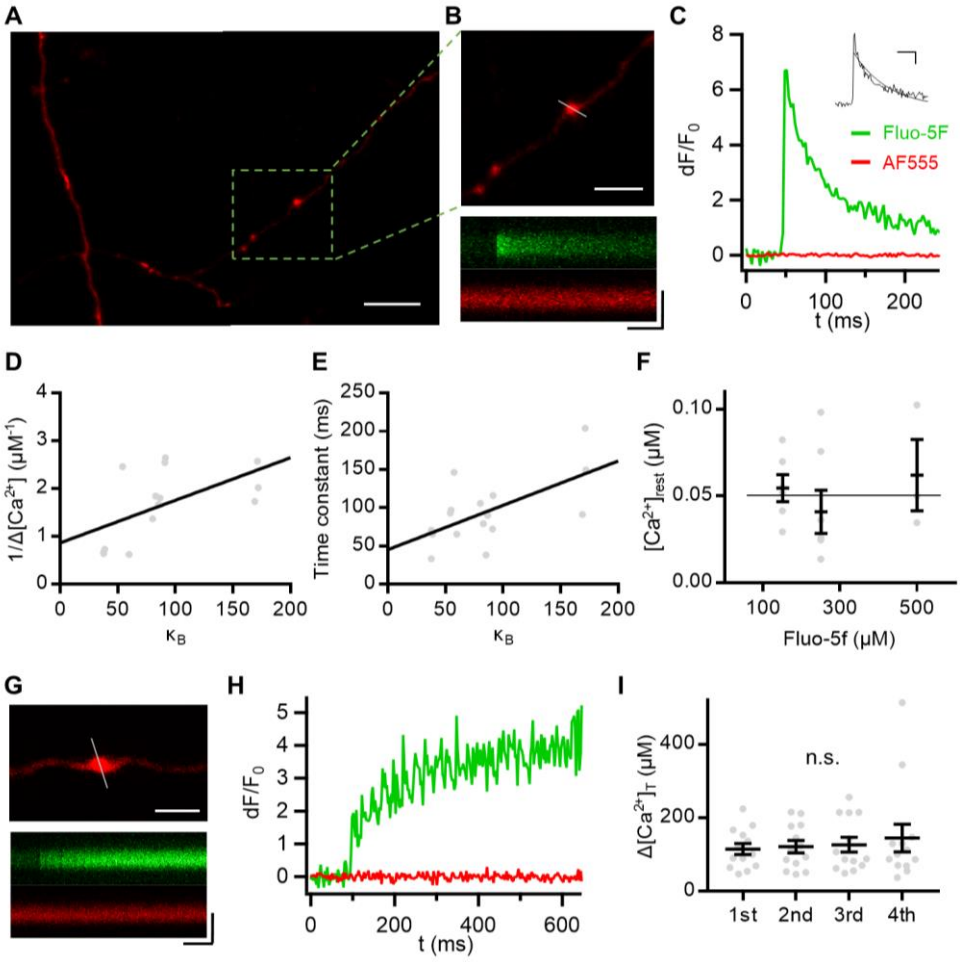

Figure 2—figure supplement 2. Presynaptic calcium kinetics at boutons of layer 2/3 pyramidal cells

(**A-C**) A mixture of Fluo-5F (150, 250 or 500 μM) and Alexa Flour 555 was loaded on their axonal boutons of L2/3-PCs through whole-cell patch techniques for dual excitation ratiometric measurements of the cytosolic [Ca^{2+}] at axonal boutons. (**A**) The long-branched stretch of axon from L2/3 PCs visualized through maximum fluorescence intensity projection using confocal laser scanning of AF555 perfused via a patch clamp pipette. Scale bar, 10 μm. (**B**) *Top*, the selected bouton for recordings, among the three, is displayed with the corresponding scanning line. Scale bar, 5 μm. *Bottom*, Line-scan images for fluorescence of Fluo-5F and AF555. Scale bars, 50 ms and 2 μm. (**C**) Baseline-normalized fluorescence changes evoked by an AP. Fluorescence intensities were spatially averaged over the bouton

122 shown in (*B*), background-subtracted and normalized to the baseline value (dF/F_0). *Inset*,
123 Ca^{2+} transient estimated from dF/F_0. Scale bar, 50 ms and 100 nM. (**D, E**) The kinetic
124 parameters of an AP-CaT were determined from a plot for the inverse of AP-evoked [Ca^{2+}]
125 increment (1/Δ[Ca^{2+}]) *vs*. calcium binding ratio (κ_B; Eq. 4 in *Material and Methods*). (**D**)
126 Reciprocal plot of the AP-induced [Ca^{2+}] changes (1/Δ[Ca^{2+}]) vs. corresponding calcium
127 binding constants (κ_B) according to Eq. 2 (n = 14). A linear fit to the plot gave the amplitude
128 of AP-CaT (A_{Ca} = 1.16 μM) from the y-intercept, representing the amplitude of free [Ca^{2+}]
129 increase in the absence exogenous Ca^{2+} buffer. The calcium binding ratio of endogenous
130 static Ca^{2+} buffers (κ_S) was estimated as 96 from the x-intercept of the linear regression
131 based on Eq. 2 in *Material and Methods*. Linear regression line, P = 0.035. (**E**) Plot of [Ca^{2+}]
132 decay time constant versus κ_B (n = 16). The time constant for [Ca^{2+}] decay from mono-
133 exponential fit was plotted vs. κ_B, and a linear regression based on Eq. 3 yielded the κ_S value
134 of 77 from the x-intercept. The y-intercept was 43 ms, an estimate for a dye-independent
135 value for Ca^{2+} decay time constant (τ_c) (Eq. 3 in *Material and Methods*). Linear regression line,
136 P = 0.011. (**F**) Resting [Ca^{2+}] measured from basal fluorescence ratio using Eq. 1 in *Material*
137 *and Methods* as a function of [Fluo-5F] in patch pipettes. The horizontal line indicates 50 nM.
138 The mean $[Ca^{2+}]_{rest}$ at three different concentrations of Ca^{2+} indicator dye were not different
139 and measured as 50 nM, suggesting that the dye did not influence $[Ca^{2+}]_{rest}$. (**G-I**) Strong PPD
140 and the subsequent STF may be caused by Ca^{2+} channel inactivation and Ca^{2+}-dependent
141 facilitation (CDF) of calcium influx into presynaptic boutons, respectively. To test these
142 possibilities, we measured presynaptic Ca^{2+} increments evoked by each of successive APs
143 applied in a train at 40 Hz. (**G**) Fluorescence signals from a selected bouton with a scanning
144 line. *Scale bars*, 3 μm (*top*), 100 ms and 2 μm (*bottom*). (**H**) Normalized fluorescence (dF/F_0)
145 responses to a train of APs at 40 Hz. (**I**) Total Ca^{2+} increments ($\Delta[Ca^{2+}]_T$; free plus bound form)
146 are plotted against the number of APs in the train (n = 13). $\Delta[Ca^{2+}]_T$ were calculated based on
147 Eq. 2 with κ_S set to 90. No significant change was observed for the estimates of $\Delta[Ca^{2+}]_T$ at
148 each of first 4 APs during 40 Hz train, indicating that contributions of Ca^{2+} channel
149 inactivation and CDF to STP are unlikely. Mean ± S.E.M., One-way ANOVA; n.s. = not
150 significant.

151

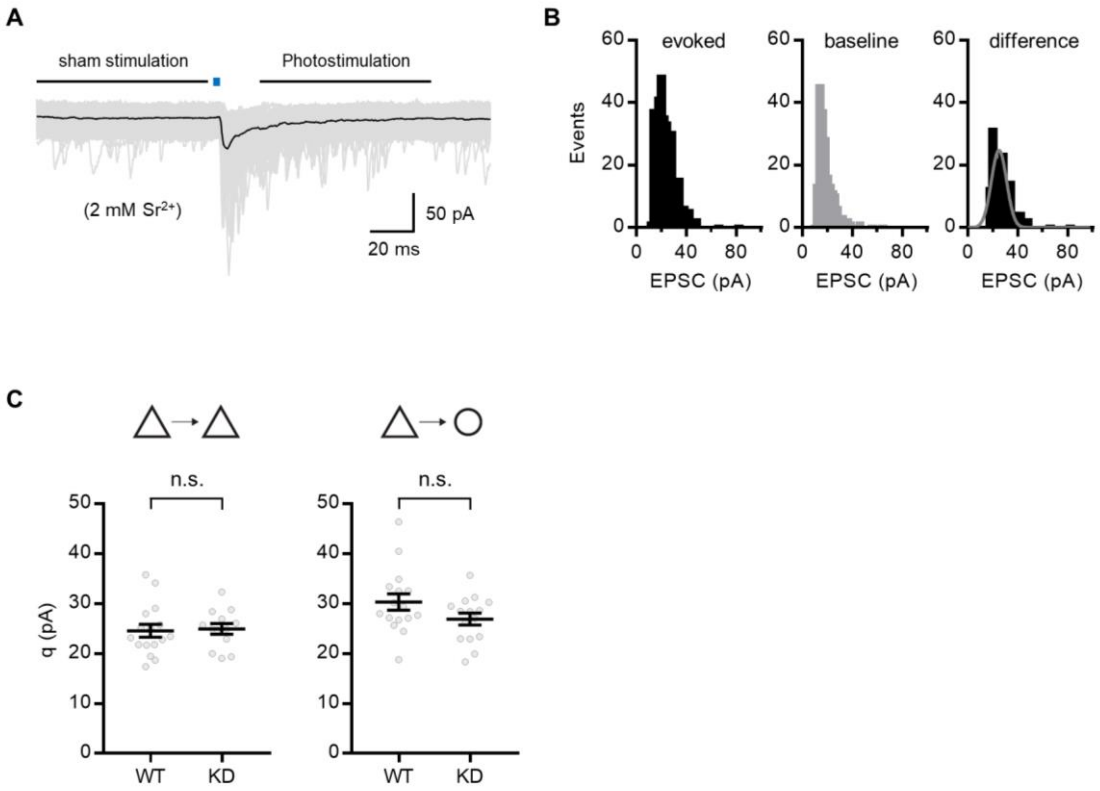

152 **Figure 3—figure supplement 1. Quantal size estimated from Sr^{2+}-induced asynchronous**
153 **release.**

154 (**A**) Representative traces (100 pulses) from PC-PC synapses. Black bars indicate the
155 detection window (100 ms) for release events in sham stimulation (*left bar*) and
156 photostimulation (*right bar*). (**B**) Representative distribution of asynchronous EPSCs at PC-PC
157 synapses. *Left*, after photostimulation. *Middle*, before stimulation. *Right*, difference
158 between left and middle panels. The difference distribution was fitted with a Gaussian
159 function (m = 24.93, σ = 6.09). (**C**) Comparisons of estimates for quantal size (q) between WT
160 and Syt7 KD synapses. From left to right: PC-PC (n = 16, 13 for WT and KD, respectively), PC-
161 FSIN (n = 16, 15). *Gray symbols*, individual data. All data are represented as mean ± S.E.M.,
162 unpaired t-test; n.s. = not significant.
163

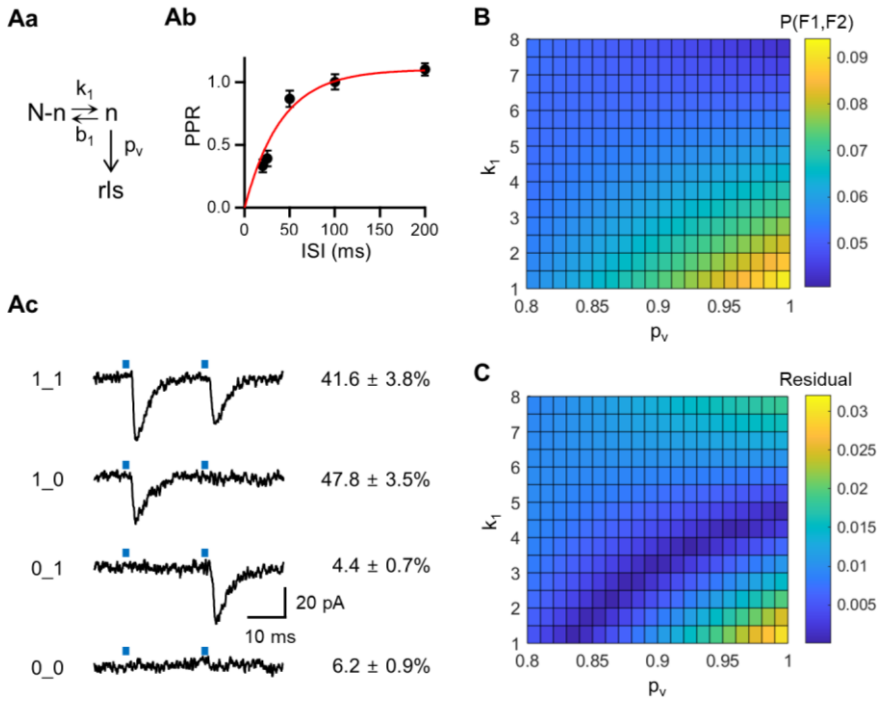

164 **Figure 3—figure supplement 2. Analysis of double failure rate supports high p_v at**
165 **excitatory synapses**

166 (**Aa**) Schematic of simple refilling model. (**Ab**) An exponential fit to the PPR plot as a function
167 of ISIs reproduced from *Figure 1G*. *Fitted function*, PPR = 1.1 [1 − exp(− t/43.5 ms)]. (**Ac**)
168 Representative traces for four combinations of success and failure of 1st and 2nd EPSCs
169 evoked by paired pulses with ISI of 20 ms at PC-PC synapses, showing successes in both
170 pulses (1_1), failures in both pulses (0_0), and mixed responses (1_0; 0_1). On the right side
171 of each trace, corresponding observation probability is shown in percentages (mean ±
172 S.E.M. n = 57). (**B-C**) Plots of the calculated P(F1, F2) values (*B*) and their differences (*C*) from
173 the observed value (6.2%) under the simple refilling model are displayed on the plane of k_1
174 versus p_v.
175
176

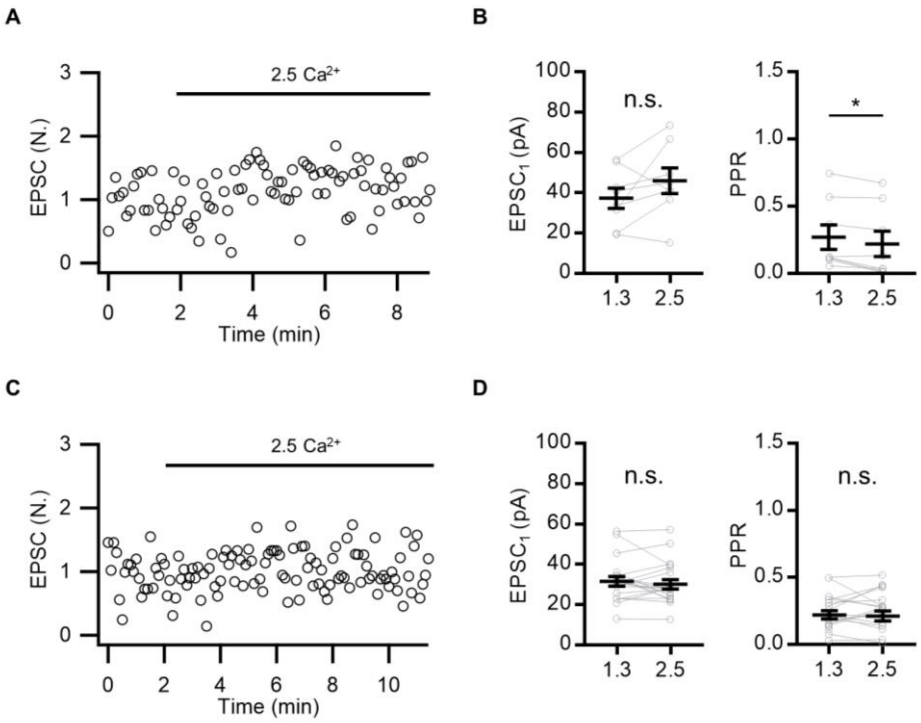

177 **Figure 3—figure supplement 3. Minimal EPSC increase upon elevated $[Ca^{2+}]_o$ indicates**

178 **saturated p_v at baseline**

179 (**A**) Representative time courses of normalized amplitudes of the first EPSCs during paired-
180 pulse photo-stimulation at 20 ms ISI under control conditions (1.3 mM $[Ca^{2+}]_o$) and elevated
181 extracellular $[Ca^{2+}]$ (2.5 mM; n = 8). (**B**) Mean values for the first EPSC (*left*) and PPR (*right*)
182 under the two conditions. (**C-D**) Experiments of A-B were repeated in the slices that were
183 pre-incubated in aCSF containing 50 µM EGTA-AM (n = 20). Note that the modest
184 extracellular $[Ca^{2+}]$-dependence of the first EPSC and PPR observed in A-B was abolished by
185 50 µM EGTA-AM pre-incubation. *Gray symbols*, individual data. All statistical data are
186 represented as mean ± S.E.M.; n.s. = not significant; *, P **<** 0.05; paired t-test.

187

188

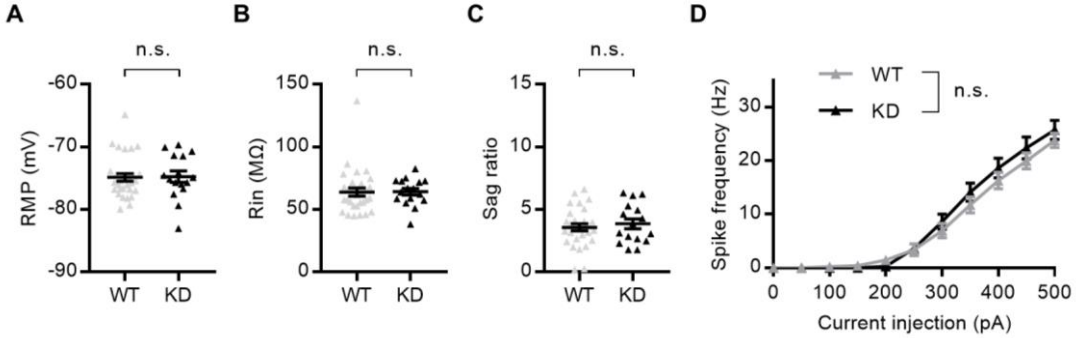

Figure 5—figure supplement 1. Little effects of Syt7 KD on intrinsic properties of neurons

Whole-cell recordings were performed from the fluorescently labeled pyramidal neurons in the prelimbic L2/3 of WT (n = 30) or Syt7 KD (n = 16) rats. (**A**) Resting membrane potential. (**B**) Input resistance. (**C**) Sag ratio. *Filled triangles*, individual data. (**D**) Current-spike frequency relationship in WT and KD cells. All statistical data are represented as mean ± S.E.M., unpaired t-test or two-way ANOVA; n.s. = not significant.

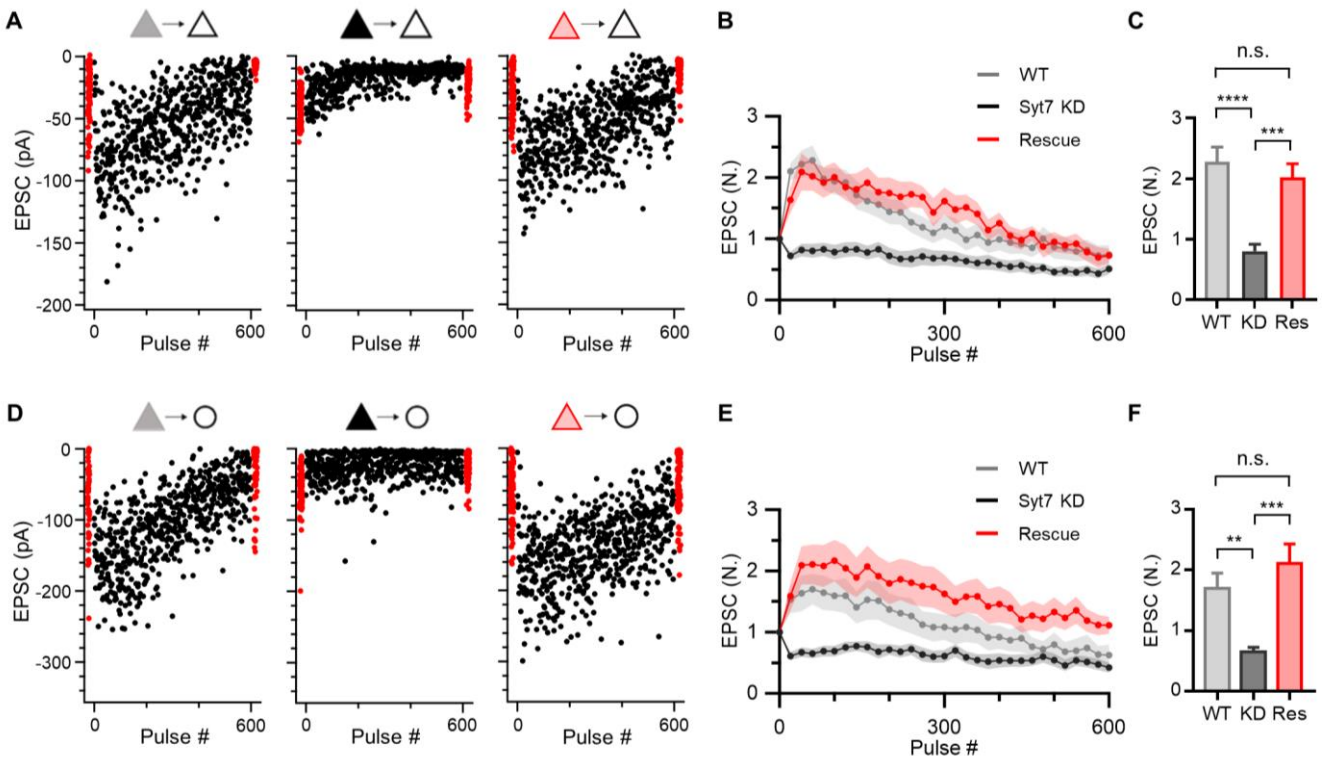

197 **Figure 5—figure supplement 2. Presynaptic expression of Syt7 rescues facilitation at L2/3**
198 **excitatory synapses**

199 (**A, D**) Representative amplitudes of EPSC trains evoked by 600-pulse 10 Hz trains (flanked
200 by 2 baseline periods comprised of 40 pulses each) at PC-PC (*A*) and PC-FSIN (*D*) synapses, in
201 which presynaptic WT (*left, gray triangles*) pyramidal cells and those transfected with
202 plasmid encoding shRNA against Syt7 (sh-Syt7, KD, *middle, black triangles*) or sh-Syt7 plus
203 Syt7 insensitive to shRNA (rescue, *right, red triangles*). (**B, E**) STP of EPSCs evoked by 600-
204 pulse trains at 10 Hz at L2/3 PC-PC (*B*; n = 9, 10, 7; WT, Syt7 KD, Rescue, respectively) and
205 PC-FSIN (*E*; n = 12, 10, 8) synapses. Each data point represents an average from a moving
206 window of 20 pulses, normalized to the baseline EPSC. (**C, F**) Mean values of 41-60th pulses
207 from *B* and *E*. Mean ± S.E.M.; n.s. = not significant; **, P < 0.01; ***, P < 0.001; ****, P <
208 0.0001; one-way ANOVA with Tukey's post-hoc test.

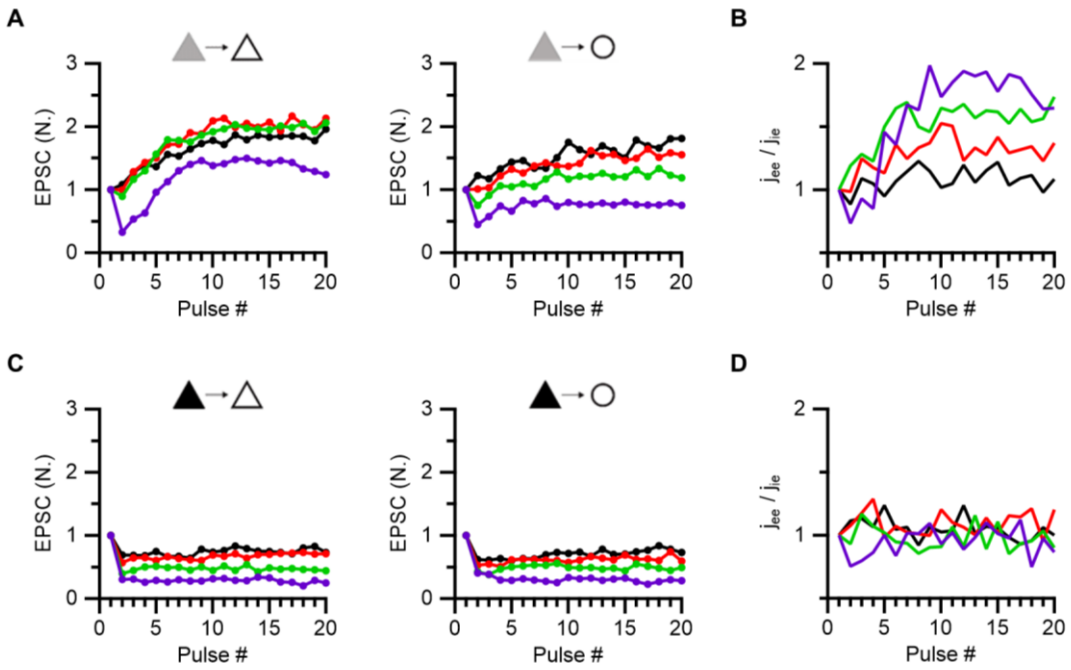

209 **Figure 8—figure supplement 1. Activity-dependent increase in the synaptic weight ratio at**

210 **PC-PC to at PC-FSIN connections (J_{ee}/J_{ie}) is abolished by Syt7 KD**

211 (**A, C**) Average amplitudes of baseline-normalized EPSCs during 20-pulse trains at
212 frequencies from 5 to 40 Hz at PC-PC (*left*) and PC-FSIN (*right*) synapses in WT (*A*) and Syt7
213 KD (*C*). Data are reproduced from ***Figure 1*** (*A*) and ***Figure 5*** (*C*). (**B, D**) Relative synaptic
214 weights of excitatory input to PCs over that onto FSINs (*Jee/Jie*) in WT (*B*) and Syt7 KD (*D*).
215 Note that excitatory influence (*Jee/Jie*) to the recurrent network increases as the firing
216 number and frequency increase in WT but not in Syt7 KD.
217
218

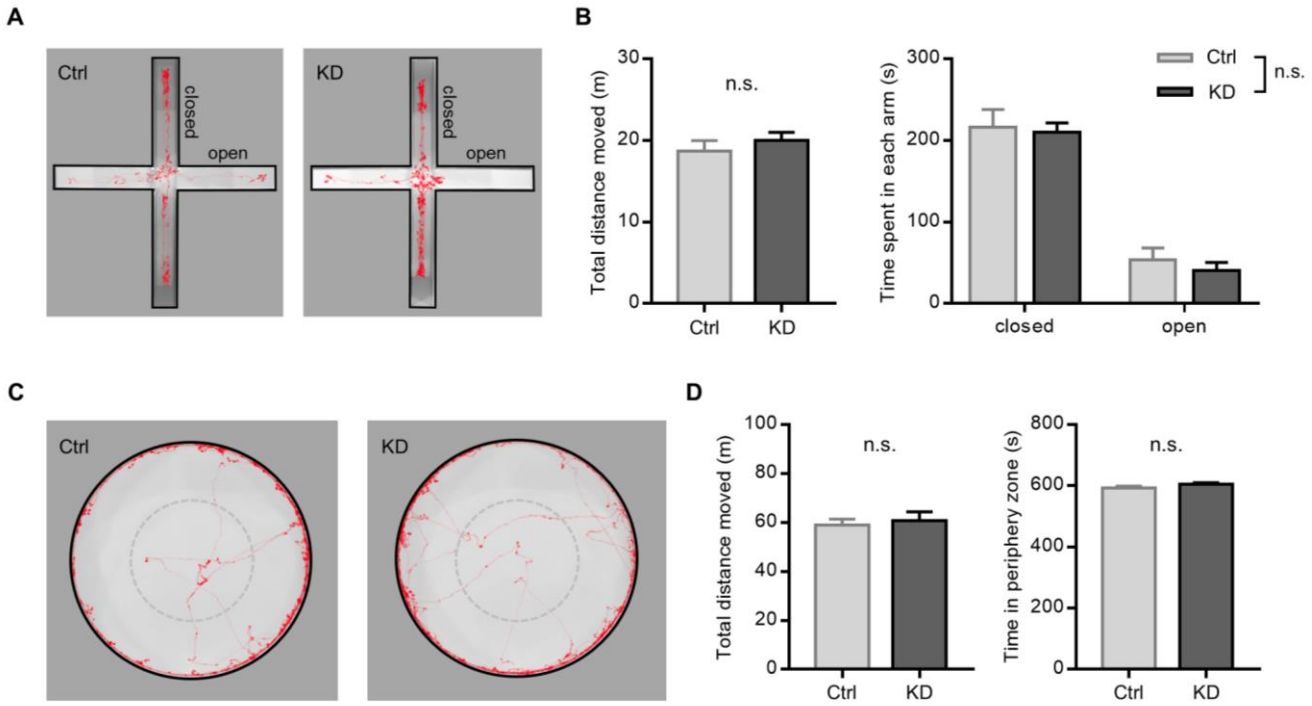

Figure 8—figure supplement 2. Locomotor activity and anxiety levels in Syt7 KD rats using OFT and EPM

(**A, C**) Representative tracking trace of the elevated plus maze (*A*) and open field test (*C*). (**B, D**) Mean values for total distance moved (*left*) and time spent (*right*) in each arm (*B*) or in periphery zone (*D*) in control (n = 13) or Syt7 KD rats (n = 9). Mean ± S.E.M.; Unpaired t-test or two-way ANOVA; n.s. = not significant.

References

Diamond JS, Jahr CE (1997) Transporters buffer synaptically released glutamate on a submillisecond time scale. J Neurosci 17:4672-4687.

Holler S, Kostinger G, Martin KAC, Schuhknecht GFP, Stratford KJ (2021) Structure and function of a neocortical synapse. Nature 591:111-116.

Lin JY, Lin MZ, Steinbach P, Tsien RY (2009) Characterization of engineered channelrhodopsin variants with improved properties and kinetics. Biophys J 96:1803-1814.

Little JP, Carter AG (2013) Synaptic mechanisms underlying strong reciprocal connectivity between the medial prefrontal cortex and basolateral amygdala. J Neurosci 33:15333-15342.

Meyer AC, Neher E, Schneggenburger R (2001) Estimation of quantal size and number of functional active zones at the calyx of Held synapse by nonstationary EPSC variance analysis. J Neurosci 21:7889-7900.

Tong G, Jahr CE (1994) Multivesicular release from excitatory synapses of cultured hippocampal neurons. Neuron 12:51-59.

Wadiche JI, Jahr CE (2001) Multivesicular release at climbing fiber-Purkinje cell synapses. Neuron 32:301-313.

Yoon JY, Lee HR, Ho WK, Lee SH (2020) Disparities in Short-Term Depression Among Prefrontal Cortex Synapses Sustain Persistent Activity in a Balanced Network. Cereb Cortex 30:113-134.